TÉCNICO LISBOA

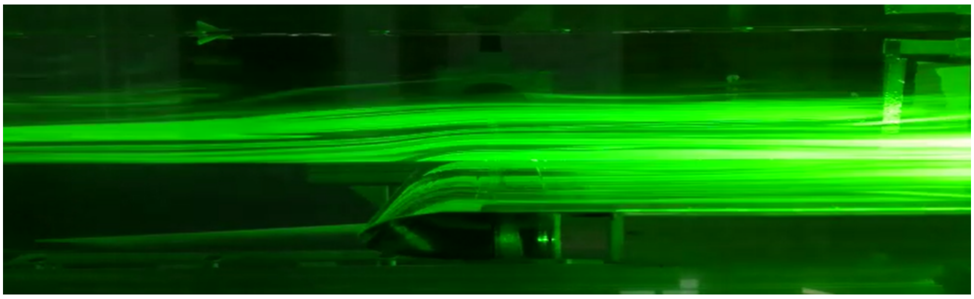

Characterization of DBD Plasma Actuator performance under external flow: Phase-resolved body force field estimation

Gonçalo Nuno Ferreira de Moura Coutinho

Thesis to obtain the Master of Science Degree in

Aerospace Engineering

Supervisor(s): Prof. Ricardo Balbino dos Santos Pereira
Dr. Jochen Kriegseis

Examination Committee

Chairperson: Prof. Filipe Szolnoky Ramos Pinto Cunha
Supervisor: Prof. Ricardo Balbino dos Santos Pereira
Member of the Committee: Prof. José Maria Campos da Silva André

November 2019

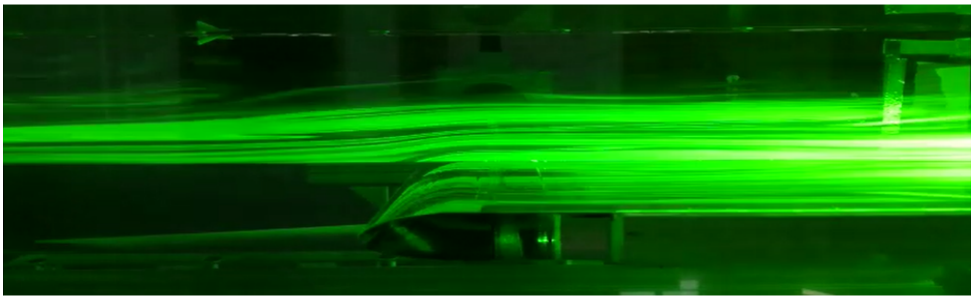

Characterization of DBD Plasma Actuator performance under external flow: Phase-resolved body force field estimation

Gonçalo Nuno Ferreira de Moura Coutinho

Thesis to obtain the Master of Science Degree in

Aerospace Engineering

Supervisor: Prof. Ricardo Balbino dos Santos Pereira
Dr. Jochen Kriegseis

Examination Committee

Chairperson: Prof. Filipe Szolnoky Ramos Pinto Cunha
Supervisor: Prof. Ricardo Balbino dos Santos Pereira
Member of the Committee: Prof. José Maria Campos da Silva André

November 2019

To my beloved family and friends.

Acknowledgments

First and foremost, I would like to thank the opportunity to join the research team at the Institute of Fluid Mechanics, part of the Karlsruhe Institute of Technology (KIT). Specially, to Dr. Ing. Jochen Kriegseis and Msc. Marc Hehner for the incredible support, guidance and experience that allowed me to achieve the goals of this work. I would like to thank my supervisor Prof. Ricardo Pereira who supported me with advice and knowledge which were crucial to complete the present thesis. Furthermore, I would like to thank all the lab group and assistants at the workshop of the KIT for the support.

I also want to thank my beloved family and friends who were always there to provide me with support and kindness since the moment I started my academic life. Specially, during the last 8 months which were crucial to conclude this work.

Special thanks to my mom, who has always been there to support me during my entire life whether in Portugal or abroad. Definitely, a special thank you for the last few months where you always supported me to achieve this goal! Of course, I would also like to thank my brother for being so patient and give me guidance, specially in the last month.

Declaration

I declare that this document is an original work of my own authorship ad that it fulfils all the requirements of the Code of Conduct and Good Practices of the Universidade de Lisboa.

Resumo

O presente trabalho investiga experimentalmente o mecanismo de força de um actuador de plasma na presença de escoamento externo, são realizadas ainda medições elétricas para caracterizar a sua descarga.

Um sistema de velocimetria de imagem de partículas é sincronizado com os eventos de descarga de plasma por forma a obter os campos de velocidade resolvidos na fase com e sem escoamento externo. A potência consumida e a corrente são adquiridas para cada velocidade considerada de escoamento externo. Posteriormente, os campos de força resolvidos no tempo e na fase são determinados e analisados através de dois métodos distintos, com base nas equações de Navier-Stokes e com base na equação de vorticidade. O consumo de energia é estimado de acordo com o método da carga elétrica.

Os campos de força resolvidos no tempo e na fase determinados com as equações de Navier-Stokes parecem resultar numa simplificação excessiva, no entanto o método baseado nas equação de vorticidade é aplicável quando se opera na presença de escoamento externo. Verificou-se que a discretização do ciclo de descarga tem um impacto significativo na força resolvida na fase, no entanto a influência é mínima na força resolvida no tempo. As medições eléctricas indicam uma tendência do consumo de potência praticamente constante, tendo em conta o desvio padrão. A análise do sinal de corrente verifica-se ser independente da velocidade do escoamento externo. Por último, a correlação entre a potência consumida e magnitude da força refletem-se numa tendência crescente da eficiência de mecânica de fluidos do actuator de plasma.

Palavras-chave: actuador de plasma, descarga, campo de forças, escoamento externo, resolvido na fase, resolvido no tempo

Abstract

The present study experimentally investigates the forcing mechanism of an AC dielectric-barrier-discharge plasma actuator under the influence of external airflow. In addition, electrical measurements are performed to characterize the discharge phenomena.

A particle image velocimetry system is synchronized with the plasma-discharge events, in order to extract the velocity information on the phase-resolved plasma discharge in quiescent air and under the operation in the presence of an external airflow. The power consumption and current signals are acquired for each operating free-stream velocity. Subsequently, time-averaged and phase-resolved body-force fields are determined and analysed using two established methods, either based on the Navier-Stokes equations or a vorticity-equation-based approach. The power consumption is estimated according to the electric-charge method.

The time-averaged and phase-resolved plasma body-force fields determined with the Navier-Stokes equations seems to result in an oversimplification whilst the vorticity-equation-based method is found to be applicable when operating with external airflow. The phase resolution is found to have a significant impact on the phase-resolved unsteady term calculation, however meaningless influence on the time-averaged volume integrated force. Regarding the electrical measurements, the results indicate that the power-consumption progression for the operating free-stream velocities is rather unclear. However, due to the standard deviation it is assumed virtually constant. The current-signal analysis evidenced the signal distribution to be similar for different operating free-stream velocities. The correlation between electrical and mechanical characterization reflected only a mild variation of the fluid-mechanic effectiveness which translates into an increasing fluid-mechanic efficiency of the plasma actuator.

Keywords: plasma actuator, discharge, body-force field, external airflow, time-averaged, phase-resolved

Contents

Acknowledgments . . . vii
Resumo . . . xi
Abstract . . . xiii
List of Tables . . . xvii
List of Figures . . . xix
Nomenclature . . . xxvi
Glossary . . . xxvii

1 Introduction **1**
1.1 Motivation . . . 1
1.2 Topic Overview . . . 2
1.3 Objectives . . . 3
1.4 Thesis Outline . . . 3

2 AC-DBD Plasma Actuators **5**
2.1 Overview . . . 5
2.2 Working principle . . . 6
2.3 Electrical Performance . . . 7
2.3.1 Relation between power, voltage and frequency . . . 9
2.4 Mechanical performance . . . 9
2.4.1 Relation with electrical properties . . . 11
2.5 Luminosity . . . 12
2.6 Applications . . . 12

3 State-of-the-Art **15**
3.1 Body force determination . . . 15
3.1.1 Time-averaged force distribution . . . 16
3.1.2 Phase-resolved force distribution . . . 18
3.2 Impact of external flow . . . 20
3.3 Research question . . . 22

4 Methodology 23
4.1 Experimental facility and setup . . . 23
4.1.1 Wind Tunnel . . . 23
4.1.2 AC-DBD Plasma Actuator . . . 24
4.1.3 Electrical measurements . . . 24
4.1.4 Particle Image Velocimetry . . . 25
4.1.5 Experimental Procedure . . . 29
4.2 Data Processing . . . 30
4.2.1 PIVview analysis software . . . 31
4.2.2 Velocity statistical significance . . . 32
4.3 Post processing . . . 34
4.3.1 Uncertainty quantification . . . 34
4.3.2 Boundary layer characterization . . . 36
4.3.3 Body force determination approach . . . 38

5 Results 41
5.1 Electrical characterization . . . 41
5.1.1 Power consumption . . . 41
5.1.2 Current . . . 42
5.2 Plasma Body-force fields . . . 43
5.2.1 Time-averaged body force . . . 43
5.2.2 Phase-resolved body force . . . 51

6 Discussion 65
6.1 Contribution of each source term . . . 65
6.2 Role of the unknown pressure gradient . . . 67
6.3 Influence of phase resolution on the volume-integrated force . . . 68
6.4 Fluid mechanic efficiency and effectiveness . . . 71
6.5 Results reproducibility . . . 72
6.6 Plasma actuator assembly and degradation . . . 73

7 Conclusions 75
7.1 Achievements . . . 75
7.2 Future Work . . . 77

Bibliography 79

A Time-averaged body-force fields 85

B Phase-resolved body-force fields 87
List of Scientific Contributions . . . 91

List of Tables

4.1 Geometric parameters of the current plasma actuator configuration. 24
4.2 Number of discharge cycles between measurements (n), laser (f_l) and camera (f_c) frequency of operation for 8 phases velocity data acquisition. 27
4.3 Number of discharge cycles between measurements (n), laser (f_l) and camera (f_c) frequency of operation for 24 phases velocity data acquisition. 29
4.4 Sequential test matrix used for electrical and velocity data acquisition per each base flow velocity. 30
4.5 External boundary-layer fundamental characteristics without plasma actuation: free-stream velocity (U_∞), BL thickness (δ_{99}), shape factor (H_{12}) and average velocity at the plasma region (U_0). 37

List of Figures

2.1 Plasma actuator standard configuration and ions transfer phenomena during the positive (right figure) and negative-going half cycle (left figure). [14] 6

2.2 Current and voltage signals for a single discharge cycle. [23] 7

2.3 Electrical discharge properties: (a) $Q-V$ cyclogram (Lissajous figure) and discharge capacitances C_0, C_{eff}; (b) Evolution of the voltage and capacitance over time. [8] 8

2.4 Temporal evolution of the horizontal (u) and vertical (v) components of the velocity field in the vicinity of the exposed electrode for subsequent discharge cycles. [22] 10

2.5 Relation between force production and applied voltage for different operating frequencies: (a) Kriegseis et al. [8]; (b) Kotsonis et al. [27]. 11

3.1 Force distribution of the horizontal component of the force $f_x(x,y)$ of the actuator operating at $V = 12$kV and $f = 11$kHz from Kriegseis et al. [28]: (a) N.S.E. [18], (b) V.E. [19]. 17

3.2 (a) Phase-resolved analysis of the source terms contribution for the total force $f_x(x,y)$ [29]; (b) Interrelation between characteristic capacitances C_{eff}, C_0 (pF) and phase-resolved force magnitude $f_x(x,y)$ [29]. 19

3.3 Phase-resolved analysis of the body-force distribution $f_x(x,y)$ during the maximum (LHS) and minimum (RHS) for production according to N.S.E. (3.2a) and V.E. (3.6).[17] 19

3.4 Impact of external flow on the power consumption. (a) Comparison of discharge $Q-V$ cyclogram with characteristic capacitances for $M = 0$ and $M = 0.42$ ($V = 13$ kV; $f = 8$ kHz) [30]; (b) Power consumption per unit length for different external flow velocities U_∞ ($V = 12$ kV; $f = 10$ kHz) [30]. 20

3.5 Light emission normalized intensity for external flow until $U_\infty = 60$ m/s for both co-flow and counter-flow forcing ($V = 20$ kV; $f = 2$ kHz).[9] 21

3.6 Load cell measurements of the plasma force production in co-flow and counter-flow configuration for velocities until $U_\infty = 60$ m/s. [9] 22

4.1 Wind tunnel test section configuration including the elliptic leading edge flat plate, exit section and AC-DBD plasma actuator. 24

4.2 Schematic of the electrical setup including the high-voltage generator (HVG), function generator (FG), power supply (PS); power consumption and current measuring system: C_p capacitor, R_p resistor probe, V actuator voltage, V_p charge-probe voltage. Reproduced from Kriegseis et al. [28], fig. 1. 25
4.3 Velocity acquisition system configuration comprising the high-speed camera, laser and FOV with respect to the plasma-actuator positioning. 26
4.4 Phase positions of the velocity measurements. (a) Phase-resolved decomposition of the discharge cycle in 8 phases positions; (b) Measured phases on the $Q-V$ cyclogram. . . 27
4.5 Temporal evolution of the input electrical signals of the plasma waveform and PIV system. (a) Synchronization between both laser cavities and camera at operating frequency $f_l = 3200$ (Hz) and $f_c = 6400$ (Hz); (b) Function generator square wave, converted sine wave at frequency $f = 10$ (kHz) and corresponding measured phases for two subsequent acquisition cycles (red circles). 28
4.6 Schematic of the PIV acquisition system hardware and plasma actuator electrical setup, including the image and signals recording. 28
4.7 Phase-resolved discharge cycle decomposition in 24 phase positions; White dots represent the additional data points compared to the 8 phases decomposition (red dots). (a) Decomposition of the plasma actuator voltage wave form in 24 phase positions; (b) Measured phases on the $Q-V$ cyclogram. 29
4.8 Calibration target picture comprising the reference axis origin and the image resolution determination. Reference xy-axis orientation flipped (x positive right to left) compared to the results shown in chapter 5. 32
4.9 Outlier detection analysis output comprising: Valid data, interpolated, other peak, outlier, disabled and no result with respect to the number of considered image pairs $\#N$ for $U_\infty = 20$ m/s. (a) Percentage of occurrence of velocity vectors computation according with outlier detection classification in each image pair; (b) Zoom-in of the lower percentage of occurrence region < 2.5 % 32
4.10 Plasma actuator horizontal velocity field $u(x, y)$ characteristic regions in quiescent air: maximum velocity (MV), shear layer (SL), wall jet (WJ) and suction (S). Electrodes and dielectric layers locations represented in grey and yellow, respectively. 33
4.11 Convergence study of the time-averaged and phase-revolved relevant regions of the velocity field with respect to the number of considered image pairs $\#N$ for $U_\infty = 0$ m/s. (a) Time-averaged mean velocity fluctuations (σ_u/u); (b) Phase-resolved velocity fluctuations (σ_u/u) evolution at the suction (S) region. 34
4.12 Horizontal velocity component (u) uncertainty quantification ($U_{\overline{u}}$). (a) Plasma actuation in quiescent air $U_\infty = 0$ m/s; (b) Plasma actuation in laminar BL flow at free-stream velocity of $U_\infty = 20$ m/s. 36
4.13 Baseline BL wall-parallel pressure gradient ($\partial p/\partial x$) distribution. (a) $U_\infty = 2.5$ m/s; (b) $U_\infty = 20$ m/s 38

5.1 Power consumption analysis. (a) Relative power consumption based on P_0 quiescent air $U_\infty = 0$ m/s for increasing free-stream velocity U_∞; (b) Lissajous figure ($Q-V$ cyclogram) comparison for quiescent air (blue data) and $U_\infty = 20$ m/s (red data). 42
5.2 Lissajous figure ($Q-V$ cyclogram) in quiescent air $U_\infty = 0$ m/s (black solid line) superposed with the current signals I in quiescent air $U_\infty = 0$ m/s (blue data) and $U_\infty = 20$ m/s (red data). 43
5.3 Plasma time-averaged horizontal body force distribution $f_x(x,y)$ in quiescent air $U_\infty = 0$ m/s. (a) According to N.S.E. (equation 3.2a); (b) According to V.E. (equation 3.6). 44
5.4 Contribution of the convective and diffusive terms to the spatial distribution of the force $f_x(x,y)$. (a)-(b) convective and diffusive term according to N.S.E. (equation 3.2a): $\rho\left(u\frac{\partial u}{\partial x}+v\frac{\partial u}{\partial y}\right)$, $\mu\left(\frac{\partial^2 u}{\partial x^2}+\frac{\partial^2 u}{\partial y^2}\right)$; (c)-(d) convective and diffusive terms according to V.E. (equation 3.6): $\int_0^\infty \rho\left(u\frac{\partial w}{\partial x}+v\frac{\partial w}{\partial y}\right)$, $\int_0^\infty \mu\left(\frac{\partial^2 w}{\partial x^2}+\frac{\partial^2 w}{\partial y^2}\right)$ 45
5.5 Plasma time-averaged vertical body force distribution $f_y(x,y)$ in quiescent air $U_\infty = 0$ m/s according to N.S.E. (equation 3.2b). 45
5.6 Ratio of force gradients $\partial f_y/\partial x$ and $\partial f_x/\partial y$ determined according to N.S.E. (equation 3.2a); white solid line - 10% isoline of the body-force field $f_x(x,y)$ in quiescent-air conditions. 46
5.7 Horizontal component of the body-force field distribution $f_x(x,y)$ determined according to N.S.E. (equation 3.2a) and subtracting the base flow pressure gradient for different free-stream velocities U_∞. (a) $U_\infty = 5$ m/s; (b) $U_\infty = 10$ m/s; (c) $U_\infty = 20$ m/s. 48
5.8 Horizontal component of the body-force field distribution $f_x(x,y)$ determined according to V.E. (equation 3.6) for different free-stream velocities U_∞. (a) $U_\infty = 5$ m/s; (b) $U_\infty = 10$ m/s; (c) $U_\infty = 20$ m/s. 49
5.9 Integrated value of the time-averaged body-force field horizontal component F_x according to the CV $x = [-1.5; 6]$ mm $y = [0; 2]$ mm using the N.S.E. method (blue data) and V.E. method (black data) for the considered free-stream velocities U_∞. 51
5.10 Phase-resolved body force fields along streamwise direction $f_x(x,y)$ in quiescent air $U_\infty = 0$ m/s determined according to N.S.E. (equation 3.2a). (a) $\phi = 0$; (b) $\phi = \pi/4$; (c) $\phi = \pi/2$; (d) $\phi = 3\pi/4$; (e) $\phi = \pi$; (f) $\phi = 5\pi/4$; (g) $\phi = 3\pi/2$; (h) $\phi = 7\pi/4$. 53
5.11 Phase-resolved body force fields along streamwise direction $f_x(x,y)$ in quiescent air $U_\infty = 0$ m/s determined according to V.E. (equation 3.6). (a) $\phi = 0$; (b) $\phi = \pi/4$; (c) $\phi = \pi/2$; (d) $\phi = 3\pi/4$; (e) $\phi = \pi$; (f) $\phi = 5\pi/4$; (g) $\phi = 3\pi/2$; (h) $\phi = 7\pi/4$. 54
5.12 Contribution of the temporal, convective and diffusive terms to the phase-resolved spatial distribution of the body-force field $f_x(x,y)$ according to N.S.E. (equation 3.2a) at phase position $\phi = 5\pi/4$. (a) Phase-resolved body force $f_x(x,y)$; (b) temporal term: $\frac{\partial u}{\partial t}$; (c) convective term: $\rho u_j \frac{\partial u_i}{\partial x_J}$; diffusive term: $\mu\frac{\partial^2 u_i}{\partial x_j \partial x_j}$ 55
5.13 Phase-resolved integral values of the force F_x and source terms contribution during the discharge cycle determined according to N.S.E. (equation 3.2a): temporal $\frac{\partial u}{\partial t}$ (red data), convective $\rho u_j \frac{\partial u_i}{\partial x_j}$ (blue data) and diffusive $\mu\frac{\partial^2 u_i}{\partial x_j \partial x_j}$ (white data). 55

5.14 Integrated value of the phase-resolved streamwise body-force field F_x according to CV $x = [-1.5; 6]$ mm $y = [0; 2]$ mm using the N.S.E. method (blue data) and V.E. method (black data) for quiescent air $U_\infty = 0$ m/s; the current signal is represented in grey to assess the discharge collapsed region (dashed line box). 56
5.15 Phase-resolved body-force field distribution on the positive-going half cycle for increasing free-stream velocity $U_\infty = [0, 2.5, 7.5, 20]$ m/s determined according to N.S.E. (equation 3.2a). (a)-(d) $\phi = \pi/12$; (e)-(h) $\phi = \pi/3$. 58
5.16 Phase-resolved body-force field distribution on the negative-going half cycle for increasing free-stream velocity $U_\infty = [0, 2.5, 7.5, 20]$ m/s determined according to N.S.E. (equation 3.2a). (a)-(d) $\phi = 5\pi/4$; (e)-(h) $\phi = 17\pi/12$. 59
5.17 Phase-resolved body-force field distribution on the positive-going half cycle for increasing free-stream velocity $U_\infty = [0, 2.5, 7.5, 20]$ m/s determined according to V.E. (equation 3.6). (a)-(d) $\phi = \pi/12$; (e)-(h) $\phi = \pi/3$. 61
5.18 Phase-resolved body-force field distribution on the negative-going half cycle for increasing free-stream velocity $U_\infty = [0, 2.5, 7.5, 20]$ m/s determined according to V.E. (equation 3.6). (a)-(d) $\phi = 5\pi/4$; (e)-(h) $\phi = 17\pi 12$. 62
5.19 Integrated value of the phase-resolved streamwise body-force field F_x according to the CV $x = [-1.5; 6]$ mm $y = [0; 2]$ mm for the tested free-stream velocities U_∞ m/s and current signal; discharge collapse regions indicate by the rectangles. (a) according to N.S.E. (equation 3.2a); (b) according to V.E. (equation 3.6). 63

6.1 Phase-resolved integral value of the source-terms contribution to the net force determined according to N.S.E. (equation 3.2a) (a)-(c) and V.E. (equation 3.6) (d)-(f). (a)-(d) temporal terms; (b)-(e) convective terms; (c)-(f) diffusive terms. 67
6.2 Impact of the discharge cycle discretization $\Delta\phi$ on the body force determination in quiescent air $U_\infty = 0$ m/s according to N.S.E. (equation 3.2a): $\Delta\phi = \pi/3$ (black data), $\Delta\phi = \pi/4$ (blue data), $\Delta\phi = \pi/6$ (red data), $\Delta\phi = \pi/12$ (green data). (a) Phase-resolved body-force production for a single discharge cycle; (b) Time-averaged volume integrated force. 69
6.3 Impact of the discharge cycle discretization and starting phase position on the volume-integrated phase-resolved body force; ($\Delta\phi = \pi/12$ - red data). (a) $\Delta\phi = \pi/4$: $\phi_0 = 0$ (black data), $\phi_0 = \pi/12$ (blue data), $\phi_0 = \pi/6$ (green data); (b) $\Delta\phi = \pi/6$: $\phi_0 = 0$ (black data), $\phi_0 = \pi/12$ (blue data). 70
6.4 (a) Fluid-mechanic efficiency η_{FM} (%); (b) fluid-mechanic effectiveness η^*_{FM} (mN/W) of the present plasma actuator configuration as function of the operating free-stream velocity U_∞ m/s. 72
6.5 Reproducibility of the body-force results determined according to N.S.E. (equation 3.2a) (blue data) and V.E. (equation 3.6) (black data); solid squares represent the first set of experiments and empty circles the second. 73

6.6 AC-DBD plasma actuator analysis. (a) Plasma actuator assembly; (b) Dielectric degradation (red dashed line). 74

A.1 Horizontal component of the body-force field distribution $f_x(x, y)$ determined according to N.S.E. (equation 3.2a) for different free-stream velocities U_∞. (a) $U_\infty = 2.5$ m/s; (b) $U_\infty = 7.5$ m/s; (c) $U_\infty = 15$ m/s. 85
A.2 Horizontal component of the body-force field distribution $f_x(x, y)$ determined according to V.E. (equation 3.6) for different free-stream velocities U_∞. (a) $U_\infty = 2.5$ m/s; (b) $U_\infty = 7.5$ m/s; (c) $U_\infty = 15$ m/s. 86

B.1 Phase-resolved body-force field distribution on the positive-going half cycle for increasing free-stream velocity $U_\infty = [0, 5, 10, 15]$ m/s determined according to N.S.E. (equation 3.2a). (a)-(d) $\phi = \pi/12$; (e)-(h) $\phi = \pi/3$. 87
B.2 Phase-resolved body-force field distribution on the positive-going half cycle for increasing free-stream velocity $U_\infty = [0, 5, 10, 15]$ m/s determined according to N.S.E. (equation 3.2a). (a)-(d) $\phi = 5\pi/4$; (e)-(h) $\phi = 17\pi/12$. 88
B.3 Phase-resolved body-force field distribution on the positive-going half cycle for increasing free-stream velocity $U_\infty = [0, 5, 10, 15]$ m/s determined according to V.E. (equation 3.6). (a)-(d) $\phi = \pi/12$; (e)-(h) $\phi = \pi/3$. 89
B.4 Phase-resolved body-force field distribution on the positive-going half cycle for increasing free-stream velocity $U_\infty = [0, 5, 10, 15]$ m/s determined according to V.E. (equation 3.6). (a)-(d) $\phi = 5\pi/4$; (e)-(h) $\phi = 17\pi/12$. 90

Nomenclature

Greek symbols

Symbol description

δ	Thickness
Δ	Variation
ϕ	Phase angle
η^*	Efficiency
η	Effectiveness
w	Vorticity
ρ	Density
τ	Response time
θ	Momentum thickness
μ	Dynamic viscosity
σ	Standard deviation

Roman symbols

Symbol description

C	Capacitance
d	Diameter
f	frequency / force field
F	force
H_{12}	Shape factor
I	Current
M	Mach number
n	Number of cycles
$\#N$	Image pairs
p	pressure
P	Power
U	Velocity
Q	Charge
R	Resistance
Stk	Stokes number
t	Time
u	x-direction velocity field
U	Velocity
v	y-direction velocity field
V	Voltage
x	Local horizontal in-plane component
y	Local vertical in-plane component
z	Local out of plane coordinate

Subscripts

Symbol description

∞	free stream
FM	fluid mechanic
p	particle/ probe
0	initial/ reference
c	camera
l	laser
$fluc$	fluctuations
err	errors

Glossary

AFC	Active Flow Control
CFD	Computational Fluid Dynamics
CV	Control Volume
DAS	Data Acquisition System
DEHS	di-ethyl-hexyl-sebacat
FOV	Field of View
FG	Function Generator
HVG	High Voltage Generator
LDV	Laser Doppler Velocimetry
LHS	Left Hand Side
MV	Maximum Velocity
NSE	Navier-Stokes Equations
NT	New terms
PIV	Particle Image Velocimetry
PMMA	Plexiglas
PS	Power Supply
RHS	Right Hand Side
SL	Shear Layer
S	Suction
VE	Vorticity Equation
WJ	Wall Jet

Chapter 1

Introduction

In this chapter an introduction to the present study is provided by defining the motivation, overview, objectives and thesis outline.

1.1 Motivation

In recent years, AC dielectric-barrier-discharge (DBD) plasma actuators have shown promising features which are suitable for active flow control (AFC) [1–3]. The well-known induced airflow produced by the plasma discharge has been used for different applications such as laminar-to-turbulent transition and turbulent boundary-layer (BL) control [4–6]. In order to enhance and better understand the electrical and mechanical properties, different experimental campaigns have aimed their efforts into analysing the electrical and mechanical phenomena associated with such a device [7–10]. However, the forcing mechanism revealed to be highly complex and there is still lack of information on the operation in the presence of external flow.

As a promising AFC device, the characterization of the forcing mechanism in the presence of an external flow would provide further insights into how these actuators behave. In addition, it would complement the known plasma actuators computational models for computational fluid dynamics (CFD) simulations [11–13]. For quiescent-air conditions $U_\infty = 0$ m/s, the discharge mechanism has been extensively studied, with various experimental campaigns reporting the electrical and mechanical characterization [14–17]. Nonetheless, in the presence of external flow the behaviour of the body-force field remains yet to be quantified. Furthermore, the two established methods for the body-force determination might not be valid and thus result in an oversimplification [18, 19]. This information is expected, on one hand to provide further insights into the applicability of the methods. On the other hand, knowledge of the body-force production in the presence of external airflow can introduce new goals and challenges for the plasma and AFC community to be tackled, by enhancing and optimizing the plasma actuator in order to be authoritative for the respective application.

1.2 Topic Overview

The AC-DBD plasma actuator is an electrically driven device, responsible for producing a plasma discharge. The standard configuration consists of two electrodes, asymmetrically placed, separated by a dielectric [20, 21]. In order to be operated, a sinusoidal waveform with high voltage ($5 - 40$ kV) at high frequency ($1 - 10$ kHz) is usually applied [22]. One electrode is connected to the high-voltage side whilst the other one is connected to ground. In addition, the grounded electrode is usually covered by an insulation. As a result of the applied voltage, two characteristically different discharges are produced, corresponding to each half-cycle. Literature defines the terms positive and negative-going half cycle accordingly [22–24]. During the negative-going half cycle, the electrons move from the high-voltage electrode to the dielectric layer. In contrast, during the positive-going half cycle, the discharge is limited to the number of electrons accumulated on the dielectric surface and move towards the high-voltage electrode [14, 20–22]. The distinct behaviour between the two half-cycles has been one of the major concerns regarding the plasma discharge characterization. Furthermore, the discharge formation above the dielectric layer is responsible for producing an induced airflow which is the main feature for AFC.

The discharge phenomena in both half cycles have been revealed to be highly complex and has been a subject of extensive experimental research works, with studies being done to characterize the discharge cycle using both electrical and mechanical properties [14–16, 25, 26]. In general, the behaviour is well-known from an electrical point-of-view with established strategies to quantify the power consumption and to analyse the discharge behaviour through current measurements, see e.g. [7, 8, 16]. For instance, the current-signal analysis indicates that the positive-going half cycle is more irregular whereas the negative-going half cycle is more uniform. For the power consumption, the discharge behaviour has been mainly characterized in terms of the dependence on the applied voltage and frequency [8, 16, 27]. Regarding the mechanical characterization, studies have reported the produced airflow velocity to be within a range of a few meters per second. In order to quantify the forcing mechanism, studies have measured for instance the net-force production and body-force field distribution, mainly the variation of the net force with electrical parameters and the spatial distribution of the force [9, 17–19, 27–29]. A power law is found to describe the thrust-voltage and thrust-frequency relation [8, 16, 27]. Additionally, two methods to determine the body-force field have been proposed based on the Navier-Stokes equations and a vorticity-equation-based approach [18, 19]. Studies reported these methods to successfully describe both time-averaged and phase-resolved body-force fields in quiescent-air conditions. The former relates to the mean body-force field over a single discharge cycle whereas the latter represents the force topology in different phase positions, i.e. with respect to time. Whilst the time-averaged force is given by a positive volume force, the phase-resolved comprises an oscillating behaviour between negative and positive force values on the positive and negative-going half cycle, respectively [17, 28, 29]. However, the validity of the assumptions is still unknown in the presence of external flow.

Due to the high applicability as an AFC device, experimental campaigns have spread to the impact of airflow on the plasma-actuator performance. Accordingly, different experimental campaigns have quantified the influence of external airflow on electrical and mechanical properties, see e.g. [9, 30].

Whilst the electrical characterization has already been widely studied, its major conclusions are still not uniform for all experimental campaigns. On the other hand, the impact on the forcing mechanism remains unclear. Even though some studies have successfully described the net force in the presence of external flow, there is a lack of knowledge regarding the time-averaged and phase-resolved body-force fields behaviour when operating with external flow.

1.3 Objectives

The main objective of the present study is to determine and characterize the time-averaged and phase-resolved body-force production of an AC-DBD plasma actuator in the presence of external flow. In addition, power consumption and current signals are acquired. Accordingly, the following tasks are proposed:

- Assemble and synchronize the Particle Image Velocimetry (PIV) system for phase-resolved PIV measurements.
- Characterize the external BL flow where the actuator will operate.
- Quantify the power consumption P and discharge behaviour with current signal I measurements in presence of external flow.
- Determine the time-averaged and phase-resolved body-force $f_x(x, y)$ fields for varying external-airflow velocities with the Navier-Stokes equations (N.S.E.) and vorticity-equation-based (V.E.) method, and compare them to results in quiescent air
- Assess the validity of the negligible pressure gradient $\partial p/\partial x_i$ and force gradient $\partial f_y/\partial x$ on the body-force field determination in presence of external airflow.
- Study the influence of the phase resolution on the estimation of the phase-resolved net force.

1.4 Thesis Outline

The work is presented in a total of seven chapters which include Introduction, literature review, state-of-the-art, experimental study, results and discussion, organized as follows:

- *Chapter 2* provides information on the working principle, mechanical and electrical fundamental characteristics of an AC-DBD plasma actuator, as well as practical applications.
- *Chapter 3* introduces the State-of-the-Art which includes the two established methods to determine the body-force field of a plasma actuator, studies on the impact of external airflow on the performance of a plasma actuator and the research question.
- *Chapter 4* presents the experimental facility and setup, including the synchronization of the PIV system. The post-processing strategy is presented.

- *Chapter 5* introduces the results which include the power consumption, current, time-averaged and phase-resolved body-force fields.
- *Chapter 6* provides a discussion on the results, including the validity of the assumptions of the used methods, assesses the phase-resolution impact on the integral value of the force, fluid-mechanic efficiency and fluid-mechanic effectiveness. The reproducibility of the results, plasma-actuator assembly and degradation are discussed.
- *Chapter 7* concludes the present study and introduces possible improvements for future works within this field of research.

Chapter 2

AC-DBD Plasma Actuators

In this chapter the working principle, applications, electrical and mechanical fundamental properties of an AC-DBD plasma actuator are presented.

2.1 Overview

High-voltage electrical discharges started to be studied in the 19th century and were identified as the fourth state of matter in 1879 by Sir William Crookes [31]. Nonetheless, the term 'Plasma' was only introduced in 1928 by Irving Langmuir and it referred to the region where the agglomeration of ions and electrons was found to be quasi-neutral in a gas discharge [31]. The increasing interest led to the use for illumination, however rapidly surpassed by the discovery of the incandescent lamp. More recently, plasmas have been used in the fabrication process of microelectronic circuits. With the increasing number of studies about plasmas, its definition has changed and now denotes the collection of particles characterized by long-range coulomb interactions in a gas.

Despite those early efforts, the first plasma actuator device for flow control appeared years later with the work of Roth et al. [32] in 1998. The so-called One Atmosphere Uniform Glow Discharge Plasma, as a result of the discharge mechanism, induces an airflow of several meters per second near the surface capable of accelerating surrounding airflow. Experimental results found this method to successfully manipulate laminar and turbulent BL. This was a milestone in flow control research due to its simple construction and easy operation. Since then, the interest in plasma has constantly grown, involving research groups worldwide that focus on characterizing plasma actuators by their electrical and mechanical properties [16, 27, 33–36]. In addition, to the surface DBD plasma actuator [32], mainly three types of plasma actuators have been used for flow control and industrial applications DC corona discharge [2, 37], nanosecond-pulsed [38, 39] and AC-DBD plasma actuators [33, 40]. Throughout this work the term plasma actuator will refer to the AC-DBD plasma actuator. In order to get into more details e.g. Kotsonis [41] provides a thorough review on plasma actuators of different types.

2.2 Working principle

The standard configuration of a surface AC-DBD plasma actuator consists of two electrodes, asymmetrically placed on a dielectric surface, see figure 2.1 [14]. One of the electrodes is supplied with high AC voltage (5-40 kV) at high frequency (1-10 kHz) while the other one is grounded [22]. This design leads to two discharges, one on each side of the dielectric. Experiments of Pons et al. [23] showed that the induced velocity is slightly higher on the high-voltage side. In practical applications a second discharge i.e. on the grounded side is usually unwanted and therefore the electrode is covered by an insulation.

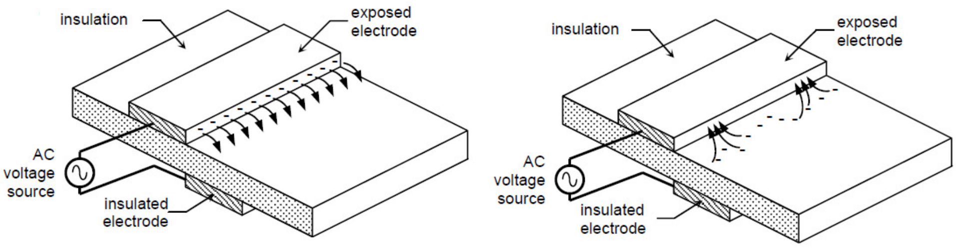

Figure 2.1: Plasma actuator standard configuration and ions transfer phenomena during the positive (right figure) and negative-going half cycle (left figure). [14]

The temporal and spatial structure of the glow discharge has been investigated by several research groups [13, 14, 23]. Although it appears to be uniform in spanwise direction, its process is highly dynamic and develops on a small time scale. In the temporal evolution of the discharge, significant differences have been found between the two half cycles of the applied waveform. Enloe et al. [14] used the terms forward-stroke and backward-stroke for the negative and positive-going half cycles (peak-to-peak) of one AC voltage period, respectively. During the former, the exposed electrode is kept more negative than the surface of the dielectric. Electrons are emitted from the exposed electrode and start to accumulate on the dielectric surface. As the surface charge opposes the applied voltage, the discharge quenches. The positive-going half cycle starts when the polarity between the exposed electrode and the dielectric surface is reversed [14]. This results in the second discharge within the AC voltage waveform cycle which is limited to the electrons accumulated on the dielectric surface.

In order to comprehend how the two discharge cycles develop over time, Pons et al. [23] used a resistive probe connected in series with the actuator to measure the current. The results are shown on figure 2.2. The current evolution exhibits a distinct behaviour in both half cycles. On the positive-going half cycle it seems to be more irregular whereas the negative-going half cycle is more homogeneous. M. Orlov and Edelstein [42], on the other hand, used a high-speed charge-coupled device camera technology to capture short exposure photos of the plasma. The results found the forward discharge to be more diffusive whilst the backward presents a filamentary nature. Similar conclusions were drawn from ion-density distribution in numerical campaigns [23, 43]. These features suggest that the electrical field is significantly different in both discharges. Corke et al. [20] refers the source of electrons as the cause for the contrasting characteristics of the two half cycles. Apparently, the limited number of electrons on the dielectric surface during the backward-stroke leads to a series of micro-discharges rather than to an uniform behaviour presented by the forward-stroke.

Insights into the spatial structure of the plasma were also provided by Enloe et al. [14]. The measurements of the light output from the plasma as function of the streamwise position were determined using a photomultiplier tube. The authors divide the process in two distinct phases: ignition and expansion. The former is characterized by a high-density region near the exposed electrode edge. Afterwards, the plasma density decreases and expands over the dielectric surface. Although the ignition phase was found to be similar in both half cycles, the expansion is again characterized by uniform versus irregular behaviour.

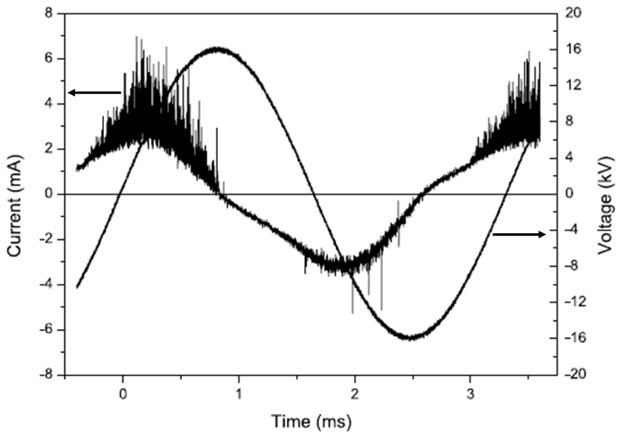

Figure 2.2: Current and voltage signals for a single discharge cycle. [23]

2.3 Electrical Performance

Electrical measurements are a powerful tool to characterize the behaviour of the actuator during operation. Information regarding the power consumption and current enables comparison between designs of these particular devices. Ashpis et al. [7] published a thorough experimental study on two established strategies to determine the power consumption: electric current and electric-charge method. The former consists in measuring instantaneous voltage and current. A shunt resistor is connected in series between the exposed and encapsulated electrode. By measuring the instantaneous voltage $V(t)$ across the resistor the current $I(t)$ can be easily obtained using Ohm's law. The instantaneous power $P(t)$ is then calculated by multiplying the measured voltage and current. The mean power consumption per discharge cycle P is obtained by integrating the instantaneous power over time - equation (2.1). Similarly, the electric charge method consists of placing a capacitor connected in series between the ground electrode and ground. The instantaneous voltage $V(t)$ readings multiplied by the capacitor's charge provide the instantaneous charge $Q(t)$. The mean power consumption P is obtained by integrating the instantaneous capacitor's charge, according to equation (2.2). Moreover, one should notice that the consumed power per discharge cycle is given by the enclosed area of the Lissajous figure ($Q-V$ cyclogram) times the frequency, see 2.3(a).

The results obtained by Ashpis et al. [7] highlighted the capacitor approach as a more consistent, reliable and accurate method than the electrical current approach. In the following, the power-consumption analysis will always refer to the electric-charge method. In order to get into more details of the electrical-current approach the reader should address to Ashpis et al. [7].

$$P(t) = V(t)I(t), \quad P = \frac{1}{T}\int_0^T P(t)dt. \tag{2.1}$$

$$Q(t) = CV(t), \quad P = \frac{1}{T}\int Q(t)\, dV. \tag{2.2}$$

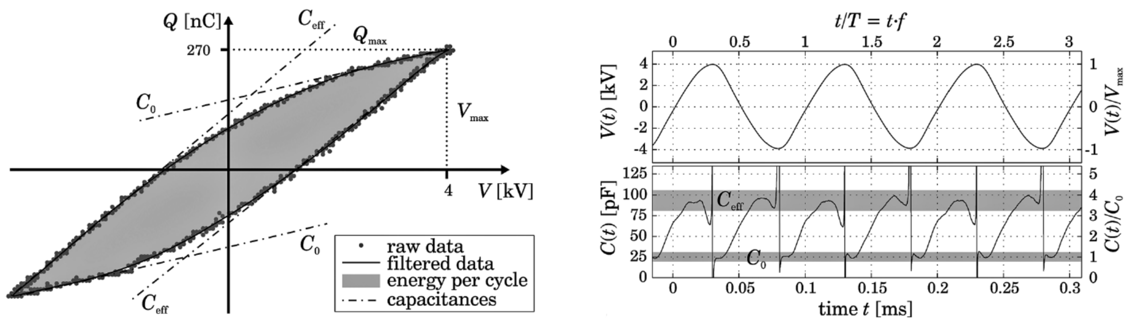

(a) (b)

Figure 2.3: Electrical discharge properties: (a) $Q-V$ cyclogram (Lissajous figure) and discharge capacitances C_0, C_{eff}; (b) Evolution of the voltage and capacitance over time. [8]

The electric-charge approach has been used in many experimental investigations, see e.g. [8, 23, 36]. In particular, Kriegseis et al. [36] published an extensive study on this subject proposing a new discharge quantification strategy using the $Q-V$ cyclogram. Temporal evolution of the plasma actuator capacitance, shown in figure 6.6(b), reveal that the discharge is dominated by two capacitances: cold capacitance C_0 and effective capacitance C_{eff}. The former represents the pure passive component of the actuator and appears in the absence of discharge (voltage peak maximum and minimum). Furthermore, its behaviour is independent from the plasma discharge, however dependent on the actuator material. Hence, its value remains constant for different operational conditions such as voltage and frequency for a specific actuator's design [36]. On the other hand C_{eff}, which combines both C_0 and the contribution of the operating actuator, reveals a dependency on the applied voltage and frequency, thus on power consumption [8]. Its value rises as the discharge develops over the dielectric surface and the capacitance increases from C_0 towards C_{eff} - figure 6.6(b). Moreover, Kriegseis et al. [36] showed that this can be directly related to lissajous figure slope, see figure 6.6(a). Although at first glance the determination of these values appears to be simple, the high fluctuations during the discharge period make it difficult to estimate. A histogram based analysis was proposed to overcome this problem [36].

Furthermore, the determination of these values enables direct comparisons between experiments with the same actuator as a change in C_{eff} is expected when the power consumption changes whilst C_0 is expected to remain constant.

2.3.1 Relation between power, voltage and frequency

The power consumption of the actuator and its dependency of applied voltage and frequency has been subjected to extensive research. Nonetheless, different relations between power versus voltage and power versus frequency have been proposed. Regarding the power-voltage, several research groups claimed a power law relation, however the exponent factor varies depending on the geometry and experimental configuration. For instance, some reports propose a quadratic relation between power and voltage ($P = V^2$) [23, 40], others indicated a power law with exponent between 2 and 3 [4, 22] or even to the power of $7/2$ [6, 34, 36]. Similarly, different relations between power and frequency have been reported. Some research groups found a linear relation [22, 23, 40] whereas others estimated a relation with the power of $1/2$ between power and frequency [36].

The scattered results make comparisons difficult between different experimental data. In order to fill this gap, Kriegseis et al. [36] introduced a novel scaling number (Θ_A). Based on the power laws for voltage and frequency from Kriegseis et al. [36] and the actuator's length, the authors derived a new parameter according to equation 2.3. In conclusion, the authors indicate that the new strategy enables comparison between actuators with different geometric and operational parameters [36].

$$\Theta_A = \frac{P/L}{f^{\frac{1}{2}} V^{\frac{7}{2}}}. \tag{2.3}$$

2.4 Mechanical performance

The main feature of the AC-DBD plasma actuator for AFC is the induced airflow produced by the discharge mechanism. Different experimental campaigns successfully reported that the so-called ionic wind reaches velocities of several meters per second [22, 44]. Furthermore, as a consequence of the oscillating behaviour of the discharge, the velocity field comprises oscillations near the exposed electrode that are gradually attenuated as the flow moves downstream, see e.g. Pons et al. [23]. Forte et al. [22] used Laser Doppler Velocimetry (LDV) to perform stationary and non-stationary velocity measurements in quiescent air. Spatial resolution of the time-averaged velocity showed a downward suction effect right on top of the exposed electrode followed by a wall jet behaviour in streamwise direction downstream the edge of the exposed electrode. More recently, PIV measurements of Debien et al. [16] also verified the presence of a suction region. The time evolution is more complex and features several characteristics that should be carefully analysed. In order to quantify it, the authors measured the velocity in three different positions downstream of the exposed electrode. Figure 2.4 shows the evolution of the velocity components in the tangentially (u) and perpendicular (v) direction in the vicinity of the exposed electrode's edge [22]. On one hand, the negative-going half cycle of the AC-voltage waveform shows a velocity of approximately 3.6 m/s (x-direction) and it is positive during the entire period of actuation. On the other hand, the positive-going half cycle shows a maximum velocity of 2.4 m/s (x-direction) and creates a negative vertical component. However, downstream this region the fluctuations seem to vanish and the velocity magnitude tends to stabilize around a mean value, for both tangential and normal component [22]. Spatial information about the evolution of the velocity profile along the streamwise direction was provided by Pons et al. [23]. The data was acquired using a pitot tube arrangement in several streamwise positions. The results showed an horizontal acceleration component in the vicinity of the exposed electrode's edge followed by a deceleration downstream this region. On the contrary, the height of the jet velocity profile seems continuously increase as the flow moves downstream due to diffusion [23].

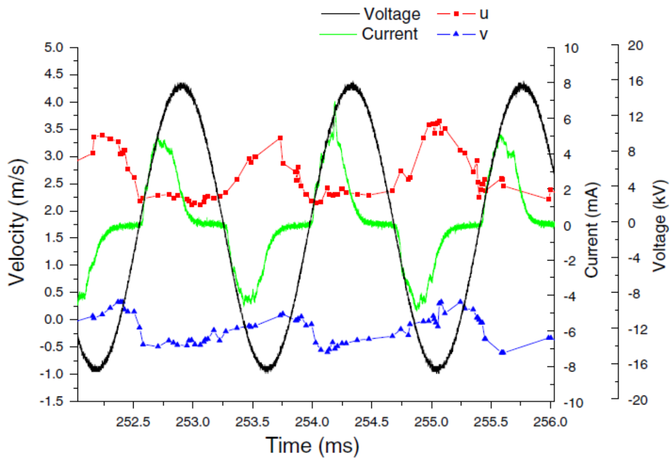

Figure 2.4: Temporal evolution of the horizontal (u) and vertical (v) components of the velocity field in the vicinity of the exposed electrode for subsequent discharge cycles. [22]

In contrast, several authors used the force produced by the ionic wind instead of the velocity to characterize the plasma actuator mechanically [16, 35]. Two methods are commonly used to determine the thrust. The simplest option consist in determining the thrust globally using a balance or load cell [9, 16]. It is usually used to obtain the thrust evolution with electrical and geometric parameters. However, to obtain the spatial distribution of the body force, more sophisticated systems are required. In this case, researchers usually use LDV or PIV systems. The spatial distribution of force is obtained by solving the velocity field within a control volume (CV). These last methods will be introduced later in chapter 3 due to its extreme importance for the present work.

When debating the measurements of a load cell attached to a plasma actuator, one should notice that its value not only accounts for the plasma force but also the induced wall shear stress developed between the wall jet and the plate supporting the actuator [9]. Experimental [15] and numerical investigations [13] reported this effect as a self-induced drag produced by the wall jet. For instance, Enloe et al. [15] used a torsional pendulum to verify the momentum addition by the plasma in quiescent air. The authors noted that between discharges (plasma off) within one AC-cycle the plasma experienced a negative force.

Similarly, the numerical model implement by Font et al. [13] showed that although the force was given by an input square wave, it did not remain constant during the simulations. As the flow accelerates downstream the shear stresses at the wall also increase and thus diminish the net force.

2.4.1 Relation with electrical properties

Electrical parameters play a major role in the mechanical performance of the AC-DBD plasma actuator. Accordingly, literature comprises several studies which report the thrust-voltage and thrust-frequency relation, see e.g. [8, 16, 23, 27].

Experiments of Pons et al. [23] revealed that the maximum airflow velocity increases with applied voltage. Furthermore, velocity profile measurements indicate that the maximum velocity moves downstream as voltage is increased. However, frequency appears to not affect the velocity profile. In conclusion, a linear relation was found between velocity magnitude and frequency.

Regarding the force-production dependency, experimental campaigns [8, 20, 27] which show a good agreement of the results determined a linear relation between the force and frequency. On the other hand, with voltage presents an initially increasing slope that then becomes a linear relation [8], see figure 2.5(a) . In contrast, experiments of Kotsonis et al. [27] and Debien et al. [16] revealed a power-law relation between the force and voltage (figure 2.5(b)). Even though there is some discrepancies in the results regarding the exact relation between the body force and these parameters, all studies revealed an increasing behaviour of the body force magnitude when increasing voltage or frequency. Moreover, the results shown in figures 2.5(a) and 2.5(b) indicate that an increase in voltage has a more pronounced impact on the force production than an increase in frequency.

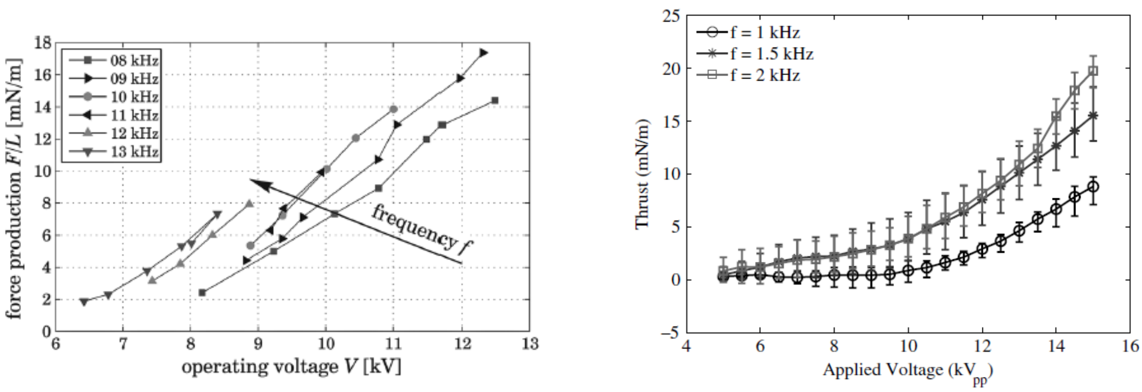

(a) (b)

Figure 2.5: Relation between force production and applied voltage for different operating frequencies: (a) Kriegseis et al. [8]; (b) Kotsonis et al. [27].

However, the increasing behaviour determined for the thrust-voltage and thrust-frequency relation should be carefully analysed. Experiments of Corke et al. [20] showed that there is an optimum frequency of operation which leads to the maximum force. Beyond this point increasing the voltage or frequency will heat the air instead of producing more body force. Nonetheless, the optimum frequency does not match the best energy efficiency of the body-force production. Reports of Kriegseis et al. [8]

showed that in order to guarantee better electrical efficiency, the actuator should be operated at the resonance frequency which strongly depends on the capacitance and applied voltage.

In order to fulfil the relation between electrical and mechanical properties, two additional parameters were introduced in literature: fluid-mechanic efficiency η_{FM} and effectiveness η^*_{FM} [25, 45, 46]. The former is defined by the ratio between the fluid-mechanic power P_{FM} and power consumption P of the actuator [25, 46], see also section 2.3. With the fluid-mechanic power being calculated by integrating the body-force field times the velocity field along a defined region or CV. Further details about the body-force fields determination and analysis is provided in section 3.1. The fluid-mechanic efficiency is shown in equation (2.4). The fluid-mechanic effectiveness is determined by the ratio of the integrated volume force of the plasma actuator and the consumed power according to equation (2.5). Hence, it represents the mechanically induced force that is gained from a certain input electric power, see e.g. Kriegseis et al. [46]. Such as parameters have been used to quantify and optimize plasma actuators for flow control in terms of input electrical power and output thrust [10, 25, 46].

$$\eta_{FM} = \frac{P_{FM}}{P} = \int_A f_x \cdot u dA \cdot \frac{1}{P}. \tag{2.4}$$

$$\eta^*_{FM} = \frac{F_x}{P}. \tag{2.5}$$

2.5 Luminosity

The plasma actuator during the discharge period exhibits an intense purple light characteristic of its behaviour. Although it seems uniform to the naked eye in spanwise direction, its morphology is complex. Therefore, varying experimental campaigns used light emission measurements to determine its structure. For instance, M. Orlov and Edelstein [42] and Debien et al. [16] used phase-locked short exposure photos to determine the discharge morphology. On the other hand, Enloe et al. [35] used photomultiplier tube and grey value distribution with a CCD camera to determine the plasma light emission in the discharge domain.

Experimental campaigns [9, 30] also used the light emission analysis to evaluate the plasma discharge under the influence of external airflow. Kriegseis et al. [30] used a gray value distribution [8] to determine the reduction in the plasma extent at $M_\infty = 0.42$. Similarly, Pereira et al. [9] used measurements of light intensity of the discharge to compare both co-flow and counter-flow configuration with different airflow velocities.

2.6 Applications

Plasma actuator devices have been implemented to a variety of applications within AFC, see e.g. [1–3]. The main purpose of using a plasma actuator for AFC is to delay the laminar-to-turbulent transition and turbulent BL control[4–6]. For instance Jolibois et al. [4] used an AC barrier discharge actuator to control airflow separation over a NACA airfoil. The study consisted on measuring the velocity field through PIV measurements in order to optimize the chordwise location of the actuator. The results indicate the actuator to be capable of reattaching the BL. In addition, the author indicates the actuator to be able to delay the separation point further downstream the airfoil. Similarly, Benard et al. [5] implemented a plasma actuator on an axisymmetric airfoil to study lift and drag performances. The time-resolved PIV measurements indicated that the stall regime can be delayed whilst drag coefficient is reduced. Other studies also reported such a device to be able to successfully control the laminar-to-turbulent transition, see e.g. [6].

The relation between AFC and plasma actuator body-force field can be enhanced by characterizing the forcing mechanism of the actuator in the presence of external airflow. Although for turbulent control the minimal enhancement of the performance is already an improvement, for laminar-to-turbulent transition the behaviour of forcing mechanism when operating with external airflow is a valuable information. This is due to the body-force field distribution and magnitude provided by the device in such conditions. Accordingly, researchers might be able to a priori adjust the actuator properly, thus increase its performance. In the context of the present study, the body-force field determination and studies regarding the operation under the influence of external flow are presented in the following chapter to connect the plasma-discharge events to the scope of the present work.

Chapter 3

State-of-the-Art

In this chapter the body-force field determination methods and respective assumptions are introduced. In addition, a review on the impact of external airflow on the plasma-actuator performance and research question are presented.

3.1 Body force determination

The main feature from the AFC point-of-view of the AC-DBD actuator is the ability to impart momentum to the surrounding airflow. In order to quantify the momentum transfer, it is of further importance to properly determine the plasma body-force distribution. Literature on the subject comprises methods that enable the determination of both magnitude and spatial distribution of the force from velocity data [18, 19, 26, 27]. For instance, PIV provides a two-dimensional (2D) distribution of the velocity field in close proximity of the plasma. The force magnitude can then be estimated using either integral or differential methods. The former is based on the integral momentum balance equation [26, 28]. The force magnitude is estimated by computing the momentum flux across the boundaries of the defined CV. Several authors found this method to be able to estimate the force magnitude [26, 27, 47, 48]. However, similarly to the previously mentioned force estimation from load cell measurements, it also suffers from a lack of spatial resolution. Comprehensive study on the integral methods force estimation is provided by Kriegseis et al. [28]. On the other hand, differential methods, either based on N.S.E. [18] or V.E. [19], are able to provide a spatial distribution of the force.

The general expression for the 2D N.S.E. of Newtonian incompressible fluid ($D\rho/Dt = 0$) with constant viscosity (μ) is shown in equation (3.1). One should notice that the volumetric-force term translates the plasma body-force field distribution $f_i(x, y)$. The convective and diffusive terms can be easily obtained from velocity distribution by computing the first and second spatial derivatives with respect to x and y coordinates. Nonetheless, the difficulty of determining the pressure term experimentally results in a two equation system for three unknowns ($f_i(x, y)$, p), thus further assumptions are required [17].

$$\underbrace{\rho\frac{\partial u_i}{\partial t}}_{\text{local acceleration}} + \underbrace{\rho u_j\frac{\partial u_i}{\partial x_j}}_{\text{convective terms}} = f_i - \underbrace{\frac{\partial p}{\partial x_i}}_{\text{pressure}} + \underbrace{\mu\frac{\partial^2 u_i}{\partial x_j \partial x_j}}_{\text{diffusive terms}}. \tag{3.1}$$

In order to deal with the additional unknown Wilke [18] assumes that the force term is larger than the pressure gradients by at least one order of magnitude in the defined control volume $|f_i| >> |\frac{\partial p}{\partial x_i}|$. Hence, the pressure gradients can be neglected $\partial p/\partial x_i = 0$. The final equations for both x and y-direction are then given by (3.2a) and (3.2b).

$$f_x = \rho\frac{\partial u}{\partial t} + \rho\left(u\frac{\partial u}{\partial x} + v\frac{\partial u}{\partial y}\right) - \mu\left(\frac{\partial^2 u}{\partial x^2} + \frac{\partial^2 u}{\partial y^2}\right), \tag{3.2a}$$

$$f_y = \rho\frac{\partial v}{\partial t} + \rho\left(u\frac{\partial v}{\partial x} + v\frac{\partial v}{\partial y}\right) - \mu\left(\frac{\partial^2 v}{\partial x^2} + \frac{\partial^2 v}{\partial y^2}\right). \tag{3.2b}$$

On the other hand, to overcome the problem of the unknown pressure gradient term Albrecht et al. [19] proposed a 2D V.E. based approach. The V.E. and vorticity are shown in equations (3.3) and (3.4), respectively.

$$\frac{1}{\rho}\left(\frac{\partial f_x}{\partial y} - \frac{\partial f_y}{\partial x}\right) = \underbrace{\rho\frac{\partial w}{\partial t}}_{\text{Local acceleration}} + \underbrace{u\frac{\partial w}{\partial x} + v\frac{\partial w}{\partial y}}_{\text{convective terms}} - \underbrace{\frac{\mu}{\rho}\left(\frac{\partial^2 w}{\partial x^2} + \frac{\partial^2 w}{\partial y^2}\right)}_{\text{diffusive terms}}. \tag{3.3}$$

$$w = \frac{\partial v}{\partial x} - \frac{\partial u}{\partial y}. \tag{3.4}$$

Even though this approach discards pressure gradient considerations, there are still two unknowns ($\frac{\partial f_x}{\partial y}$, $\frac{\partial f_y}{\partial x}$) for one equation. Therefore, another assumption is necessary to compute the force distribution. Reports found that the force field is strongly dominated by the wall-parallel component (x-direction) [27]. Hence, Albrecht et al. [19] assumes that the curl of the force is dominated by the horizontal component $|\frac{\partial f_x}{\partial y}| >> |\frac{\partial f_y}{\partial x}|$. Accordingly, the normal component can be neglected $\frac{\partial f_y}{\partial x} = 0$. The final equation for the remaining force gradient is shown on equation (3.5). The body force distribution can be then obtained by integrating equation (3.5) along the y-direction according to equation (3.6).

$$\frac{1}{\rho}\frac{\partial f_x}{\partial y} = \rho\frac{\partial w}{\partial t} + u\frac{\partial w}{\partial x} + v\frac{\partial w}{\partial y} - \frac{\mu}{\rho}\left(\frac{\partial^2 w}{\partial x^2} + \frac{\partial^2 w}{\partial y^2}\right). \tag{3.5}$$

$$f_x = -\rho\int_{\infty}^{0}\left[\rho\frac{\partial w}{\partial t} + u\frac{\partial w}{\partial x} + v\frac{\partial w}{\partial y} - \frac{\mu}{\rho}\left(\frac{\partial^2 w}{\partial x^2} + \frac{\partial^2 w}{\partial y^2}\right)\right]dy. \tag{3.6}$$

3.1.1 Time-averaged force distribution

The differential methods introduced by Albrecht et al. [19] and Wilke [18] require further analysis and comparison regarding the force behaviour within the CV. Time-averaged force-distribution analysis is provided by Kriegseis et al. [28] and Benard et al. [17]. In the former, the actuator was operated at a voltage of 12 kV and frequency 11 kHz whereas Benard et al. [17] selected a 20 kV operating voltage at a frequency of 1 kHz. Both authors used a PIV setup to acquire the 2D velocity distribution in quiescent air $U_\infty = 0$ m/s.

Benard et al. [17] found the time-dependent term to be small compared to the other source terms of the volume force f_i. As a result of the oscillating behaviour of the plasma discharge, the flow accelerates and decelerates accordingly. Hence, the local acceleration is negligible and can be omitted in the time-averaged analysis. Moreover, these results show good agreement with the force fields from Kriegseis et al. [28].

The time-averaged contours of the streamwise component of the force $f_x(x, y)$ from Kriegseis et al. [28] are shown in figure 3.1. Despite the slight differences between both approaches, the force fields are consistent. In both cases, the results reveal a positive volume-force generation. The bulk of the force appears right on top of the high-voltage electrode edge ($x = 0$ mm) and develops downstream according to the wall jet behaviour towards the far edge of the grounded electrode [22]. A subsequent analysis of the convective and diffusive terms contribution to the force field was also provided. The authors found a strong dominance of the convective term due to the strong convective acceleration ($\partial u/\partial x$). On the other hand, diffusive terms show only minor contributions [28]. Similar findings were reported by Benard et al. [17]. Moreover, there is a negative force region downstream of the upper electrode. This is a result of the so-called plasma self-induced drag [15], see section 2.4. As the flow develops downstream the force starts to be dominated by viscous effects that lead to a deceleration of the flow. Thus, the horizontal convective acceleration ($\partial u/\partial x$) becomes negative, leading to a negative force [28]. Details about the vertical component $f_y(x, y)$ indicate that similarly to the streamwise force term $f_x(x, y)$, the wall-normal component is dominated by the convective acceleration. Furthermore, results from Benard et al. [17] demonstrated that its contribution represents 92% of the total wall-normal force.

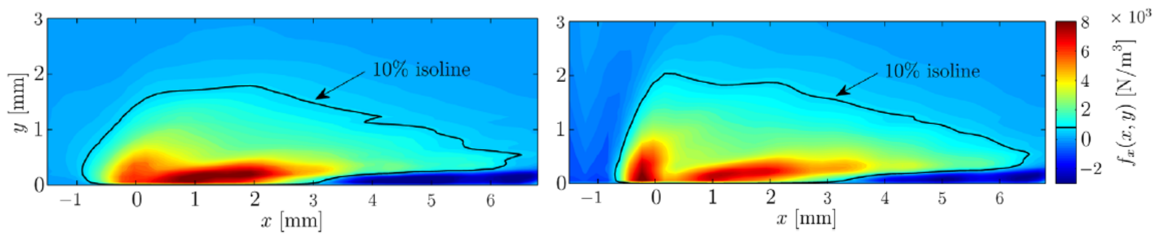

(a) (b)

Figure 3.1: Force distribution of the horizontal component of the force $f_x(x, y)$ of the actuator operating at $V = 12$kV and $f = 11$kHz from Kriegseis et al. [28]: (a) N.S.E. [18], (b) V.E. [19].

Insights into the validity of the assumptions of both methods were also provided by Kriegseis et al. [28]. In order to guarantee the applicability of the VE approach, the authors evaluated the force gradients ratio $|\frac{\partial f_y}{\partial x}|/|\frac{\partial f_x}{\partial y}|$ obtained with the N.S.E. approach [18]. A 10% isoline of the body-force field $f_x(x, y)$ was defined as the area of interest of the plasma body-force field, see figures 3.1(a) and 3.1(b). The results revealed that the curl force ratio is dominated by the horizontal component within the designated area. However, larger values were found in surrounding regions invalidating the assumption in certain parts of the domain [28]. Hence, it is of further importance to carefully assess the assumption made in the V.E. approach. On the other hand, the authors were not able to evaluate the unknown pressure gradient due to lack of information. Nonetheless, the comparison between results from figures 3.1(a) and 3.1(b) seems to indicate that the pressure terms are at least one order of magnitude smaller than the force [28]. Accordingly, the hypothesis was considered to be valid.

In conclusion, the detailed analysis provided by Kriegseis et al. [28] demonstrate that, although the force shape and distribution is slightly different in both methods, the results show good agreement. However, the authors highlight that the V.E. approach suffers from lack of wall-normal momentum-transfer information $f_y(x, y)$ whereas the N.S.E. assumption cannot be further evaluated based on the body-force field distribution.

3.1.2 Phase-resolved force distribution

The phase-resolved body force relates to the volume-force generation in different phase positions of a single discharge cycle. In contrast to the time-averaged force, the phase-resolved force field is strongly dependent on the temporal term, see equations (3.2) and (3.5). Benard et al. [17] stated that the unsteady term represents 87% of the total produced force in both horizontal and vertical directions. Such a result is attributed to the highly unstable character of the discharge cycle. Similar conclusions were drawn by Kuhnhenn et al. [29] (see figure 3.2(a)). The impact of both convective terms is minimal when compared with the time-dependent term. Moreover and directly related to the time evolution of the velocity, the force magnitude comprises periodical fluctuations throughout the actuation period. However, the force depicts a positive versus negative volume force generation. During the negative-going half cycle the force is found to be mostly a positive force whilst a negative force magnitude is detected during the positive-going half cycle. This corroborates the push/pull behaviour of the plasma [16, 17]. Regardless, the time-averaged force integral is found to be positive due to the larger magnitude during the positive forcing. Furthermore, a phase offset seems to characterize the force in relation to the applied waveform. This aspect was also reported by other authors [16–18, 22].

Kuhnhenn et al. [29] related the capacitances and time evolution of the plasma forcing mechanism over one discharge cycle according with the capacitance-quantification strategy introduced by Kriegseis et al. [36], see figure 3.2(b). This results highlight the correlation between null-force magnitude and the cold capacitance at phase angles $\phi = 3\pi/4$ and $\phi = 7\pi/4$. Moreover, the largest magnitude was found to coincide with the effective capacitance during the negative half-cycle $\phi = 5\pi/4$ whereas the negative peak is located at the effective capacitance of the positive half-cycle.

Details about the phase-resolved discharge topology were provided by Benard et al. [17] and Kuhnhenn et al. [29]. The authors analysed the time evolution of the force field in phase positions of the applied sine-wave. The results from Benard et al. [17] obtained the with N.S.E. and V.E. method are shown in figure 3.3 for the maximum and minimum volume force generation. The time-locked reference t^* relates to the non-dimensional time of the problem t^*/T, where T represents the period of one AC-voltage cycle. Furthermore, Benard et al. [17] reported that the successive numerical operations related to the V.E. method degrade the results as non-physical vertical stripes are presented on the body-force field distributions.

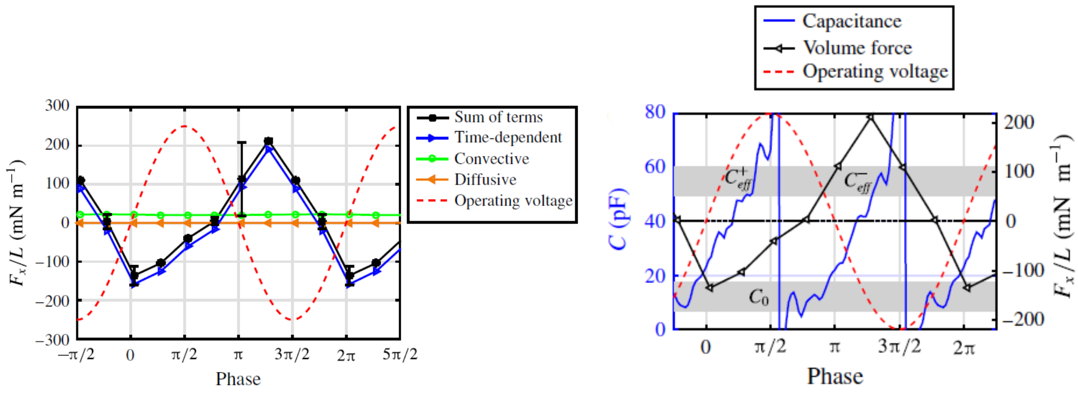

(a) (b)

Figure 3.2: (a) Phase-resolved analysis of the source terms contribution for the total force $f_x(x, y)$ [29]; (b) Interrelation between characteristic capacitances C_{eff}, C_0 (pF) and phase-resolved force magnitude $f_x(x, y)$ [29].

In general, the authors found the results obtained with the two approaches to correlate. Although the body-force field distributions present mild differences, it is stated that the good correlation indicates that the assumption of a negligible pressure gradient leads to trustful results for a first approximation. Furthermore, as an aspect of major importance, the authors stated that the volume-force generation is responsible for a push/push behaviour which is in contrast with the push/pull theory. The force production during the positive-going half cycle is found to be significantly weaker. Accordingly, the authors point out that viscous effects might be camouflaging the force production and thus leading to a negative volume force generation [17].

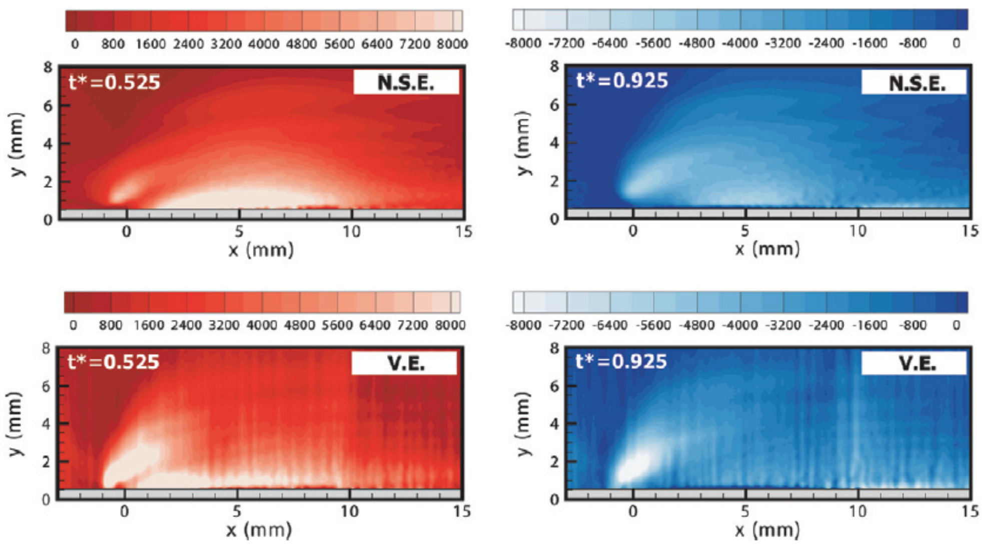

Figure 3.3: Phase-resolved analysis of the body-force distribution $f_x(x, y)$ during the maximum (LHS) and minimum (RHS) for production according to N.S.E. (3.2a) and V.E. (3.6).[17]

3.2 Impact of external flow

Comprehensive studies about the performance of the AC-DBD plasma actuator under external flow were published by Pereira et al. [9] and Kriegseis et al. [30]. In the former, a self-adhesive copper tape was used for the electrodes and *Plexiglas* (PMMA) for the dielectric. The actuator was operated with a peak-to-peak voltage of $40\,$kV at frequency of $2\,$kHz. The latter, comprises different experiments in which copper-Kapton actuators with various lengths were operated at different voltages and frequencies [30]. The studies aimed at the analysis of the power consumption and luminosity in the presence of external flow. Load cell measurements of the force in both co-flow and counter-flow configuration were also provided by Pereira et al. [9].

Regarding the electrical measurements, in both cases the electric-charge method [7] was used to determine the instantaneous voltage $V(t)$ and charge $Q(t)$, thus power consumption. The power consumption measurements from Kriegseis et al. [30] are shown in figure 3.4(b). These results evidence a significant performance drop when operating under the influence of external flow. In particular, the average power consumption per cycle is already reduced by 6% at $M = 0.145$ and 10% for $M = 0.2$. Figure 3.4(a) shows the comparison of the lissajous figure between quiescent air ($M = 0$) and $M = 0.42$. The voltage remains unchanged whereas the peak magnitude of the charge decreases, thus indicating a reduction in power consumption as the area shrinks. Moreover, the discharge' capacitances C_{eff} and C_0 were also correlated with the power drop. The cold capacitance confirmed its pure passive behaviour as its value remain unchanged as the power varies due to the presence of airflow. However, the effective capacitance being directly dependent on the power consumption also showed a decrease, see figure 3.4(a). In contrast, the results from Pereira et al. [9] revealed an independence of the power consumption from external flow ($U_\infty < 60\,$m/s) for co-flow and counter-flow configuration. The small differences found were attributed to the construction and assembly of the plasma actuators [9]. Furthermore, contrarily to the results shown in fig 3.4(a), the $Q - V$ cyclogram remained virtually constant.

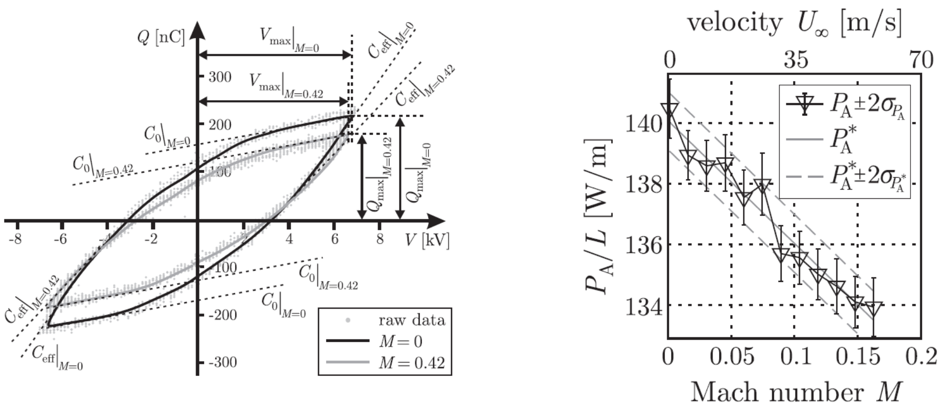

(a) (b)

Figure 3.4: Impact of external flow on the power consumption. (a) Comparison of discharge $Q - V$ cyclogram with characteristic capacitances for $M = 0$ and $M = 0.42$ ($V = 13\,$kV; $f = 8\,$kHz) [30]; (b) Power consumption per unit length for different external flow velocities U_∞ ($V = 12\,$kV; $f = 10\,$kHz) [30].

Plasma light emission analysis was used to obtain the discharge area light intensity along x-direction

[9]. The data was acquired through a series of short exposure photos of the plasma-discharge domain. The results of the normalized light intensity of the discharge for velocities until $U_\infty = 60$ m/s from Pereira et al. [9] are shown in figure 3.5. In co-flow forcing, the light intensity is weakly dependent on the external flow. Reports from [30] also showed a negligible light intensity reduction for similar external flows. Nonetheless, for higher airflow's velocities ($M > 0.2$) the resulting length of the plasma in x-direction decreases [30]. On the other hand, the normalized light intensity of the plasma discharge domain in counter-flow forcing was found to increase with external flow [9], see figure 3.5.

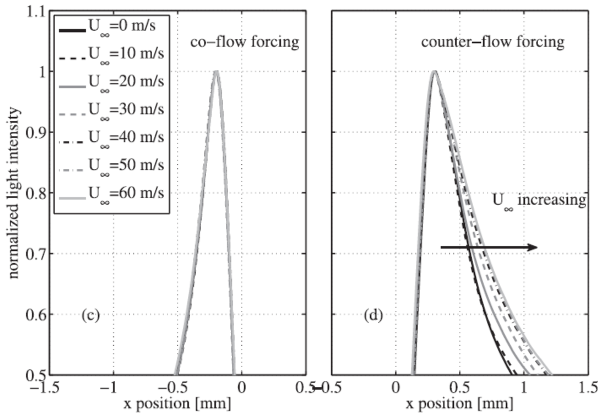

Figure 3.5: Light emission normalized intensity for external flow until $U_\infty = 60$ m/s for both co-flow and counter-flow forcing ($V = 20$ kV; $f = 2$ kHz).[9]

The load cell measurements from Pereira et al. [9] are shown in figure 3.6. One should notice that the force magnitude $|\Delta F_{LC}|$ is given by the difference between plasma on and plasma off. This represents the plasma body force magnitude plus the difference between skin friction with and without actuation. The co-flow forcing load measurements show an increasing behaviour of the force for velocities until $U_\infty = 30$ m/s which then turn into a constant value for $U_\infty = 40$ m/s. Furthermore, for higher velocities up to $U_\infty = 60$ m/s the force seems to increase. The lower value in quiescent air is attributed to the opposing skin friction in relation to the plasma force production. For higher velocities, due to the presence of a BL the skin friction in the plasma-off situation automatically increases. In addition, the plasma was hypothesized to loose the ability to change skin friction for such velocities. Consequently, the plasma body-force magnitude increases as the skin friction variation tends to zero. Nonetheless, the increase for velocities higher than $U_\infty = 40$ m/s could not be explained and further experiments are required to explain such behaviour [9].

On the contrary, the counter-flow forcing measurements indicate a constant behaviour once the plasma is operating with velocities higher than $U_\infty = 10$ m/s. By opposing the plasma forcing and external flow, the plasma is expected to trigger the laminar-to-turbulent BL transition [9]. Consequently, the skin friction will significantly increase. This effect plays a role in the higher value for $U_\infty = 10$ m/s case as the BL was found to be laminar. In contrast, for higher velocities the plasma was operating in a turbulent BL and the impact of the plasma forcing remained unchanged [9].

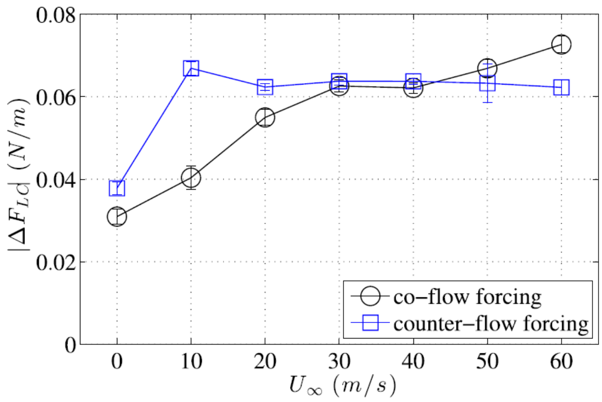

Figure 3.6: Load cell measurements of the plasma force production in co-flow and counter-flow configuration for velocities until $U_\infty = 60$ m/s. [9]

3.3 Research question

The present literature review introduces several studies based on plasma discharge mechanism characterization using both electrical and mechanical information, see e.g. [17, 20, 21]. However, the impact of external airflow remains to be clarified. On one hand, the electrical measurements report either a decreasing or constant trend of the power consumption per cycle with increasing external airflow velocity [9, 30]. On the other hand, the studies regarding the body-force field distribution were only performed in quiescent-air conditions [17, 27–29]. Although the results presented by Benard et al. [17] and Kriegseis et al. [28] indicate that both assumptions are reasonable for quiescent air, the applicability under the presence of external airflow suffers from lack of information. Consequently, the methods introduced by Wilke [18] and Albrecht et al. [19] might result in an oversimplification when operating with external flow. Hence, the present thesis proposes a characterization of the discharge regime under the influence of external airflow. Accordingly, the N.S.E. and V.E. methods are presently studied to assess the validity of the assumptions when operating with external flow, see N.S.E. (3.2a) and V.E. (3.6). Both time-averaged and phase-resolved body-force field distributions are evaluated for various free-stream velocities. Regarding the electrical quantities, power consumption and current-signal analysis are performed to evaluate the plasma discharge-events and clarify the results obtained by Kriegseis et al. [30] and Pereira et al. [9].

Chapter 4

Methodology

In this chapter the experimental facility, setup and procedure are presented. Additionally, the post-processing strategy is introduced.

4.1 Experimental facility and setup

4.1.1 Wind Tunnel

In the present work, electrical and planar high-speed PIV measurements were used to acquire information on the power consumption per discharge cycle, current and 2D velocity information on the plasma discharge in quiescent air and under the influence of external flow. The experiments were carried out in a sub-sonic blower-type wind tunnel located in the Institute of Fluid Mechanics laboratory at Karlsruhe Institute of Technology (KIT). The tunnel allows the operation within a range of free-stream velocities $U_\infty = [2.5; 50]$ m/s. The airflow velocity is regulated manually and the volume-flow rate can be determined from a static pressure measurement system at the inlet nozzle. The free-stream velocity can be then calculated. Due to its low precision, PIV measurements were used to determine the correct free-stream velocity. The test section is situated at the exit of the tunnel and consists of a rectangular section (320×220 mm^2) with 690 mm length made of PMMA which provides optical access. The actuator was placed on a flat plate with elliptic leading edge, both horizontally and vertically centred in the test section (see figure 4.1).

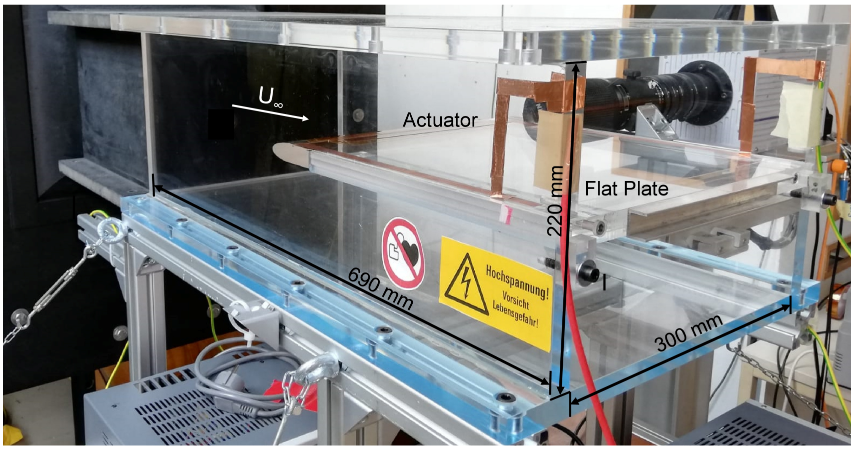

Figure 4.1: Wind tunnel test section configuration including the elliptic leading edge flat plate, exit section and AC-DBD plasma actuator.

4.1.2 AC-DBD Plasma Actuator

In order to guarantee comparability with the body-force field characterization of Kriegseis et al. [28] and Kuhnhenn et al. [29], the characteristics of the actuator were chosen to match. Hence, the actuator consists of two self-adhesive copper tape electrodes with no longitudinal offset separated by a multi-layer dielectric. A polyimide film (Kapton®) was used for the dielectric. The actuator has a span of 150 mm. The width of both encapsulated and exposed electrodes is 10 mm and 2.5 mm, respectively. The dielectric consists of 5 layers of Kapton® tape with total thickness of 0.4 mm. Table 4.1 summarizes the current actuator architecture. The actuator was placed in co-flow configuration (wall-jet along mean-flow direction), 57 mm downstream of the leading edge of the flat plate. To prevent rapid degradation due to air bubbles and minimize surface roughness, the actuators were carefully inspected after the assembly and before the experiments [49]. In addition, the tips of both electrodes were rounded to prevent accumulation of discharge on the edges [50]. The actuator was driven by a sinusoidal waveform with a peak-to-peak voltage of $V = 15$ kV at an AC frequency $f = 10$ kHz.

Parameter	Material	Length (mm)	Width (mm)	Thickness (µm)
Exposed electrode	Copper	150	2.5	60
Encapsulated electrode	Copper	150	10	60
Dielectric thickness	Kapton®	150	25	400

Table 4.1: Geometric parameters of the current plasma actuator configuration.

4.1.3 Electrical measurements

The electrical setup of the plasma actuator includes the actuator's input signal and acquisition system. The former was given by a high-voltage generator (HVG) GBS Electronik MiniPuls 2.1. By providing a low voltage input square wave at the desired frequency, the HVG filters and transforms it into an output sine wave. The square wave was given by an ILA5150 high-speed synchronizer that works as a function generator (FG) and an external power supply unit Voltcraft VLP 1405 Pro was used to provide the input voltage. Regarding the recording system, two configurations were used to measure power consumption and current. The power consumption was determined using the electric-charge method [7, 8]. A ceramic charge-probe capacitor $C_p = 22$ nF was connected in series between the grounded electrode and ground. The system records the voltage across the capacitor and applied voltage. For the current measurements, the capacitor was replaced by a shunt resistor $R_p = 2.2\,\Omega$ [7, 17]. Furthermore, in both cases the data was acquired with InfiniiVision DSO-X 2004 oscilloscope (70 MHz; 2 GSa/s) with a vertical resolution of 9 bit. The readings were taken with a sampling rate of 5 MSa/s at a maximum available length (25000 data points). Thus, the electrical characteristics were acquired over 50 discharge cycles each measurement with a total of 500 data points per cycle. The electrical setup is illustrated in figure 4.2.

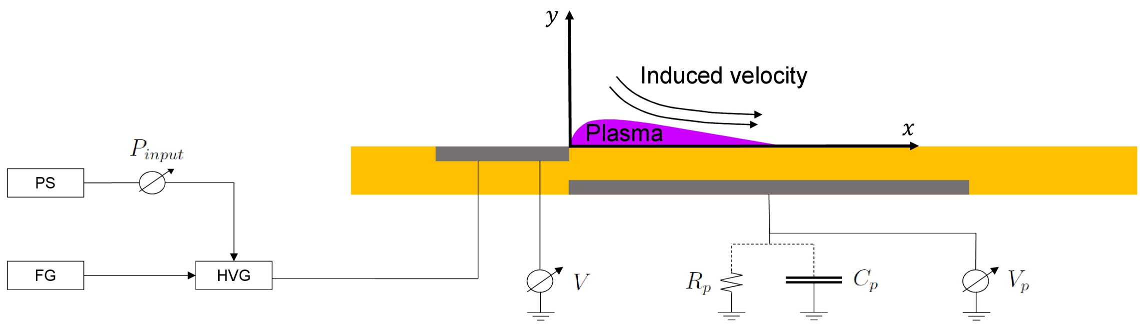

Figure 4.2: Schematic of the electrical setup including the high-voltage generator (HVG), function generator (FG), power supply (PS); power consumption and current measuring system: C_p capacitor, R_p resistor probe, V actuator voltage, V_p charge-probe voltage. Reproduced from Kriegseis et al. [28], fig. 1.

4.1.4 Particle Image Velocimetry

Velocity information on the plasma discharge was captured using a planar high-speed PIV system. The PIV system is comprised by a Neodym YLF ($\lambda = 527$ nm) dual-cavity laser Quantronix Darwin Duo and one Photron Fastcam SA4 high-speed camera (maximum resolution 1024×1024 px^2). The camera was operated with a Nikon AF micro Nikkor 200 mm f/4D IF-ID lens. In addition, four extensions with total length of 108 mm were added to obtain high resolution of 1024×512 px^2 and an appropriate object distance. The system was synchronized using an ILA 5150 high-speed synchronizer. The experiments were conducted in the $x - y$ plane located at the centre of the actuator ($z = 0$) with a field-of-view (FOV) located in close proximity with the discharge region 10×4.5 mm^2 length and height, respectively. It was assumed that the present plasma configuration produces a uniform discharge along the z-direction at the mid-span coordinate and thus the flow can be considered bi-dimensional at the $x - y$ plane. The PIV system was calibrated before each set of experiments to align the camera and laser with the FOV. Figure 4.3 shows the positioning of the laser and camera with respect to the test-section configuration and corresponding FOV.

In order to capture the instantaneous particle position, the flow was seeded with di-ethyl-hexyl-sebacat (DEHS) tracers with mean diameter of $d_p = 0.9$ µm. The tracer particles were carefully chosen to avoid being charged due to the strong electric field near the plasma region [10]. Taking into account the DEHS density ($\rho_p = 914$ kg/m^3) and air dynamic viscosity ($\mu = 18.5$ µPa·s), the particle response time of the tracers is given by $\tau_p = d_p^2 \rho_p / 18\mu = 2.22$ µs. Subsequently, the maximum Stokes number is found to be equal to $Stk = \tau_p U_\infty / l_c = 6.66 \times 10^{-2}$ for $U_\infty = 20$ m/s, with l_c characteristic length scale of the problem [29, 48]. Hence, the particles are expected to follow flow motion with acceptable accuracy [51].

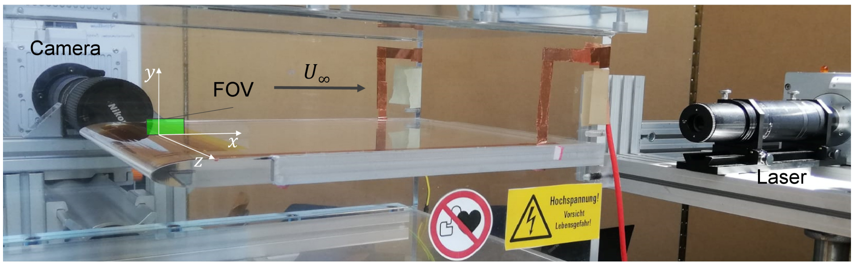

Figure 4.3: Velocity acquisition system configuration comprising the high-speed camera, laser and FOV with respect to the plasma-actuator positioning.

Phase-resolved velocity measurements

Phase-resolved velocity acquisition was divided in two separate sets of experiments. In the first approach, the applied voltage waveform was decomposed in 8 different phases equally spaced in time, corresponding to $\Delta\phi = \pi/4$ (4 per half-cyle) according with the experiments of Kuhnhenn et al. [29]. This decomposition provides access to the momentum transfer ability during both positive- and negative-going half cycles. Figure 4.4 shows the correspondent phases (in red) of the discharge in the applied sinusoidal waveform and $Q - V$ cyclogram.

The challenge of recording the velocity information of all 8 phases in one single measurement is considerable due to the small time scale of the discharge cycle ($f = 10$ kHz), maximum frequency of operation of the laser $f_l = 5000$ Hz and synchronizer software accuracy. In the present work, it is proposed to record sequentially the 8 phases of the discharge cycle during a certain number of cycles. Thus, the laser frequency should correspond to a multiple (n) of the plasma discharge cycle period ($T = 1 \times 10^{-4}$ s) plus the phase-to-phase time spacing $\Delta t_{ph} = 12.5 \times 10^{-5}$ s, see equation 4.1. Furthermore, the camera must operate with twice the laser frequency to capture both pulses. Table 4.2 shows the possible range of operation frequency for the laser (f_l) and camera (f_c).

$$f_l = (n \times T + \Delta t_{ph})^{-1}. \tag{4.1}$$

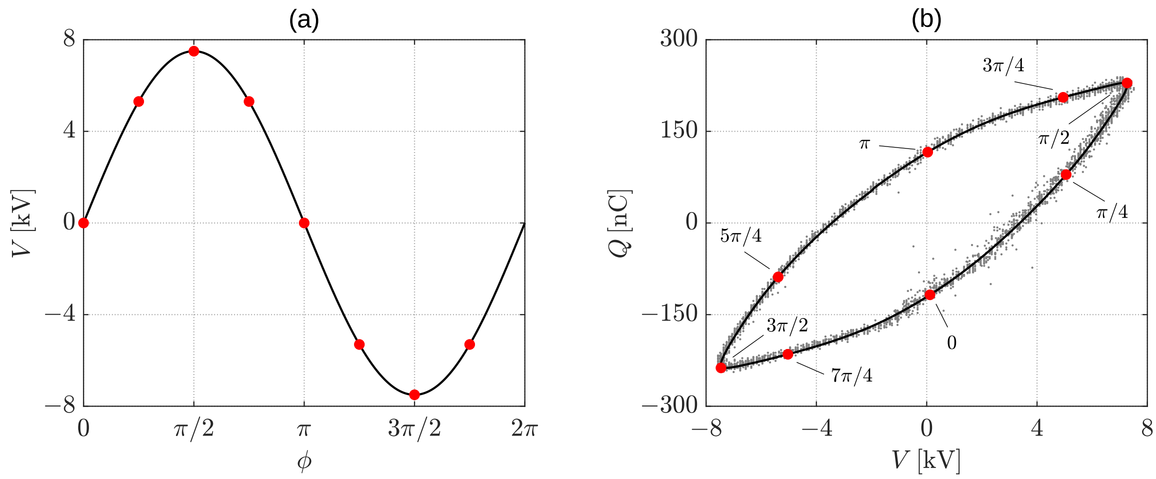

Figure 4.4: Phase positions of the velocity measurements. (a) Phase-resolved decomposition of the discharge cycle in 8 phases positions; (b) Measured phases on the $Q - V$ cyclogram.

Parameters	Operational settings					
Cycles of interval (n)	1	2	3	4	5	6
Laser frequency f_l (Hz)	8888.88	4705.88	3200	2424.24	1951.22	1632.65
Camera frequency f_c (Hz)	17777.76	9411.76	6400	4848.48	3902.44	3265.30

Table 4.2: Number of discharge cycles between measurements (n), laser (f_l) and camera (f_c) frequency of operation for 8 phases velocity data acquisition.

According to table 4.2, the most accurate operation is found for an acquisition rate of one phase per each three cycles of actuation. The laser should be operated at a frequency of $f_l = 3200\,$Hz. The pulse distance is $\Delta t = 4 \times 10^{-6}\,$s and pulse width is $\Delta t = 1 \times 10^{-6}$ s. The camera acquisition rate is $f_c = 6400\,$Hz and corresponding pulse width is $\Delta t = 40 \times 10^{-6}\,$s. Figure 4.5 shows the synchronization between the sine wave, laser and camera signals for two consecutive phase positions. In addition, the current settings enable to operate the camera at reduced sensor size $1024 \times 512\,$px^2 and final resolution of 96 pixels per millimetre. The camera buffer capacity ($8\,$Gb) was fully used in each measurement. This arrangement provided a maximum number of $N = 10914$ frames per run. In double pulse mode, corresponds to 5456 image pairs per run and 682 image pairs per phase angle. The images were then stored in a computer hard-drive.

The system was operated using the *SigMa* software of the synchronizer with an external trigger. In each measurement, to ensure consistency between different data sets, the actuator was switched on $10\,$s before acquiring the data, however the phase position of the first recording is arbitrary. To overcome this problem, the signals of the laser cavity 1, camera trigger and output voltage from the HVG were acquired using an auxiliary data acquisition system (DAS) National Instruments USB-X series multi-function DAQ. The signals were then processed using *LabView* software to determine the first recorded phase in a second computer. Figure 4.6 shows the schematic of the entire hardware including the plasma system and DAS.

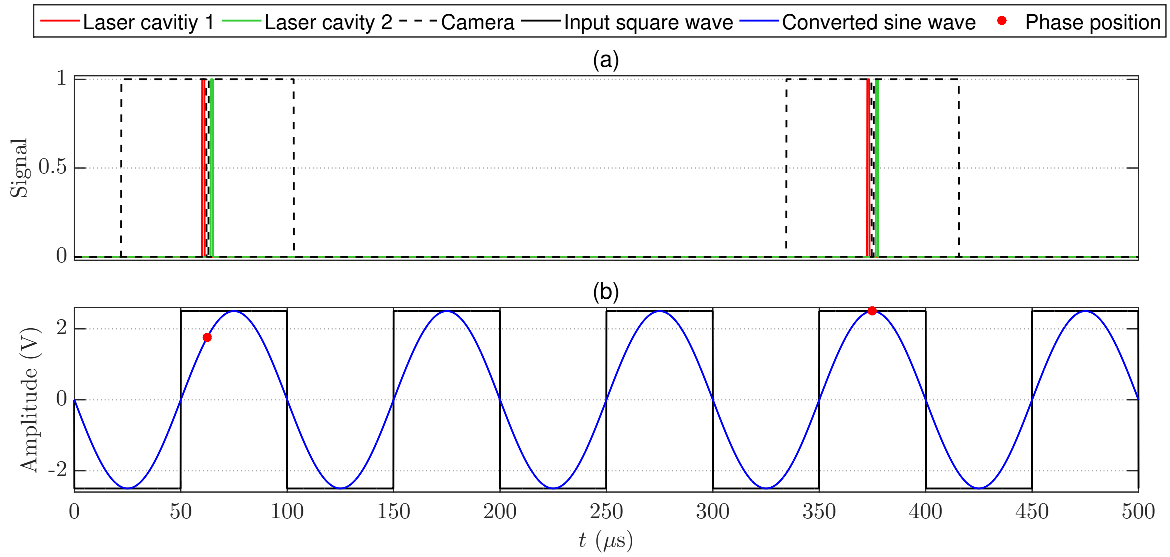

Figure 4.5: Temporal evolution of the input electrical signals of the plasma waveform and PIV system. (a) Synchronization between both laser cavities and camera at operating frequency $f_l = 3200$ (Hz) and $f_c = 6400$ (Hz); (b) Function generator square wave, converted sine wave at frequency $f = 10$ (kHz) and corresponding measured phases for two subsequent acquisition cycles (red circles).

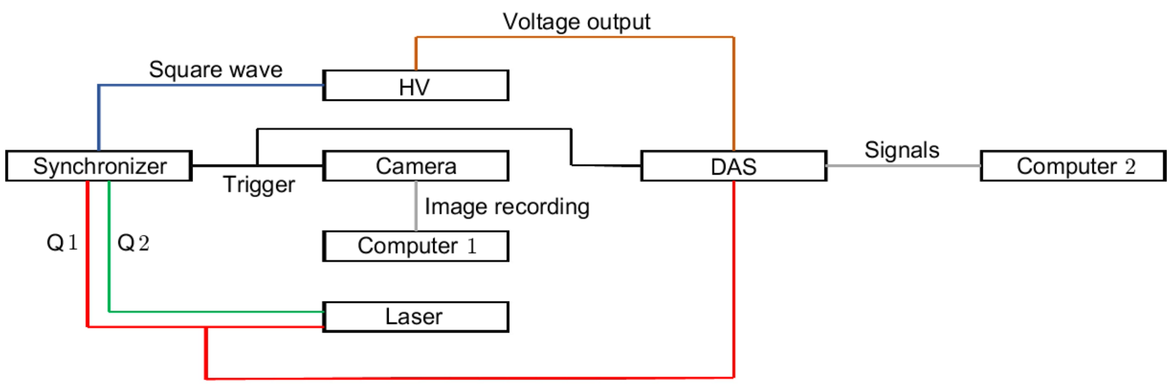

Figure 4.6: Schematic of the PIV acquisition system hardware and plasma actuator electrical setup, including the image and signals recording.

A second set of experiments was performed with the purpose of accessing information about the discharge morphology that might be hidden within the time spacing of the 8 phases approach. Hence, the discharge cycle was decomposed in 24 phases equally spaced in time, corresponding to $\Delta\phi = \pi/12$, see figure 4.7. The PIV setup and actuator design remain unchanged in order to guarantee comparability with the 8 phase positions resolution. However, the operating frequency of the laser and camera were adjusted to capture 24 instead of 8 phases, according to equation (4.1). Notice the phase-to-phase time spacing is now reduced to a third $\Delta t = 4.1(6) \times 10^{-6}$ s. Table 4.3 shows the possible operation frequencies for the laser (f_l) and camera (f_c) with respect to number of cycles between recordings.

Parameters	Operational settings					
Cycles of interval (n)	1	2	3	4	5	6
Laser frequency f_l (Hz)	9600	4897.96	3287.67	2474.23	1983.47	1655.17
Camera frequency f_c (Hz)	19200	9795.92	6575.34	4948.45	3966.94	3310.34

Table 4.3: Number of discharge cycles between measurements (n), laser (f_l) and camera (f_c) frequency of operation for 24 phases velocity data acquisition.

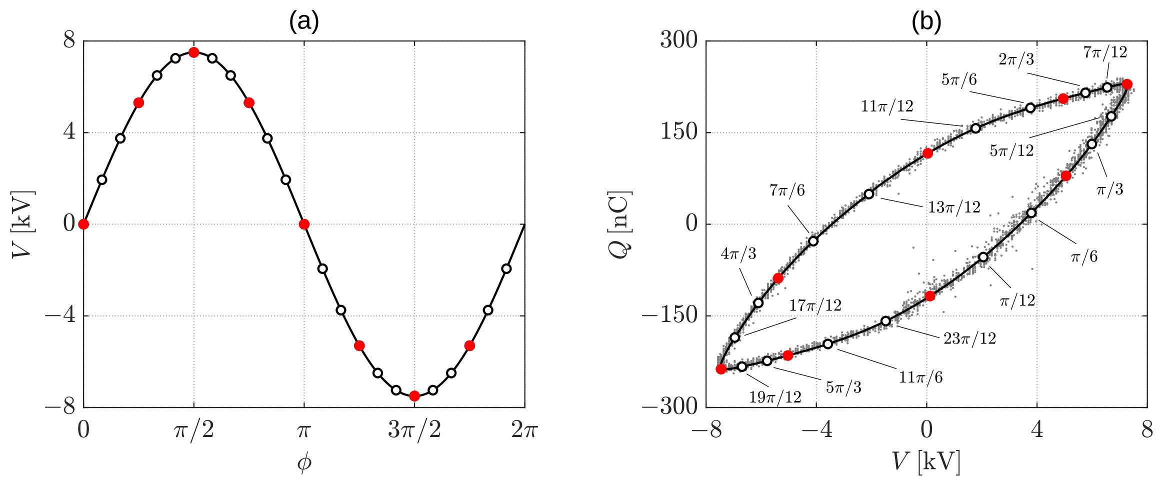

Figure 4.7: Phase-resolved discharge cycle decomposition in 24 phase positions; White dots represent the additional data points compared to the 8 phases decomposition (red dots). (a) Decomposition of the plasma actuator voltage wave form in 24 phase positions; (b) Measured phases on the $Q-V$ cyclogram.

Even though the most accurate operating frequency is found for one cycle of interval, the laser can be operated at a maximum frequency of $f_l = 5000$ Hz. Due to the accuracy of the synchronizer software $t \pm 5 \times 10^{-9}$ s, two and three cycles of interval between acquisitions also enable the accurate positioning of the laser and camera signals. Nonetheless, the operation with two cycles of interval demands high acquisition rate of the camera and thus reduces the image resolution. Therefore, the laser and camera were operated at an acquisition rate of one phase per each three cycles of actuation. This setting enables the camera to operate at high resolution of 1024×512 px^2 and an appropriate object distance. In addition, it provides the same final resolution of previous phase decomposition strategy (96 px/mm). The recording system comprises the same configuration of the first set of experiments (see figure 4.6). Moreover, by increasing the number of phase positions, the number of image pairs per phase is decreased to a third (227 image pairs per phase) compared to the previous strategy. To overcome this discrepancy the velocity data for each free-stream velocity was acquired three times in a row providing a total of 682 image pairs per phase.

4.1.5 Experimental Procedure

The plasma body-force field in the presence of external flow remains yet to be quantified. Hence, the first consideration is the velocity range in which the actuator will operate. It is decided as a first approach and due to lack of information about the body-force field determination under the influence of external airflow to operate the actuator in a laminar BL with velocities up to $U_\infty = 20$ m/s. Specifically, in the first set of experiments are conducted in the following free-stream velocities $U_\infty = [0, 5, 10, 15, 20]$ m/s. Intermediate steps of U_∞ were introduced in the second set, for free-stream velocities $U_\infty = [2.5, 7.5]$ m/s. The BL fundamental characteristics for the considered free-stream velocities are summarized in section 4.3.2

The experimental procedure is defined to guarantee best possible comparability between power consumption, current and body-force field for the different free-stream velocities. The approach proposed in the present work is to record electrical and velocity data sequentially. Due to expected fluctuations in power consumption measurements, electrical information is acquired three times per velocity, before, during and after the PIV measurement. To ensure consistency, it is set a one minute gap between electrical measurements and ten seconds of actuation prior to the recording. On the other hand, the current signal is only recorded once per velocity because the goal is only to evaluate the behaviour of the plasma-discharge events. Similarly, the actuated and non-actuated velocity fields are also recorded only once per base-flow velocity. Table 4.4 exemplifies the test matrix used during the experiments for each different base flow velocity, where PA# stands for the actuator used in each set of experiments. In the current work two actuators are manually fabricated, for the 8 and 24 phases decomposition.

PA #	U_∞	Case		PIV	Power consumption (P)	Current (I)
		Plasma	Base flow			
n	U_i		x	x		
n	U_i	x			x	
n	U_i	x		x	x	
n	U_i	x			x	
n	U_i	x				x

Table 4.4: Sequential test matrix used for electrical and velocity data acquisition per each base flow velocity.

The experiments were repeated three times per each velocity in each set. The importance of acquiring different sets for each free-stream velocity is that it provides information on the reproducibility of the body-force fields. In addition, it is expected to guarantee statistical significance of the electrical data. Due to the small number of image pairs per run in the 24 phase resolution strategy and to match the 8 phase resolution number of image pairs, two additional velocity measurements are performed for the actuated velocity field. In this case, each three runs are considered one case for purposes of body-force field determination.

4.2 Data Processing

The determination of the velocity field was achieved by processing the raw images obtained with PIV measurements. The defined camera setup enables to capture accurately the tracer particles, however it might also record reflections due to the laser and PMMA flat plate. In addition, it is expected the presence of background noise. One should notice that the background noise and reflections are systematically present in each raw image and are not randomly distributed from image to image.

In order to overcome this problem the raw images are evaluated using a mean filter in a pre-processing technique, consisting on calculating and subsequently subtracting the image mean from the raw images. Due to the double-frame operation of the acquisition settings, the images are decomposed in first and second frame from which a mean image is calculated separately. One should notice that the distribution of the tracer particles over the raw image do not influence the mean image. Thus the technique efficiently minimizes sources of erroneous velocity vectors such as reflections and background noise.

4.2.1 PIVview analysis software

The instantaneous velocity vectors were obtained by processing the filtered images using the software PIVview $3C$ version 3.8. Taking into account the double-frame operation, the software is able to compute the velocity vectors, thus the velocity field with respect to each image pair. The time-averaged velocity field is then obtained by averaging the instantaneous fields. For the phase-resolved velocity field, the instantaneous fields are averaged for each single phase position.

The reference axis together with the image resolution is defined using the calibration target, see figure 4.8. Regarding the reference axis, the downstream edge of the exposed electrode was defined as the origin of the coordinate system (x, y). The resolution is computed using the camera calibration image according with the length and image resolution (see figure 4.8).

In addition, a parameter file is required to define the processing specifications such as filters, algorithm, interrogation area and outlier detection. Regarding the filters, a low and high pass filter were included to enhance the image quality and facilitate the particle detection algorithm of the software. The interrogation method is based on a multi-grid refinement with initial and final sampling window of 64×64 and 32×12 pixels with $75 \times 50\,\%$ overlap, respectively. To determine the sub-pixel displacement a least squares Gaussian fit (3×3) was also included [51]. Based on these parameters, the software is able to detect and calculate the particle displacement, hence the velocity vectors between the two images of one image pair. However, the algorithms might calculate non-physical vectors due to erroneous particle displacement correlation. In order to validate the velocity computation, outlier detection filters were included. The evaluation was performed by a normalized median test and maximum particle displacement (Δ_{max}) [51]. The maximum displacement (Δ_{max}) is estimated according with equation (4.2), where Δt_L represents the distance between laser pulses. Its value was properly evaluated for each case according with the external flow velocity. Erroneous vectors are replaced using an 5 passes outlier replacement scheme based on interpolation.

$$\Delta_{max} = Resolution \times U_{max} \times \Delta t_L. \tag{4.2}$$

The validation process of the PIV evaluation provides the information regarding the outliers in each velocity field. In figure 4.9, the validation process for the case with $U_\infty = 20\,$m/s report is shown for

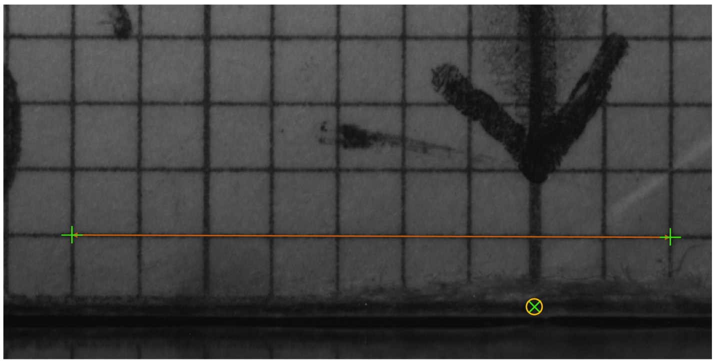

Figure 4.8: Calibration target picture comprising the reference axis origin and the image resolution determination. Reference xy-axis orientation flipped (x positive right to left) compared to the results shown in chapter 5.

a total of number of image pairs. In contrast, to the base flow case, with the presence of the plasma, the velocity field will be subjected to significant velocity gradients that might compromise the vector's calculation. Hence, only a plasma case with external flow $U_\infty = 20$ m/s is shown in figure 4.9 for total of number of image pairs $\#N$. The results indicate the percentage of outliers to be $< 1\%$ and interpolated data below $< 2.5\%$ which is in agreement with literature [51]. The results of the remaining cases are found to be within the same range.

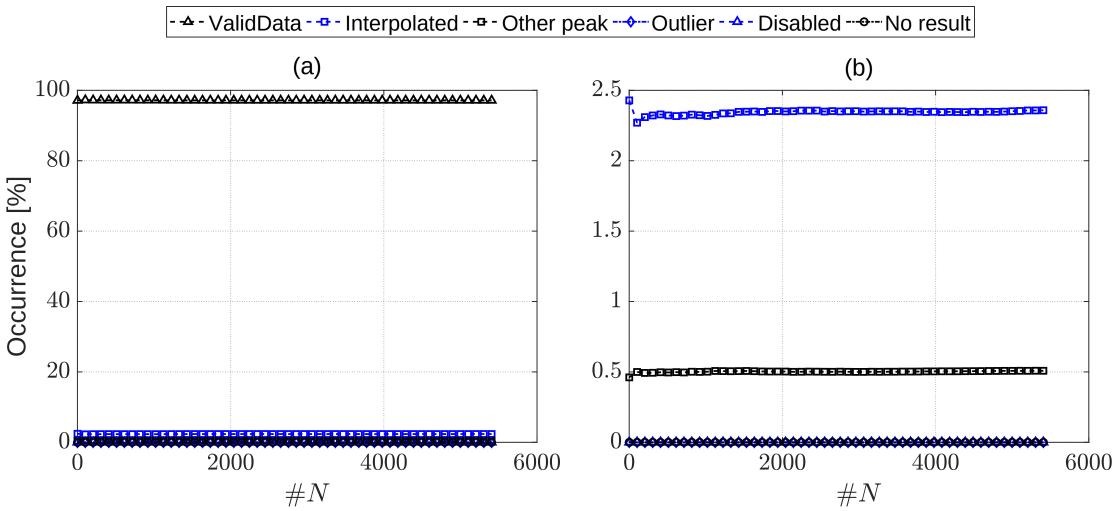

Figure 4.9: Outlier detection analysis output comprising: Valid data, interpolated, other peak, outlier, disabled and no result with respect to the number of considered image pairs $\#N$ for $U_\infty = 20$ m/s. (a) Percentage of occurrence of velocity vectors computation according with outlier detection classification in each image pair; (b) Zoom-in of the lower percentage of occurrence region < 2.5 % .

4.2.2 Velocity statistical significance

The plasma-actuator induced airflow is well-known for its highly unsteady behaviour during the discharge cycles [17, 23, 29, 34]. Additionally, the velocity information acquisition system has limited buffer capacity. This implies that the velocity fields must converge within the available number of image pairs to guarantee statistical significance and subsequently compute the mean velocity fields. One should notice that the phase-resolved velocity field is given by the average of the instantaneously acquired fields of a single phase angle. Similarly, to obtain the time-averaged velocity field, all instantaneous velocity fields are averaged. Literature comprises different techniques to verify the convergence of the velocity fields, see e.g. [28, 29]. In the present work, the average fluctuations of the velocity field are used as a convergence parameter [28]. The time-averaged and phase-resolved velocity fields (u_i) and standard deviation (σ_{u_i}) are given by equations (4.3) and (4.4), respectively.

$$u_i(x, y) = \frac{1}{N} \sum_{k=1}^{N} U_i(x, y, \Delta t_k). \tag{4.3}$$

$$\sigma_{u_i} = \sqrt{\frac{1}{N-1} \sum_{k=1}^{N} [U_i(x, y, \Delta t_k) - u_i(x, y)]^2}. \tag{4.4}$$

The velocity field in quiescent air features characteristic regions that are relevant to verify the convergence [28, 29]. Figure 4.10 illustrates the velocity field and considered regions: maximum velocity (MV) regions which is situated near the bulk of the plasma, the suction region above the exposed electrode (S), shear layer (SL) and downstream the fully developed wall jet (WJ).

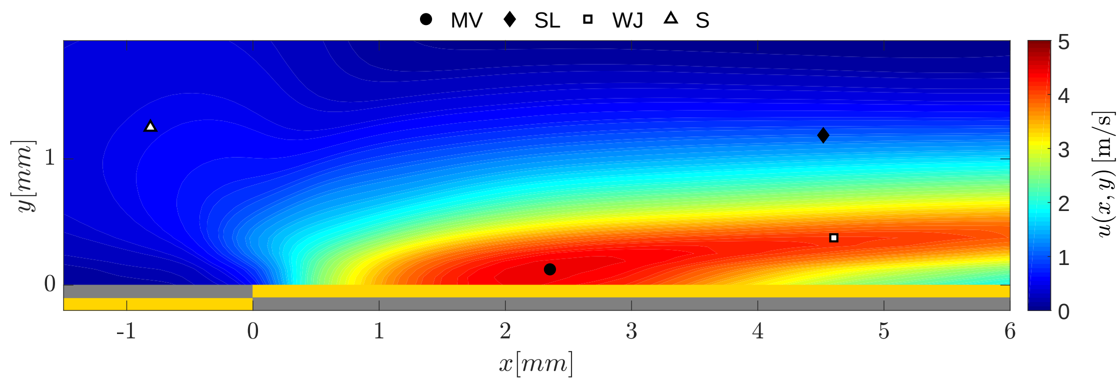

Figure 4.10: Plasma actuator horizontal velocity field $u(x, y)$ characteristic regions in quiescent air: maximum velocity (MV), shear layer (SL), wall jet (WJ) and suction (S). Electrodes and dielectric layers locations represented in grey and yellow, respectively.

According with the expressions (4.3) and (4.4), and above mentioned characteristic regions, a convergence study was conducted for the time-averaged and phase-resolved analysis. The results for quiescent air are shown in figure 4.11. Moreover, for simplicity the analysis for the phase-resolved data shown in figure 4.11 (b) exhibits only 8 of the total number of phases (24) and only for the suction region.

The results indicate that for both approaches the number of image pairs is sufficient to guarantee statistical significance. Nonetheless, the suction region is found to comprise a high value for the average fluctuation in the velocity field compared to the other regions. This behaviour is attributed to the highly unsteady behaviour of the plasma discharge that leads to high fluctuations near the suction region. Similar results were presented by Kriegseis et al. [28]. The remaining cases were also found to convergence within the available number of image pairs for both time-averaged and phase-resolved strategies.

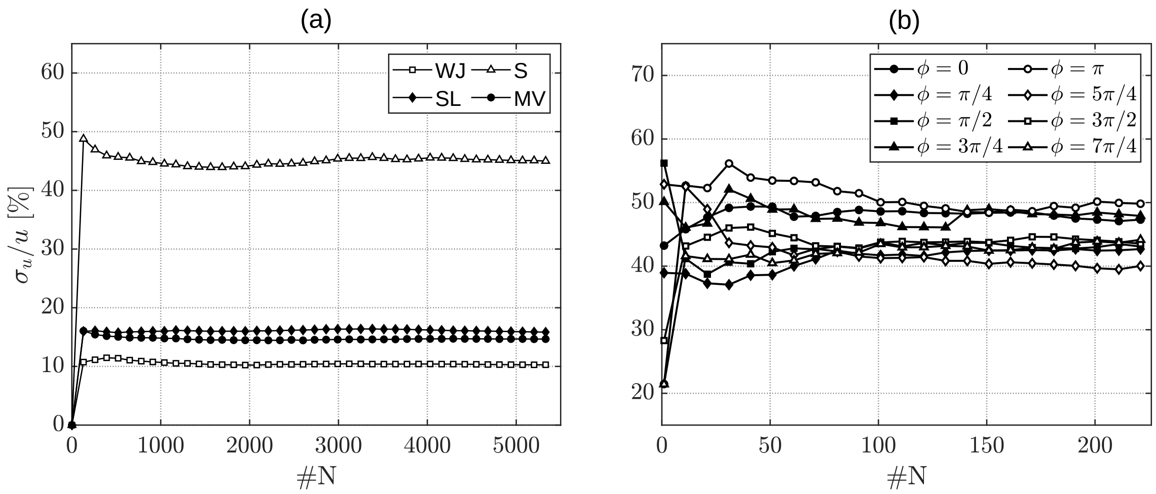

Figure 4.11: Convergence study of the time-averaged and phase-revolved relevant regions of the velocity field with respect to the number of considered image pairs $\#N$ for $U_\infty = 0$ m/s. (a) Time-averaged mean velocity fluctuations (σ_u/u); (b) Phase-resolved velocity fluctuations (σ_u/u) evolution at the suction (S) region.

4.3 Post processing

4.3.1 Uncertainty quantification

Electrical data

The electrical information on the plasma discharge cycle is characterized using both power consumption and current. The latter is measured with the purpose of analysing the plasma-discharge events rather than calculating the power consumption. Thus, it is not considered in the following analysis and the results are shown in section 5.1.2. Regarding the power consumption, the previously introduced equation (2.2) provides the average power consumption of one discharge cycle using electric-charge technique [7, 8]. In addition, the sampling rate is accounted for the power consumption determination. Accordingly, the power consumption of the actuator is given by the average of the total number of measured cycles, see section 4.1.3. Equation (2.2) is then replaced by expression (4.5).

$$P = \frac{f}{K} \sum_{k=1}^{K} \oint_k C_p V_p(t) dV. \tag{4.5}$$

The uncertainty is determined considering the cycle-to-cycle standard deviation. One should notice that this approach enables the determination of the standard deviation related to the power consumption in each measurement. Nonetheless, external factors are not accounted for. In order to get into detail of external sources of uncertainty the reader should refer to Ashpis et al. [52]. Equation (4.6) represents the uncertainty with respect to each power consumption measurement σ_P, where P_i represents the power consumption associated with each individual discharge cycle and P average power consumption of each data acquisition. For comparison and clarity reasons, the results are only introduced later in the power consumption analysis section 5.1.1.

$$\sigma_P = \sqrt{\frac{1}{K-1}\sum_{k=1}^{K}[P_i(k) - P]^2}. \tag{4.6}$$

Velocity field

The velocity field uncertainty quantification is performed using the strategy for time-averaged quantities presented by Sciacchitano and Wieneke [53]. The approach consists on determining the time-averaged velocity uncertainty field according to equation (4.7), where σ_u represents the standard deviation of the velocity fields and N the number of instantaneous velocity fields. Furthermore, the uncertainty relates to the time-averaged velocity field in each individual point.

$$U_{\overline{u}} = \frac{\sigma_u}{\sqrt{N}}. \tag{4.7}$$

The standard deviation is determined according to equation (4.8). The expression includes the velocity fluctuations ($\sigma_{u,fluct}$) and measurement errors ($\sigma_{u,err}$). The latter can be approximately given by the mean-square of the instantaneous velocity field uncertainty ($\overline{U_u^2}$) [53].

$$\sigma_u^2 = \sigma_{u,fluct}^2 + \sigma_{u,err}^2 \approx \sigma_{u,fluct}^2 + \overline{U_u^2}. \tag{4.8}$$

In the following, the uncertainty of the actuated BL velocity fields is presented. The results are shown for the minimum and maximum velocity with plasma actuation, see figure 4.12. For simplicity, the uncertainty of the non-actuated velocity fields is omitted.

Regarding quiescent air $U_\infty = 0$ m/s, the uncertainty is found to be maximum near the exposed electrode downstream edge $x = 0$ mm whereas the surrounding regions present significantly lower uncertainty. (see figure 4.12 (a)). This result can be anticipated due to the unstable character of the discharge cycle [17, 23, 29, 34]. One should notice that although only the time-averaged velocity is being considered, the velocity fluctuations produced by the discharge cycle are included in equation (4.7) by standard deviation σ_u. On the other hand, for $U_\infty = 20$ m/s, the velocity fluctuations within the BL lead to higher values of uncertainty. Near the surface, the results depict the higher values, however such an effect is attributed to the low number of particles and to the lower velocity region. The latter relates to the defined particle image displacement on the PIV cross-correlation algorithm which is different than the estimated velocity near the surface, see section 4.2.1. Nonetheless, the uncertainty is lower than < 4 % just above the surface layer. Outside the BL region, the uncertainty is very low as the velocity field is given by a rather constant free-stream velocity. The remaining cases are found to have an uncertainty within the range established by the minimum and maximum free-stream velocity with actuation. Similarly, the non-actuated BL is also found to be within the uncertainty of $U_{\overline{u}} = [2; 4]$ % with exception of the surface layer.

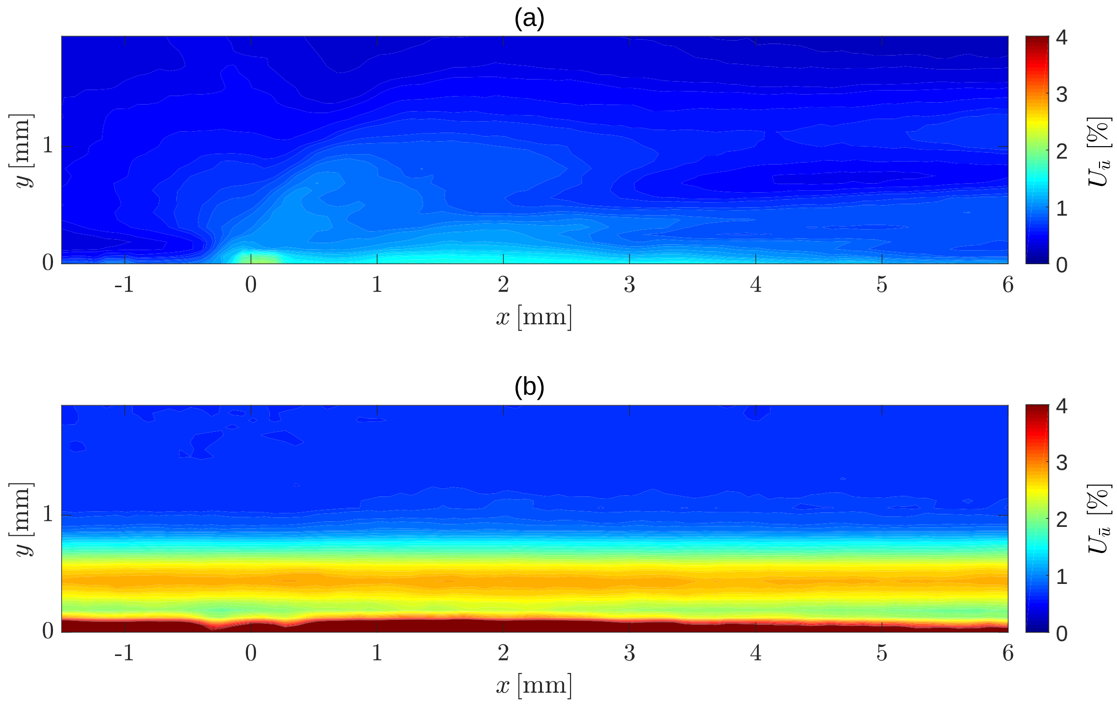

Figure 4.12: Horizontal velocity component (u) uncertainty quantification ($U_{\overline{u}}$). (a) Plasma actuation in quiescent air $U_\infty = 0$ m/s; (b) Plasma actuation in laminar BL flow at free-stream velocity of $U_\infty = 20$ m/s.

The propagation of velocity uncertainty is also considered by Sciacchitano and Wieneke [53]. However, the method relates the velocity with decoupled quantities such pressure distribution using the Monte Carlo simulations. In the present work, the body force and velocity can not be decoupled, hence the propagation of the uncertainty to the body-force field is not considered.

4.3.2 Boundary layer characterization

The non-actuated base-flow BL is characterized in order to determine in which conditions the plasma actuator is operated. Velocity information on the non-actuated BL at the considered external flow velocities is provided by PIV measurements, see section 4.1.5. The characterization is established by the integral BL parameters: BL thickness (δ_{99}), shape factor (H_{12}) [54]. The BL thickness is defined as the height at which the velocity is found to be $U(\delta_{99}) = 0.99U_\infty$ [54]. The shape factor (H_{12}) is related to the behaviour of the velocity profile. Hence, quantifies the state of the BL, whether laminar or turbulent. By definition, it is given by the ratio between the displacement thickness (δ^*) and momentum thickness (θ), according to equation (4.9) [54]. The upper limit of the integration domain is provided by δ_{99}. Furthermore, the operation within a BL requires the definition of the velocity felt by the plasma, which is considerably lower than the free-stream velocity (U_∞). Thus, a third parameter is introduced (U_0). The estimation of this velocity is defined as the average velocity at the plasma location along y-direction, see equation (4.10). The velocity profile is integrated up to the height of the body-force field (h). Results from Kriegseis et al. [28] are used as reference for the body-force field height (h). Similar strategy is presented by Pereira et al. [9]. The BL properties for the considered external-airflow velocities are summarized in table 4.5.

$$H_{12} = \frac{\delta^*}{\theta} = \frac{\int_0^\infty \left(1 - \frac{U(y)}{U_\infty}\right) dy}{\int_0^\infty \frac{U(y)}{U_\infty}\left(1 - \frac{U(y)}{U_\infty}\right) dy}. \tag{4.9}$$

$$U_0(U_\infty) = \frac{1}{h}\int_0^h U(y) dy. \tag{4.10}$$

U_∞ (m/s)	δ_{99} (mm)	H_{12}	U_0 (m/s)
2.5	3.49	3.23	0.87
5	2.87	3.26	1.86
7.5	2.18	3.27	3.43
10	1.99	3.38	5.06
15	1.56	3.48	9.14
20	1.43	3.55	12.18

Table 4.5: External boundary-layer fundamental characteristics without plasma actuation: free-stream velocity (U_∞), BL thickness (δ_{99}), shape factor (H_{12}) and average velocity at the plasma region (U_0).

The range of values of the shape factor illustrate that the plasma is operating in a laminar BL ($H_{12} > 1.5$) [54]. In addition, the high values are attributed to a decelerated flow regime - an adverse pressure gradient in the BL along the streamwise direction ($\partial p/\partial x > 0$).

Based on the global quantification of the external BL, the presence of an adverse pressure gradient is carefully analysed. One should notice that the body-force field determined with N.S.E. method neglects the pressure gradient. Hence, the pressure gradient must be evaluated properly otherwise the validity of the force determined with N.S.E. may be compromised. On the contrary, the V.E. approach should not be affected by such phenomenon (see section 3.1). The pressure gradient ($\partial p/\partial x$) is estimated using the previously introduced N.S.E. equations (eq. 3.1) with no plasma actuation ($f_i = 0$). The results for free-stream velocities of $U_\infty = 2.5$ m/s and $U_\infty = 20$ m/s are shown in figure 4.13 (a) and (b), respectively.

For low free-stream velocities, the maximum streamwise pressure gradient is found to be reasonably small (see figure 4.13(a)). On the other hand, the results clearly show a CV strip within the range $y = 0.5$ mm to $y = 1$ mm height with a significant pressure gradient for $U_\infty = 20$ m/s (see figure 4.13(b)). Furthermore, the values shown in figure 4.13(b) are in the same order of magnitude of the body-force field distributions presented by Kriegseis et al. [28]. Consequently, the flow field must be carefully analysed before calculating any body-force distribution using the N.S.E. approach. In the following section 4.3.3 strategies based on fluid mechanics fundamentals are analysed in order to minimize the impact of the base-flow BL pressure gradient on the plasma body-force field determination.

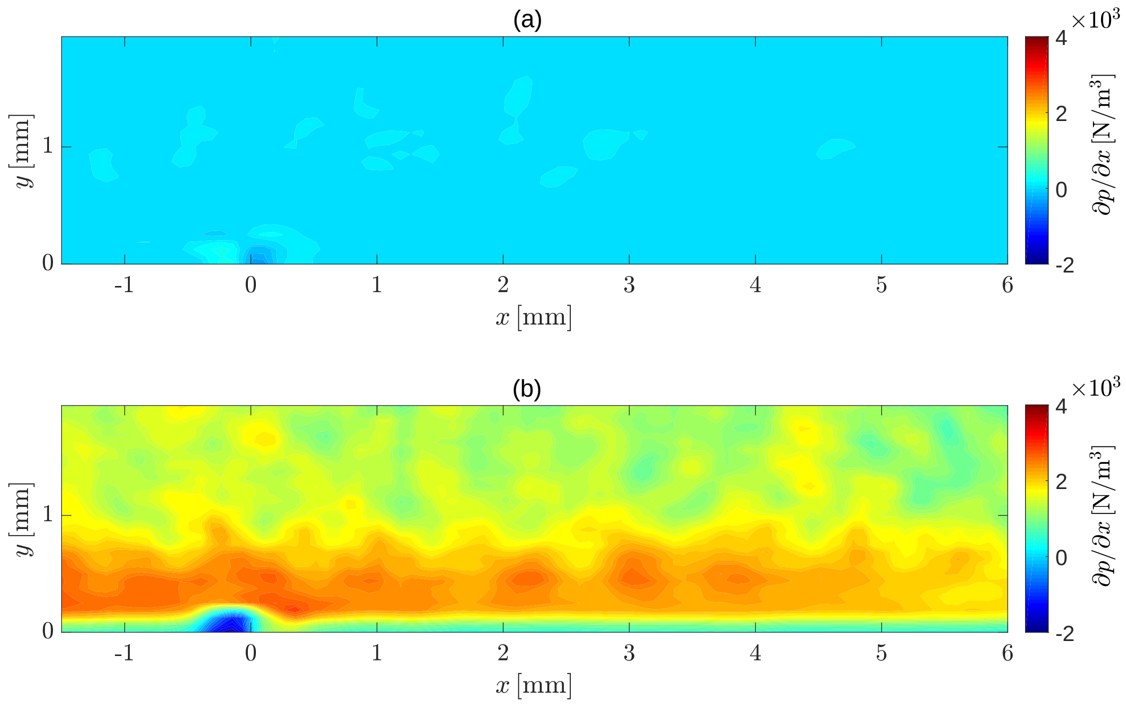

Figure 4.13: Baseline BL wall-parallel pressure gradient ($\partial p/\partial x$) distribution. (a) $U_\infty = 2.5$ m/s; (b) $U_\infty = 20$ m/s

4.3.3 Body force determination approach

The negligible pressure gradient assumption is already violated for the base flow (i.e. without plasma actuation), and thus it is expected to compromise the body-force determination. In the present work, two techniques are considered to minimize such an effect, however the problem is rather complex. It is noted that the body-force determination using the V.E. method should not be affected by the presence of an adverse pressure gradient (see section 3.1).

The first considered technique is to extract the plasma-induce velocity field simply by subtracting the non-actuated from the actuated flow field. The subsequent determination of the body-force field represents only the actuation of the plasma on the laminar BL flow. Based on such considerations and in order to obtain the plasma-induced velocity, the velocity field must be given by the difference between the actuated and non-actuated BL. Hence, the combination of two completely developed fluid motions. The induced velocity u_{pa} is then represented by equation (4.11), where U_{pa} and U_∞ represent the actuated and non-actuated velocity field, respectively. One should notice that U_{pa} contains both the velocity field U_∞ and plasma-induced velocity-field perturbations. In addition, the free-stream velocity U_∞ is assumed to be unchanged between two consecutive PIV measurements.

$$u_{pa} = U_{pa} - U_\infty. \tag{4.11}$$

The body-force field is obtained by replacing expression (4.11) in the previously introduced 2D N.S.E. (3.2a) and (3.2b). The temporal derivative of the velocity is not considered in the following discussion as it is expected not to have a significant contribution. For simplicity, only the mathematical manipulation of the N.S.E. along x-direction (3.2a) is shown. Similar procedure would apply for the y-direction. For clarity, the variables U_{pa} and U_{∞} are replaced by the index notation u_1 and u_2, respectively. In order to simplify, equation (3.2a) is split, expressions (4.12) and (4.13) represent the left-hand-side (LHS) and right-hand-side (RHS) of the initial equation, respectively. In addition, the variables u and v relate to the horizontal and vertical component of the velocity field, respectively.

$$fx_1 - fx_2 - \frac{\partial}{\partial x}(p_1 - p_2) \equiv RHS. \tag{4.12}$$

$$LHS \equiv \underbrace{\rho\bigg((u_1 - u_2)\frac{\partial(u_1 - u_2)}{\partial x} + (v_1 - v_2)\frac{\partial(u_1 - u_2)}{\partial y}\bigg)}_{\text{convective terms}} - \mu\bigg(\frac{\partial^2(u_1 - u_2)}{\partial x^2} + \frac{\partial^2(u_1 - u_2)}{\partial y^2}\bigg). \tag{4.13}$$

The main concern of superposing two completely developed flows is related with the non-linear convective terms [55]. Therefore, only the convective term is considered from now on, see equation (4.13). The expressions of the mathematical manipulation are shown in equations (4.14).

$$\begin{gathered} \rho\bigg\{\frac{\partial}{\partial x}(u_1^2 - 2u_1u_2 + u_2^2) + \frac{\partial}{\partial y}(v_1u_1 - v_1u_2 - v_2u_1 + v_2u_2)\bigg\}, \\ \rho\bigg\{\frac{\partial u_1u_1}{\partial x} - 2\frac{\partial u_1u_2}{\partial x} + \frac{\partial u_2u_2}{\partial x} + \frac{\partial v_1u_1}{\partial y} - \frac{\partial v_1u_2}{\partial y} - \frac{\partial v_2u_1}{\partial y} + \frac{\partial v_2u_2}{\partial y}\bigg\}. \end{gathered} \tag{4.14}$$

The superposition of the two fluid motions is not immediately valid as the non-linear convective terms might introduce additional cross terms i.e terms including the product between the actuated and non-actuated velocity fields. In order to superpose the two fluid motions, the non-linear inertial terms should vanish naturally [55]. However, in the present case the final expression of the convective terms includes new cross terms which are not included in the initial N.S.E. equation formulation (3.2a). Hence, the approach is not valid without further considerations. The new terms (NT) are highlighted in expression (4.15).

$$NT = \underbrace{2\rho\frac{\partial u_1u_2}{\partial x} - \frac{\partial v_1u_2}{\partial y} - \frac{\partial v_2u_1}{\partial y}}_{\text{New terms}}. \tag{4.15}$$

In order to overcome this problem a solution might be a linearisation strategy namely using the non-actuated base flow to linearize the N.S.E. equations, see e.g. Pereira et al. [56]. In a linearisation strategy the plasma induced flow is treated as a perturbation, and as such this approach is only valid for ($u_{pa}/U_{\infty} << 1$). For the considered free-stream velocities the condition $u_{pa}/U_{\infty} << 1$ does not apply. Although it might be applicable for large free-stream velocities, the plasma region is located within the BL where the velocity is considerably smaller than U_{∞}, hence it is not applicable for the current work.

A second strategy is proposed to minimize the impact on body-force determination with the N.S.E. of the adverse pressure gradient exhibited by the non-actuated BL. Experiments of Kriegseis et al. [28] and Benard et al. [17] indicate the hypothesis of having a negligible pressure gradient to be valid in quiescent-air conditions $U_\infty = 0$ m/s, see section 3.1.1 [18]. Therefore, it might be reasonable to assume that the presence of a baseline pressure gradient is not affected by the presence of the plasma discharge, at least for quiescent-air conditions. Consequently, the pressure gradient can be directly determined from the base-flow BL velocity field. With the N.S.E. approach, the plasma body-force field is estimated assuming a negligible pressure gradient. The true body-force production (fx_{pa}) can be then obtained by subtracting the pressure gradient from the body force. Hence, the effect of the base-flow pressure gradient can be accounted for on the body-force field. Again, the validity of such a method requires the independence of the pressure gradient from the plasma. For sake of simplicity, equation (4.16) is shown with the same index notation, where fx_1 represents the body-force field of the actuated boundary-layer with negligible pressure gradient and $\partial p_2/\partial x$ the baseline pressure gradient.

$$fx_{pa} = fx_1 - \frac{\partial p_2}{\partial x}. \tag{4.16}$$

It should be remarked that the N.S.E. solution subtraction does not involve any superposition of fluid motion but a subtraction of two solutions of the N.S.E. (3.2a) which is a valid approach. In the following chapter 5 the method will be carefully analysed and quantified for the tested free-stream velocities (U_∞).

Chapter 5

Results

In this chapter the results are shown and interpreted, namely, electrical, time-averaged and phase-resolved body-force fields.

5.1 Electrical characterization

5.1.1 Power consumption

The power-consumption analysis is performed using the electric-charge method and subsequently calculated using equation (4.5) [7, 8], see also sections 2.3 and 4.1.3. The results are presented in non-dimensional form P/P_0, where P represents the averaged power consumption for a given free-stream velocity and P_0 the averaged power consumption in quiescent air. In order to guarantee statistical significance, the power consumption measurements are averaged for each free-stream velocity (see subsections 4.1.3 and 4.1.5). Additionally, the standard deviation (σ_P) associated to the determination of the power consumption is included as error bars (see equation 4.6). The results are shown on figure 5.1(a) for the tested range of free-stream velocities.

The results do not show a clear variation of the power consumption for the considered free-stream velocities. Data points shown on figure 5.1(a) exhibit both an increasing or decreasing behaviour without providing a clear trend. In addition, the variation is estimated to be in a range of $\pm 2\%$ which is within the standard deviation. Accordingly, the power consumption is considered to be virtually constant for the tested free-stream velocities. Further analysis is provided by the direct comparison of the $Q - V$ cyclogram between quiescent air $U_\infty = 0$ m/s (blue data) and free-stream velocity of $U_\infty = 20$ m/s (red data) shown on figure 5.1(b). As expected, the cyclogram distribution is similar for the two considered cases. The minor variation of power consumption is not sufficiently large to produce visible changes on the cyclogram shape. Additionally, the results resemble the findings of Pereira et al. [9] where a constant power consumption behaviour was found for free-stream velocities up to $U_\infty = 60$ m/s in co-flow configuration. In contrast, experiments of Kriegseis et al. [30] evidenced a power consumption decrease of about 3% already for $M_\infty = 0.1$, see section 3.2. The different experimental results are attributed to the orders-of-magnitude higher temporal resolution of the acquisition device used by Kriegseis et al.

[30], when compared to the present study and Pereira et al. [9]. Drops of power consumption in the order of 1% require to capture the points near the peak-voltage locations, i.e. the two sharp ends of the $Q - V$ cyclogram, precisely. Furthermore, the linear law for thrust-power relation reported in literature indicates that such a variation of power consumption is expected to have a negligibly small effect on the produced integral force F_x [8, 16].

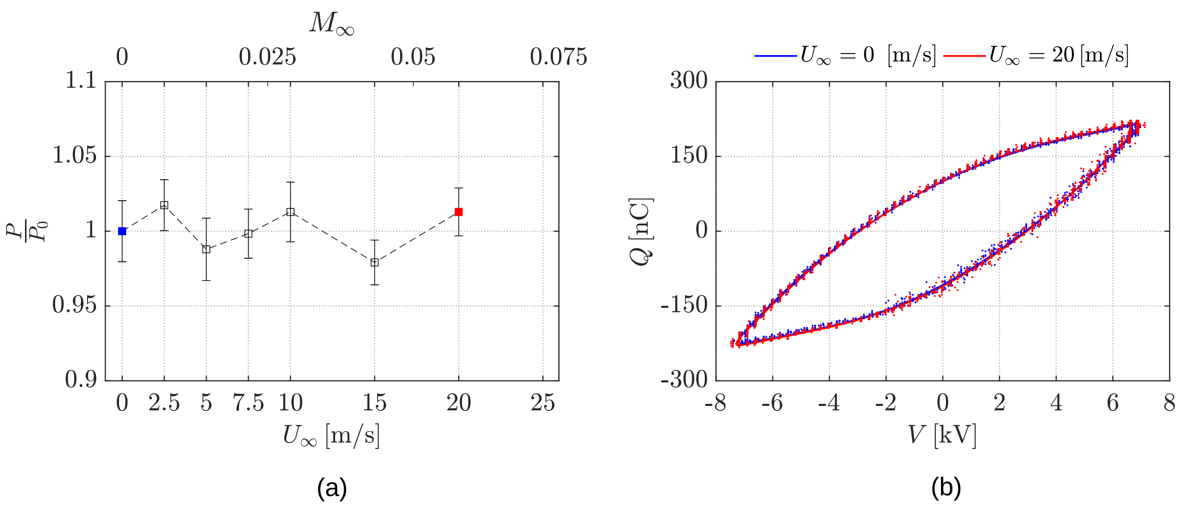

Figure 5.1: Power consumption analysis. (a) Relative power consumption based on P_0 quiescent air $U_\infty = 0$ m/s for increasing free-stream velocity U_∞; (b) Lissajous figure ($Q - V$ cyclogram) comparison for quiescent air (blue data) and $U_\infty = 20$ m/s (red data).

5.1.2 Current

The current measurements performed for the considered free-stream velocities are only shown for quiescent-air conditions and free-stream velocity of $U_\infty = 20$ m/s. The current signal of a single discharge cycle (blue data $U_\infty = 0$ m/s; red data $U_\infty = 20$ m/s) is superposed to the $Q - V$ cyclogram shown on figure 5.2 in order to study the discharge phenomena for different free-stream velocities. The lower and upper branch of the cyclogram represents the positive and negative-going half cycle, respectively.

In general, the current behaviour on the positive-going half cycle features large peaks (streamer discharge) whereas the negative-going half cycle is expected to produce smaller current peaks (glow discharge) [17, 21, 23], see also section 2.2. However, in the present study the positive-going half cycle features only weakly enhanced current peaks compared to the negative counterpart, with the negative-going half cycle being somewhat irregular compared to literature. Such a behaviour might be attributed to the low vertical resolution used to acquire the current signals compared to the experiments of Benard et al. [17]. In addition, the results clearly show the regions where the discharge quenches before entering in the subsequent discharge regime by the no-current zones (dashed line). The discharge collapses at the end of both positive and negative-going half cycles, corresponding to the phase positions $\phi =$

$\pi/2$ and $\phi = 3\pi/2$, respectively. Subsequently the discharge enters the dark period (no plasma) also identified by the region of cold capacitance (C_0), see section 2.3 [36]. The beginning of each following half-cycle is indicated by the occurrence of new current peaks. By analysing the so-called 'dark period' [57], one might extract qualitative information about the phase topology of the forcing mechanism. As the current is found to be null during the periods $6/12\pi \leq \phi \leq 10/12\pi$ and $19/12\pi \leq \phi \leq 22/12\pi$, the instantaneously produced local and integral force F_x is expected to be identical to zero (see section 5.2.2). Moreover, the similarities between the current-signals distribution for the two considered free-stream velocities evidences that the onset in each half-cycle is found for a constant phase position independently of the free-stream velocity.

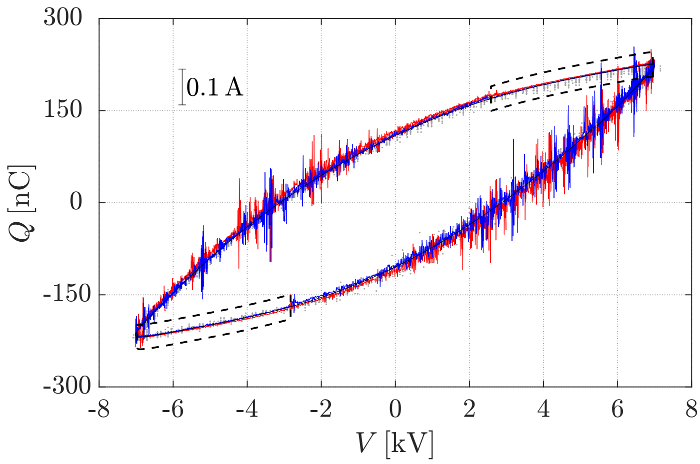

Figure 5.2: Lissajous figure ($Q - V$ cyclogram) in quiescent air $U_\infty = 0$ m/s (black solid line) superposed with the current signals I in quiescent air $U_\infty = 0$ m/s (blue data) and $U_\infty = 20$ m/s (red data).

5.2 Plasma Body-force fields

5.2.1 Time-averaged body force

Time-averaged volume-force generation of the present plasma actuator configuration is first analysed in quiescent air $U_\infty = 0$ m/s. The body force is determined using both N.S.E. and V.E. methods according to equations (3.2a) and (3.6), respectively. The horizontal component of the body-force field distributions $f_x(x, y)$ are shown in figures 5.3 (a) and (b) for N.S.E. and V.E. approach, respectively.

Analysis of the results obtained with both methods determined the body force distribution to be dominated by a strong positive volume-force generation immediately downstream of the exposed electrode $x = 0$ mm that extends in both x-direction and y-direction. Further downstream, the force distribution magnitude decreases significantly with a negative volume force appearing near the surface. Such a result might be attributed to the plasma self-induced drag [13, 14, 28, 34], see also section 2.4. As the convected fluid elements evolve downstream, viscous effects start to appear, hence decelerating the plasma-induced airflow gradually. Accordingly, the velocity gradient $\partial u/\partial x$ results in a negative contribution to the body force, thus leading to a negative volume-force estimation. To further characterize the body-force generation the source terms of equations N.S.E. (3.2a) and V.E. (3.6) are carefully evaluated. The convective and diffusive contribution are shown on figures 5.4 (a)-(b) for N.S.E. and on figures 5.4 (c)-(d) for V.E. method. The contribution of the temporal term $\partial u/\partial t$ is found to be insignificant, hence it is not shown [17]. The analysis of each component evidences a strong dominance of the body-force field reflected in the convective acceleration, which may be anticipated as the plasma actuator is responsible for producing strong velocity gradients [17, 28, 29]. Furthermore, the volume-force production along y-direction is analysed for quiescent air using the N.S.E. method, see figure 5.5. Analysis of figures 5.3(a) and 5.5 clearly demonstrates that the plasma body-force field is dominated by the streamwise component $f_x(x, y)$, as the force distribution along y-direction is found to be one order of magnitude smaller. The results are in compliance with the findings of Benard et al. [17] and Kriegseis et al. [28]. Previous experimental studies evaluated the V.E. method assumption by determining the ratio of the force gradients $\partial f_y/\partial x$ and $\partial f_x/\partial y$ according to N.S.E. (3.2b) and (3.2a) and subsequently determining the spatial derivatives. The result is shown on figure 5.6, in addition the 10% isoline of the body-force field $f_x(x, y)$ is included to guarantee comparability [28]. As evidenced by Kriegseis et al. [28] the ratio of the force gradients is found to be ≤ 1 in magnitude within the isoline except for scattered regions. Hence, it is reasonable to assume the V.E. assumption to be valid for quiescent-air conditions, see also section 3.1.1.

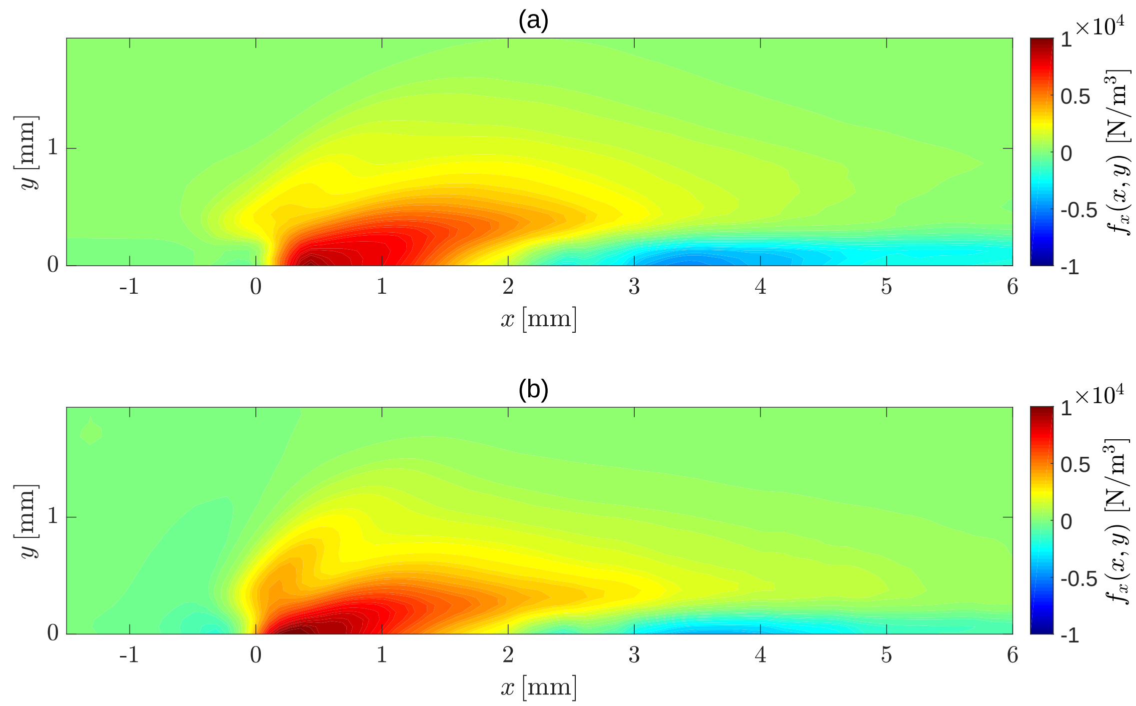

Figure 5.3: Plasma time-averaged horizontal body force distribution $f_x(x, y)$ in quiescent air $U_\infty = 0$ m/s. (a) According to N.S.E. (equation 3.2a); (b) According to V.E. (equation 3.6).

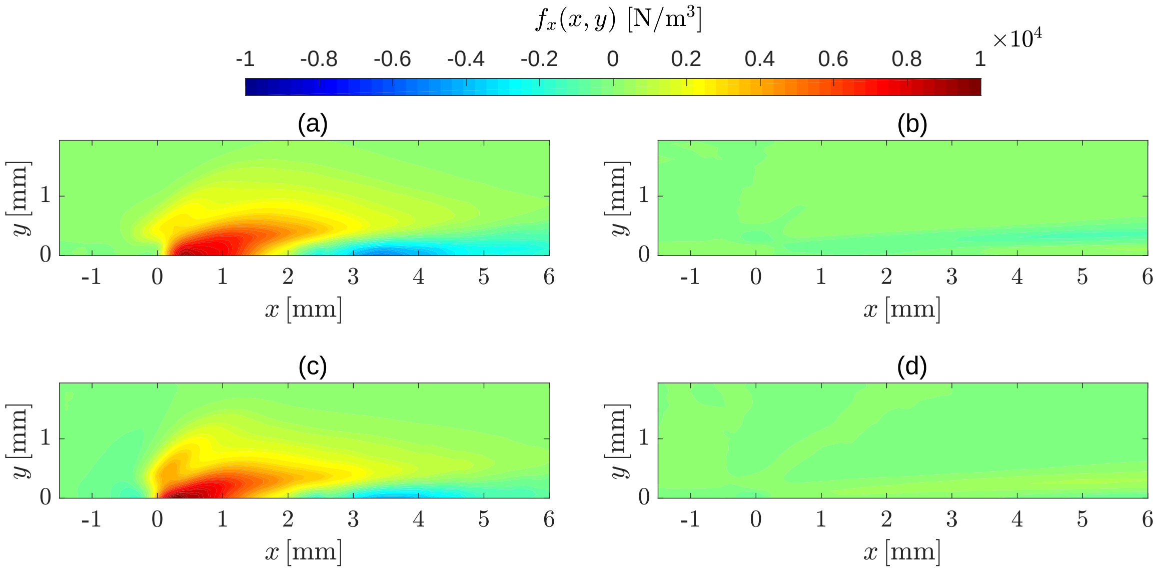

Figure 5.4: Contribution of the convective and diffusive terms to the spatial distribution of the force $f_x(x, y)$. (a)-(b) convective and diffusive term according to N.S.E. (equation 3.2a): $\rho\left(u\frac{\partial u}{\partial x} + v\frac{\partial u}{\partial y}\right)$, $\mu\left(\frac{\partial^2 u}{\partial x^2} + \frac{\partial^2 u}{\partial y^2}\right)$; (c)-(d) convective and diffusive terms according to V.E. (equation 3.6): $\int_0^\infty \rho\left(u\frac{\partial w}{\partial x} + v\frac{\partial w}{\partial y}\right)$, $\int_0^\infty \mu\left(\frac{\partial^2 w}{\partial x^2} + \frac{\partial^2 w}{\partial y^2}\right)$

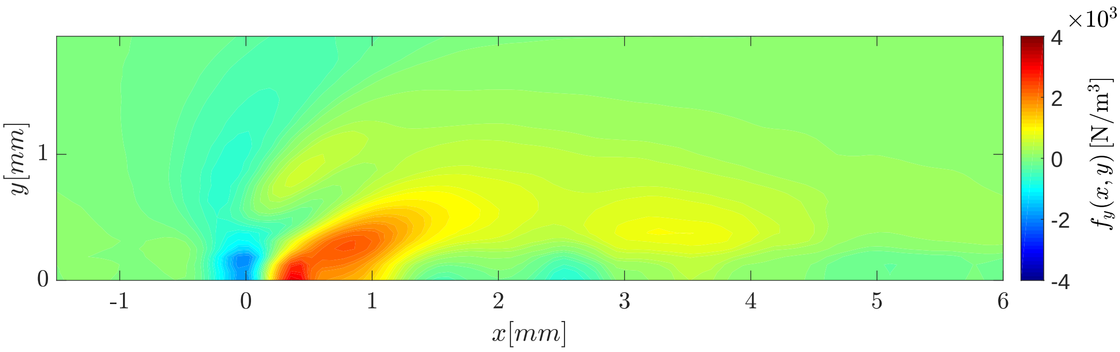

Figure 5.5: Plasma time-averaged vertical body force distribution $f_y(x, y)$ in quiescent air $U_\infty = 0$ m/s according to N.S.E. (equation 3.2b).

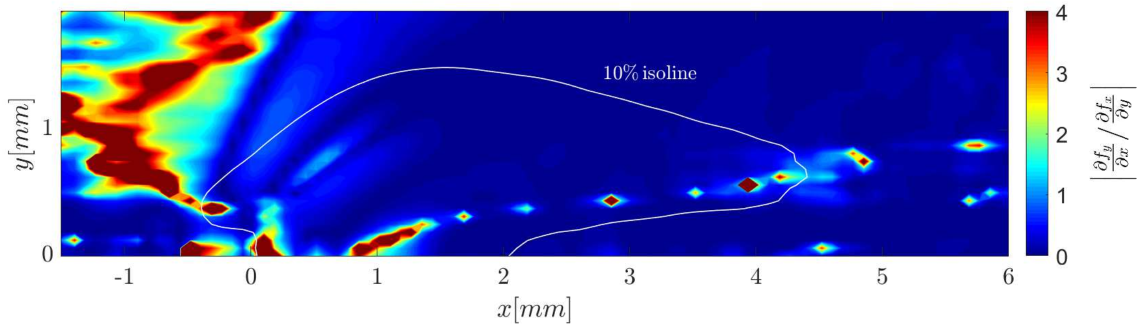

Figure 5.6: Ratio of force gradients $\partial f_y/\partial x$ and $\partial f_x/\partial y$ determined according to N.S.E. (equation 3.2a); white solid line - 10% isoline of the body-force field $f_x(x,y)$ in quiescent-air conditions.

Direct comparison between body-force fields shown on figures 5.3(a) and 5.3(b) evidences a similar spatial distribution of the $f_x(x,y)$ regardless of the estimation method. Nonetheless, mild differences can be detected, on one hand, the V.E. approach appears to estimate a larger area of the maximum magnitude region near the edge of the exposed electrode $x = 0$ mm than the N.S.E. On the other hand, the negative volume force generation is more pronounced when using the N.S.E. approach. At this point, no conclusion can be made regarding the most accurate method, however the resemblance between results shown on figures 5.3(a) and 5.3(b) indicates that both approaches lead to trustful results in quiescent air. Similar conclusions were drawn by Benard et al. [17] and Kriegseis et al. [28], see section 3.1.1. Furthermore, the identical actuator design and same operating conditions lead to results which are in very close compliance with the experimental study of Kriegseis et al. [28], see also section 3.1.1 figures 3.1(a) and 3.1(b).

The impact of the external flow on the spatial distribution of the body-force field $f_x(x,y)$ is evaluated for both N.S.E. and V.E. approach. The results for the time-averaged body-force field using the N.S.E. are shown in figures 5.7 (a)-(c) for different free-stream velocities $U_\infty = [5, 10, 20]$ m/s. The results for the remaining free-stream velocities $U_\infty = [2.5, 7.5, 15]$ m/s are presented in appendix A figure A.1. The baseline BL flow pressure gradient $\partial p/\partial x_i$ is subtracted, see section 3.1 equation (4.16). In general, the results evidence a strong impact of the baseline BL flow on the volume-force generation. Comparison between figures 5.3(a) and 5.7(a) indicates that the body-force topology is already significantly altered in both x-direction and y-direction for external-flow velocity $U_\infty = 5$ m/s. For higher free-stream velocities, a decisive decrease of the spatial distribution of the force $f_x(x,y)$ is determined, see figures 5.7(b)-(c). In addition, a negative volume-force region appears just above the bulk of the plasma $x = 0$ mm, which becomes more pronounced as the external BL velocity is increased up to $U_\infty = 20$ m/s. At the same time, a separated region from the most significant area of the body-force that yields a positive net force becomes noticeable for increasing free-stream velocity, see for instance figure 5.7(c) at $x \approx 0$ mm and $y \approx 0.5$ mm.

Regarding the V.E. method, the results are shown for increasing free-stream velocity $U_\infty = [5, 10, 20]$ m/s in figures 5.8 (a)-(c). The results for the remaining free-stream velocities $U_\infty = [2.5, 7.5, 15]$ m/s are presented in appendix A figure A.2. In contrast to the previously introduced results for the N.S.E. method, the estimation of the body-force field with the V.E. indicate that this method is less sensitive. Comparison with quiescent-air conditions, see figure 5.3(b), indicates that the impact of the external flow on the plasma body-force field appears to extend only to a minor part of the spatial distribution for free-stream velocities up to $U_\infty = 10$ m/s. Nonetheless, a remarkable effect on the body-force field is evidenced, on one hand, in the vicinity of the exposed electrode $x = 0$ mm the area of larger magnitude seems to become larger. On the other hand, the streamwise extend appears to shrink, see figures 5.3(b), 5.8(a)-(b). For higher free-stream velocity $U_\infty = 20$ m/s, shown on figure 5.8(c), the region of strong positive force increases in magnitude and area. However, the general features of the body-force field remain unchanged. As an aspect of significant importance, the verification step performed for quiescent-air conditions of the hypothesis $|\partial f_x/\partial y >> \partial f_y/\partial x|$ is not considered in the presence of external airflow [28], see figure 5.6. This is due to the high impact of the external flow on the body-force field estimation with N.S.E. method, that might indicate an oversimplification of the method. Furthermore, the V.E. body-force distribution shown on figures 5.8 (a)-(c) appears to be influenced by numerical error associated with the numerical operations and discretization domain, with large vertical stripes being identified on the contours. Similar conclusions were drawn by Benard et al. [17].

The contribution of the convective and diffusive terms to the body-force fields estimated with the N.S.E. (3.2a) and V.E. (3.6) is not presented as it resembles the results shown for quiescent air, see figure 5.4(a)-(d). The body-force field is dominated by the convective terms whilst the diffusive contribute only to a minor extent. In addition, the unsteady term is found to have an insignificant contribution to the body-force fields [17], further analysis is provided in section 6.1.

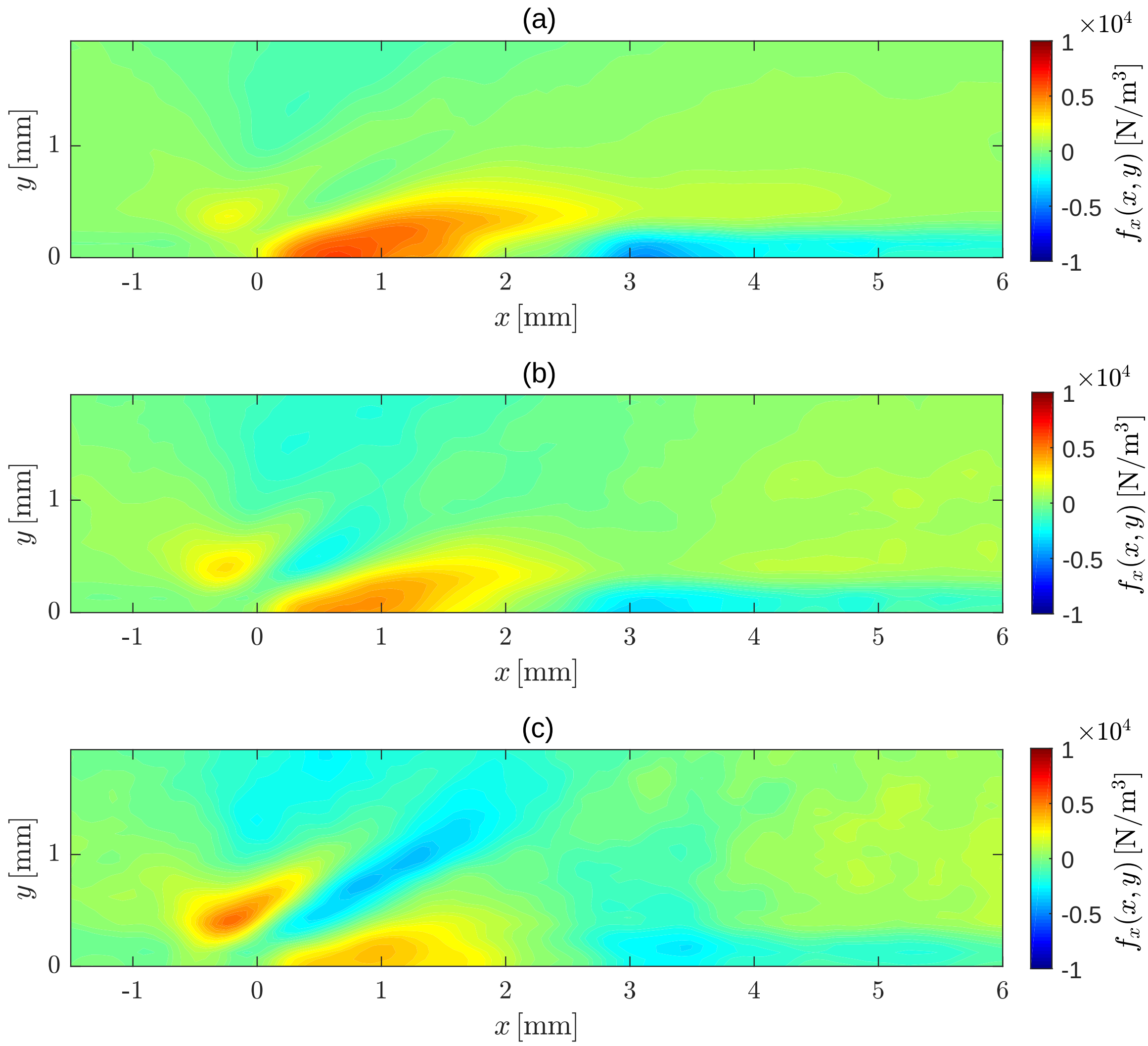

Figure 5.7: Horizontal component of the body-force field distribution $f_x(x, y)$ determined according to N.S.E. (equation 3.2a) and subtracting the base flow pressure gradient for different free-stream velocities U_∞. (a) $U_\infty = 5$ m/s; (b) $U_\infty = 10$ m/s; (c) $U_\infty = 20$ m/s.

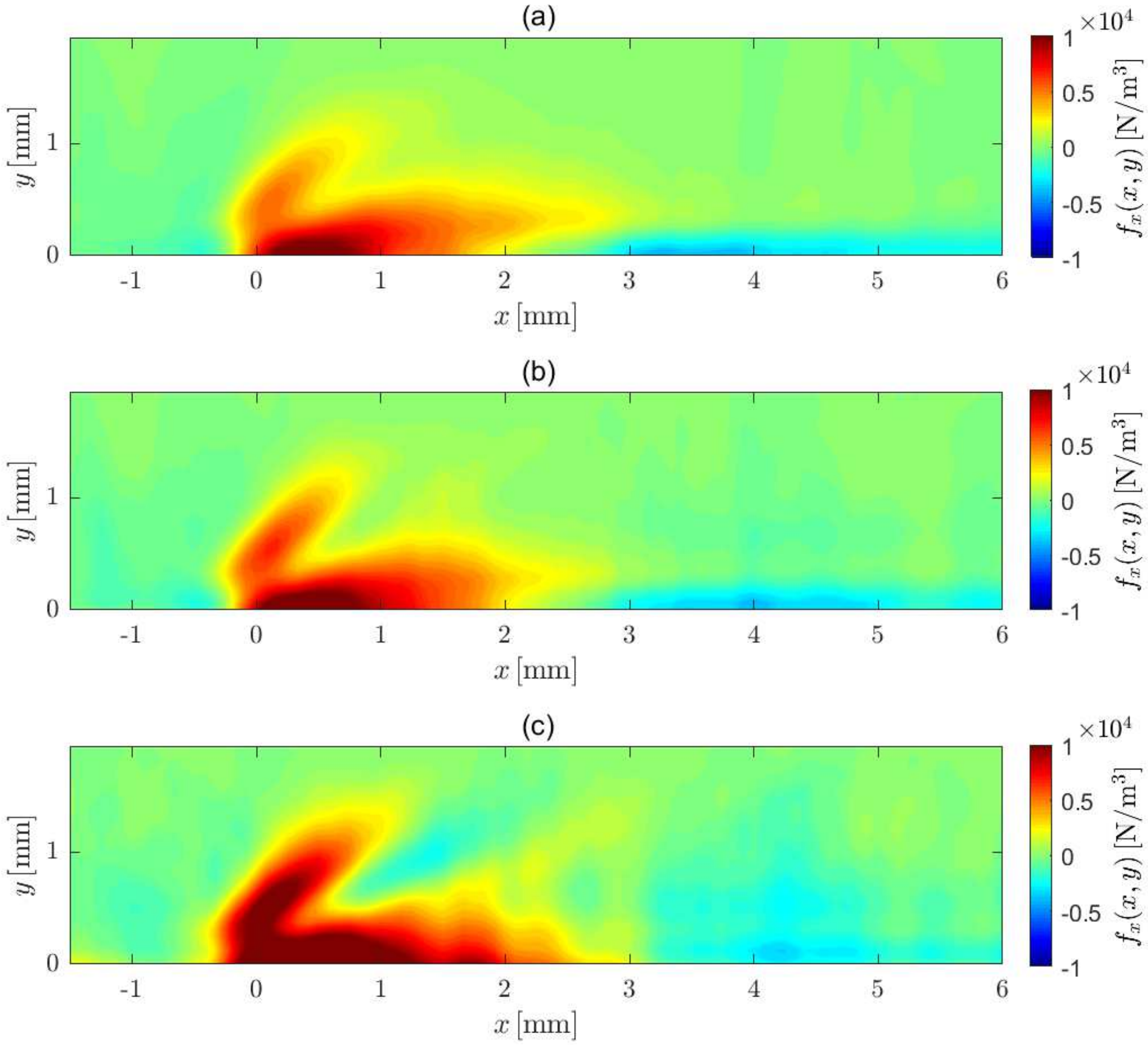

Figure 5.8: Horizontal component of the body-force field distribution $f_x(x, y)$ determined according to V.E. (equation 3.6) for different free-stream velocities U_∞. (a) $U_\infty = 5$ m/s; (b) $U_\infty = 10$ m/s; (c) $U_\infty = 20$ m/s.

Quantification of the global impact of the plasma volume-force generation F_x often termed 'Thrust' is determined by integrating the plasma body force over a CV [17, 27–29]. Literature comprises a strategy based on the 10% isoline of the body-force field f_x which represents the most significant domain of the spatial distribution [28], see figure 5.6. However, in the present study for increasing free-stream velocity U_∞, the shape of the 10% isoline of the body-force field presents significant changes specially for the N.S.E. approach (not shown). Hence, to have a comparison region independent of the body-force distribution, the integral is calculated over a rectangular CV defined by $x = [-1.5; 6]$ mm and $y = [0; 2]$ mm. The results are shown for the considered free-stream velocities on figure 5.9 for the N.S.E. (blue data) and V.E. (black data).

Analysis of the N.S.E. results evidence a clearly decreasing behaviour of the integrated body-force production with increasing free-stream velocity. Even though the baseline pressure gradient $\partial p/\partial x$ is taken into account (see section 4.3.3), a reduction in the estimated thrust of approximately 40% is evidenced already for $U_\infty = 2.5$ m/s. For free-stream velocities higher than $U_\infty > 10$ m/s, the continuously decreasing trend leads to negative values of the integral force F_x. On the other hand, the V.E. exhibits a decrease of about 17% from quiescent air to laminar BL flow operation at free-stream velocity $U_\infty = 2.5$ m/s. Nonetheless, the results tend to converge to a rather constant value for free-stream velocities up to $U_\infty = 15$ m/s. For the highest operating free-stream velocity $U_\infty = 20$ m/s, a mild increase is detected. In addition, the compliance between quiescent-air performance of both methods shown on figures 5.3 (a) and (b) is again verified by the integral determination. Specifically ,the N.S.E. approach force integral F_x is estimated to be only 1.5% larger in comparison with V.E. method.

In general, the negligibly small variations presented by the power consumption analysis shown on figure 5.1(a) indicate the electrical-to-mechanical conversion of the present plasma actuator remains unchanged for the tested free-stream velocities [8, 16, 27], see also section 5.1.1. Hence, the actuator is expected to produce almost the same amount of force for each free-stream velocity. Accordingly, the V.E. results shown on figure 5.9 correlate with electrical characterization, thus indicating only mild impact of the neglected $\partial f_y/\partial x$. On the other hand, the N.S.E. is significantly diminished with increasing free-stream velocity. Such a result evidences that the negligible pressure gradient $\partial p/\partial x$ might result in an oversimplification of the method. At this point, it must be noted the estimation of force obtained with N.S.E. (3.2a) and subsequently base-flow pressure-gradient subtraction according to equation (4.16) is questionable. This is because no physical phenomenon associated with imposing an external airflow on an AC-DBD plasma actuator may explain the change in direction of the plasma force produced. Further analysis on the impact of the pressure gradient is provided in chapter 6.

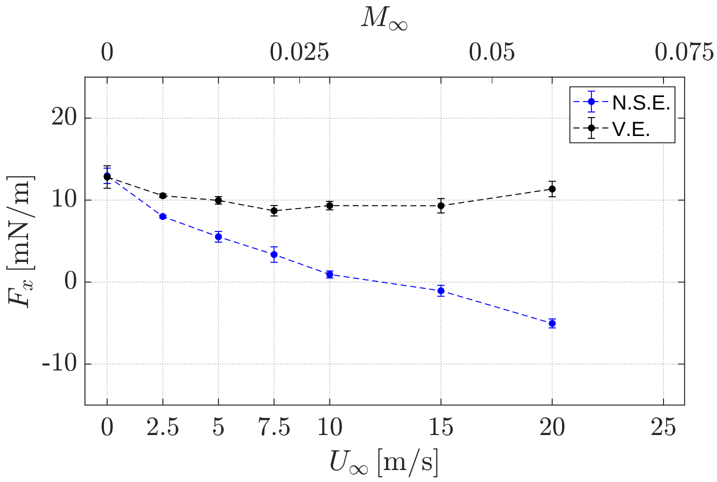

Figure 5.9: Integrated value of the time-averaged body-force field horizontal component F_x according to the CV $x = [-1.5; 6]$ mm $y = [0; 2]$ mm using the N.S.E. method (blue data) and V.E. method (black data) for the considered free-stream velocities U_∞.

5.2.2 Phase-resolved body force

The phase-resolved volume-force production determination strategy enabled to quantify the body force in 24 phases over a single discharge cycle (see section 4.1.4). Due to high resolution of the discharge cycle, the results are first analysed for quiescent air (8 phases). As mentioned before, the phase values for each data point considered in this analysis are coincident with the experiment of Kuhnhenn et al. [29], see also section 4.1.4. Similarly to the time-averaged results, the instantaneous body force is estimated using both N.S.E. and V.E. methods. The results are shown in figures 5.10 (a)-(h) using the N.S.E. approach and in figures 5.11 (a)-(h) for the V.E. approach. Figures 5.10 (a)-(d) comprise the positive-going half cycle whereas figures 5.10 (e)-(h) relate to the negative-going half cycle. The same order of the plots is applied for the V.E. approach results, shown in figures 5.11 (a)-(h).

The body-force field distribution clearly indicates the periodic oscillating behaviour of the discharge cycle for both methods (N.S.E; V.E.). The positive-going half cycle is initially dominated by a strong negative volume force (fig. 5.10(a); 5.11(a)) which gradually decreases in magnitude as the discharge evolves giving place to a positive volume force (fig. 5.10(d); 5.11(d)). On the other hand, the negative-going half cycle is responsible for producing an initially strong positive volume force $\phi = \pi$ (fig. 5.10(e); 5.11(e)) which then starts to decrease in the subsequent phase positions. The results resemble the findings of Benard et al. [17] and Kuhnhenn et al. [29]. In addition, the source-terms contribution is analysed. In contrast to the time-averaged body force, the temporal term has a major contribution to the body-force field, thus it is included in the following analysis [17, 29]. For simplicity, the results are shown for one phase position $\phi = 5\pi/4$ and only for the N.S.E. method according to equation (3.2a). Figure 5.12 (a)-(d) depicts the body-force field, temporal, convective and diffusive term, respectively. The analysis of each component evidences that the temporal term dominates the body-force field $f_x(x, y)$. The convective and diffusive term contribute only to a minor extent of the body force at this single phase position. Similar results were obtained with the V.E. method (not shown). Further details regarding the contribution of each term to the N.S.E. body force is provided by the respective integral value over the defined CV for all 24 phase positions. The results are shown in figure 5.13. The unsteady term (red data) represents the major contribution regardless of the phase position. On the other hand, convective (blue data) and diffusive (white data) terms contribute only to a minor extent to the integral value of the force. Such a behaviour was previously reported by Benard et al. [17] and Kuhnhenn et al. [29].

Comparison between the results obtained with N.S.E. and V.E. shows good agreement. Nonetheless, the N.S.E. seems to estimate a larger body-force magnitude when compared to the V.E. approach. In general, the main characteristics of each single phase position can be clearly identified on both methods. However, the first $\phi = 0$ and second $\phi = \pi/4$ phase positions exhibit a slightly different body-force distribution depending on the approach. Specifically, an oval-like positive net force, centred at $x \approx 1$ mm and $y \approx 0.5$ mm appears on the V.E. approach for the first position which is not consistent with the determined body-force field determined with the N.S.E. method, see figures 5.10(a) and 5.11(a). For the second phase position, both the positive and negative net force downstream the exposed electrode determined with the N.S.E. appear to have larger magnitude when compared to the V.E. body-force field, see figures 5.10(b) and 5.11(b). Similarly to the time-averaged V.E. body-force results, vertical stripes appear on the body-force distribution. Such a result is clearly not physical and it is attributed to the numerical error associated with the numerical operations to obtain higher-order derivatives of the velocity field and discretization domain [17].

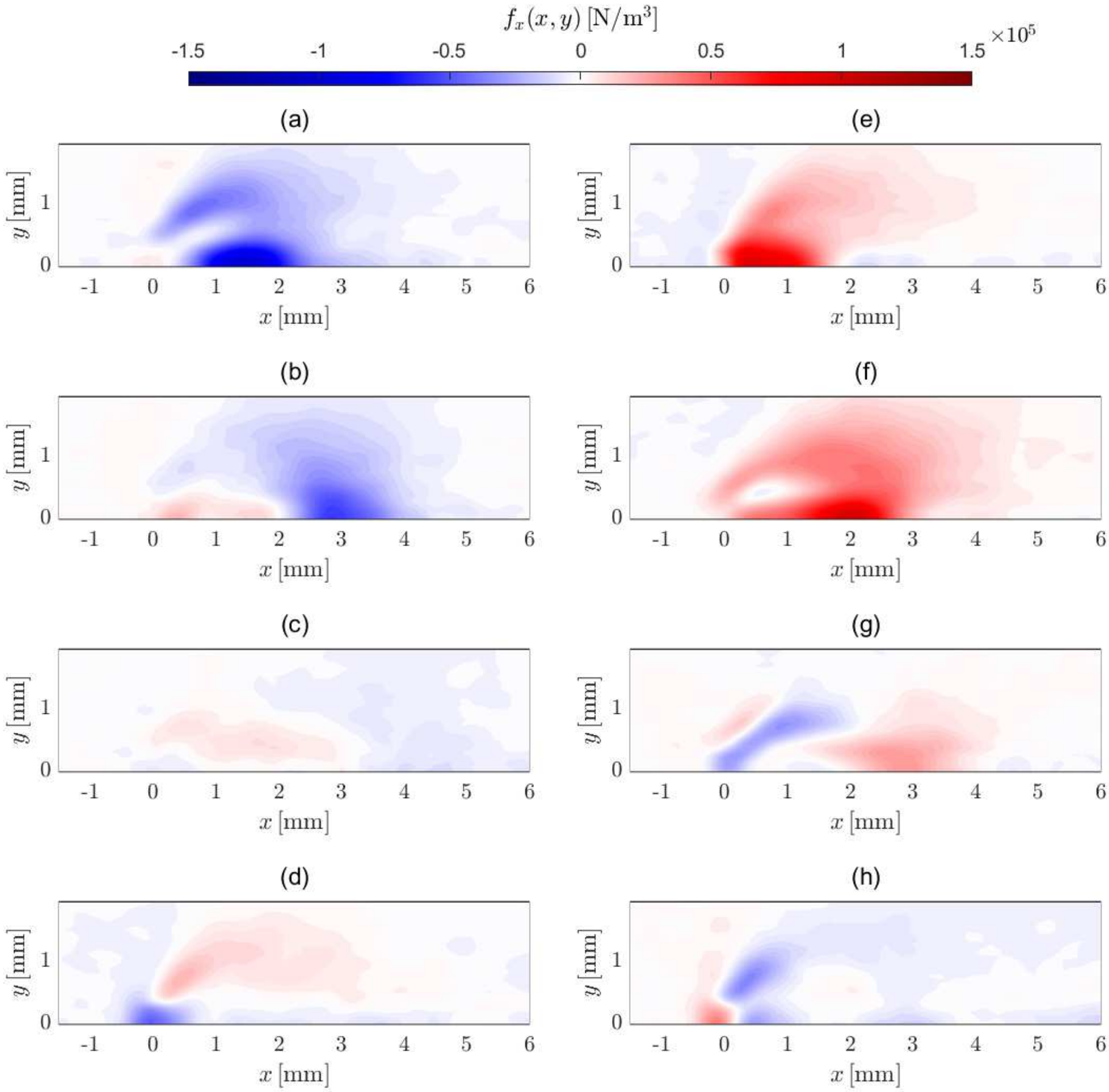

Figure 5.10: Phase-resolved body force fields along streamwise direction $f_x(x, y)$ in quiescent air $U_\infty = 0$ m/s determined according to N.S.E. (equation 3.2a). (a) $\phi = 0$; (b) $\phi = \pi/4$; (c) $\phi = \pi/2$; (d) $\phi = 3\pi/4$; (e) $\phi = \pi$; (f) $\phi = 5\pi/4$; (g) $\phi = 3\pi/2$; (h) $\phi = 7\pi/4$.

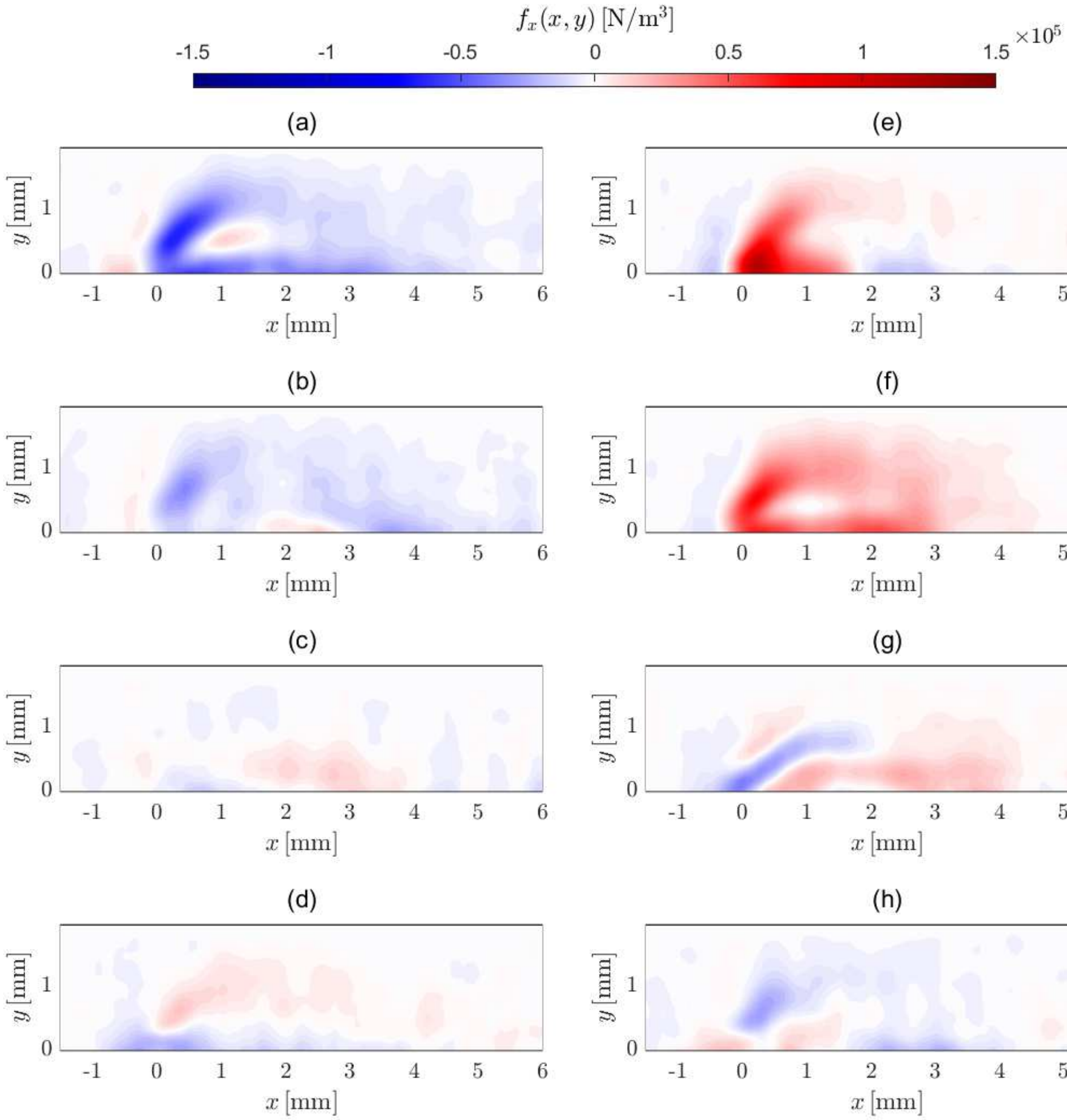

Figure 5.11: Phase-resolved body force fields along streamwise direction $f_x(x, y)$ in quiescent air $U_\infty = 0$ m/s determined according to V.E. (equation 3.6). (a) $\phi = 0$; (b) $\phi = \pi/4$; (c) $\phi = \pi/2$; (d) $\phi = 3\pi/4$; (e) $\phi = \pi$; (f) $\phi = 5\pi/4$; (g) $\phi = 3\pi/2$; (h) $\phi = 7\pi/4$.

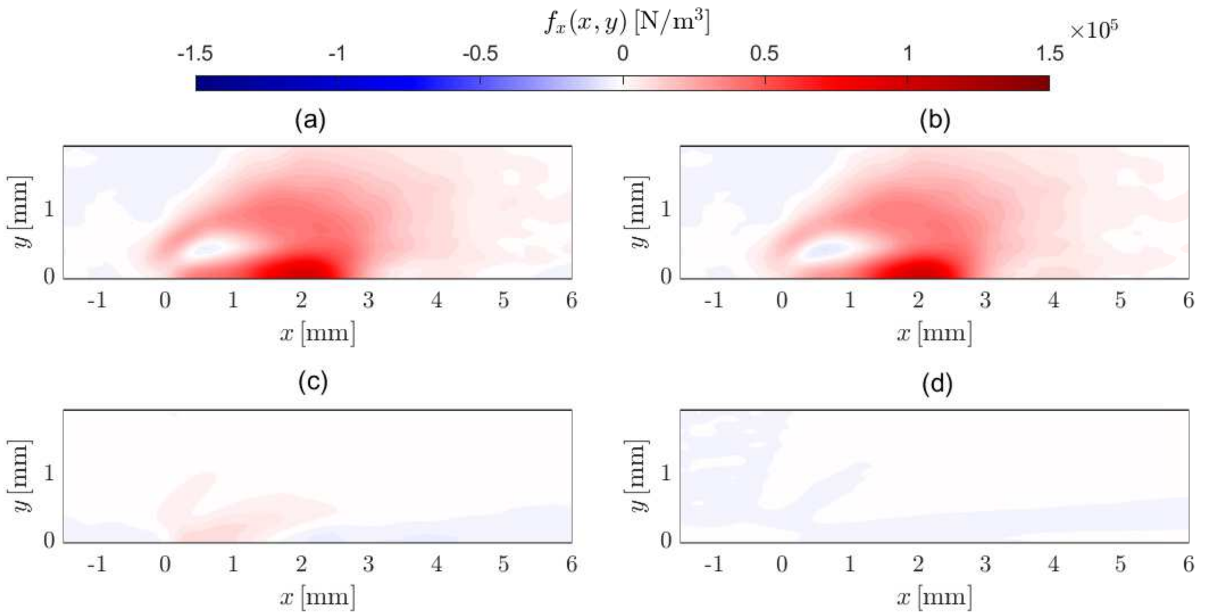

Figure 5.12: Contribution of the temporal, convective and diffusive terms to the phase-resolved spatial distribution of the body-force field $f_x(x, y)$ according to N.S.E. (equation 3.2a) at phase position $\phi = 5\pi/4$. (a) Phase-resolved body force $f_x(x, y)$; (b) temporal term: $\frac{\partial u}{\partial t}$; (c) convective term: $\rho u_j \frac{\partial u_i}{\partial x_J}$; diffusive term: $\mu \frac{\partial^2 u_i}{\partial x_j \partial x_j}$

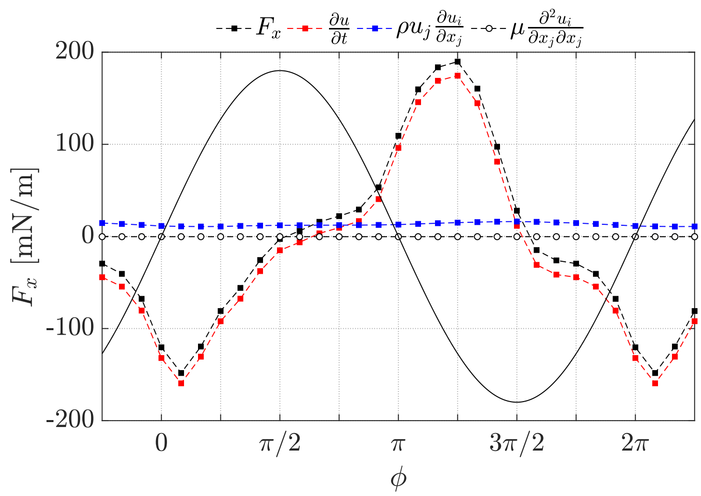

Figure 5.13: Phase-resolved integral values of the force F_x and source terms contribution during the discharge cycle determined according to N.S.E. (equation 3.2a): temporal $\frac{\partial u}{\partial t}$ (red data), convective $\rho u_j \frac{\partial u_i}{\partial x_j}$ (blue data) and diffusive $\mu \frac{\partial^2 u_i}{\partial x_j \partial x_j}$ (white data).

Analysis of the phase-resolved force production F_x is determined by integrating the plasma body-force over the CV, see section 5.2.1. Additionally, all 24 phases are taken into account to provide high resolution of the forcing mechanism. The results are shown in figure 5.14 for the N.S.E. (blue data) and V.E. (black data), the current signal is added to the graph in order to assess the regions of collapsed discharge (rectangles).

The results clearly resemble the oscillating character of the discharge [17, 23, 34]. Whilst the positive-going half cycle is responsible for producing a mainly negative net volume force, the negative-going half cycle generates a mainly positive net volume force. The negative force tends to increase as the positive-going half cycle evolves up to the first collapse point of a single discharge cycle $\phi = \pi/2$, which is consistent with the collapse of the current signal shown in figure 5.14. In the subsequent phase positions $\pi/2 \leq \phi \leq 5\pi/6$ which corresponds to the discharge collapsed region, the force F_x is virtually null. Nonetheless, a minimal increase on the estimated integral value is evidenced for both methods. Once the negative-going half cycle starts, the volume force increases significantly which then presents a decreasing behaviour. Once the second collapse region of the discharge is reached $\phi = 3\pi/2$, the force is found to be almost null, however in the subsequent phase positions $19\pi/12 \leq \phi \leq 11\pi/6$ a mild decrease mainly for N.S.E. method is determined. On the other hand, the V.E. method seems to correlate better with the expected behaviour during the collapsed discharge zones, i.e., the integrated value is expected to be identically null $F_x \approx 0$. In agreement with the body force fields shown on figures 5.10 (a)-(h) and 5.11 (a)-(h) for the N.S.E. and V.E., respectively, the volume-integrated force indicates a larger value when using the N.S.E. method. Furthermore, the maximum force value appears to be shifted by one phase position when comparing both methods and by $\pi/2$ when compared to the applied waveform.

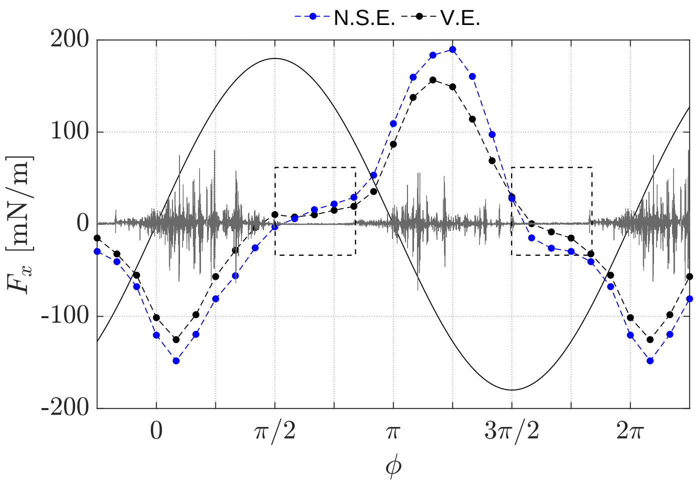

Figure 5.14: Integrated value of the phase-resolved streamwise body-force field F_x according to CV $x = [-1.5; 6]$ mm $y = [0; 2]$ mm using the N.S.E. method (blue data) and V.E. method (black data) for quiescent air $U_\infty = 0$ m/s; the current signal is represented in grey to assess the discharge collapsed region (dashed line box).

The impact of external flow on the phase-resolved body force is studied for the N.S.E. (3.2a) and V.E. (3.6). In order to guarantee and ease comparisons only 4 out of 24 phases positions are selected. Accordingly, the results are shown for the minimum ($\phi = \pi/12$), maximum ($\phi = 5\pi/4$) and two additional phase positions ($\phi = \pi/3$; $\phi = 17\pi/12$), see section 4.1.4 figure 4.7(b). The body-force distribution is presented for free-stream velocities $U_\infty = [2.5, 7.5, 20]$ m/s. The results for the remaining free-stream velocities $U_\infty = [5, 10, 15]$ m/s are presented in appendix B. Furthermore, for comparison reasons the quiescent air body-force field is also shown. The results for the N.S.E. for increasing free-stream velocity are shown on figures 5.15 (a)-(h) and on figures 5.16 (a)-(h) for the positive and negative-going half cycle, respectively. The comparison of source terms distributions is not included, however it was verified that the temporal term still dominates the volume-force generation whereas the convective and diffusive terms contribute only to a minor extent of the force field, further analysis is provided in section 6.1. Regarding the positive-going half cycle, the results evidence a good correlation between quiescent air and $U_\infty = 2.5$ m/s (fig. 5.15)(a)-(e); fig. 5.15)(b)-(f)). The volume force main characteristics appear to be preserved. For increasing free-stream velocity, the body-force field starts to reveal a slight impact of the external airflow. The direct comparison between quiescent air and $U_\infty = 20$ m/s indicates that the region where the body-force magnitude is larger $x = 2$ mm becomes smaller in height (fig. 5.15)(a)-(e); fig. 5.15 (d)-(h)). Nonetheless, all the main features of the body-force field in quiescent-air conditions can be clearly identified for the considered free-stream velocities. For instance, the positive volume-force generation immediately downstream the exposed electrode and the higher magnitude region (fig. 5.15)(a)-(d)). Similarly, for the negative-going half cycle the body-force fields show good agreement between quiescent-air conditions and $U_\infty = 2.5$ m/s (fig. 5.16) (a)-(e); fig. 5.16)(b)-(f)). For increasing free-stream velocity, the results indicate an impact of the external flow on the body-force field. Specifically, an oval-like shape centred at $x \approx 0.5$ mm and $y \approx 0.2$ mm becomes more pronounced (fig. 5.16(a)-(d)). In addition, the area of larger positive net force becomes weaker, see, for instance, the body-force field distributions at $x \approx 2.5$ mm and $y \approx 0.1$ mm in figures 5.16(e)-(h). However, the global features remain unchanged.

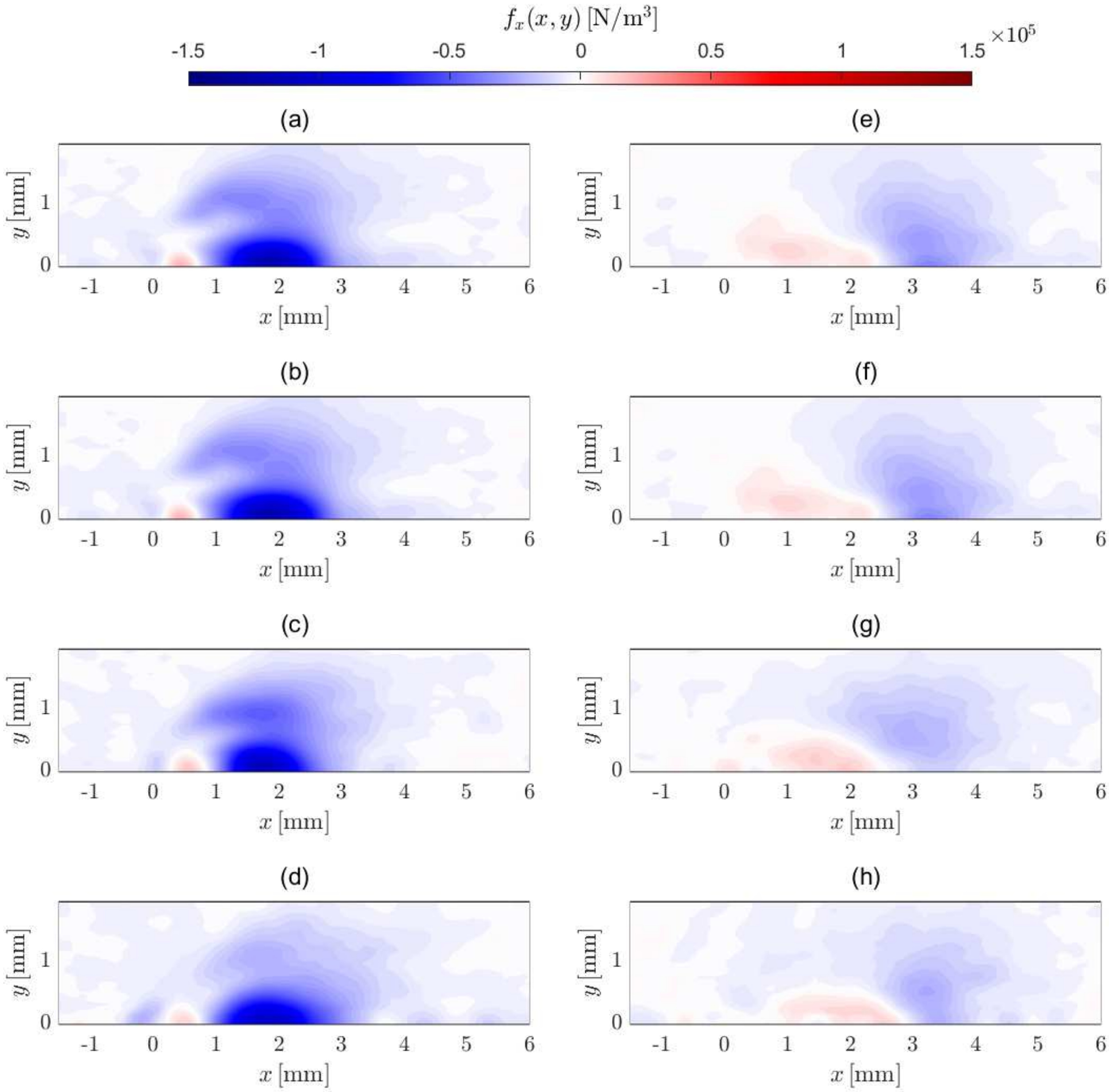

Figure 5.15: Phase-resolved body-force field distribution on the positive-going half cycle for increasing free-stream velocity $U_\infty = [0, 2.5, 7.5, 20]$ m/s determined according to N.S.E. (equation 3.2a). (a)-(d) $\phi = \pi/12$; (e)-(h) $\phi = \pi/3$.

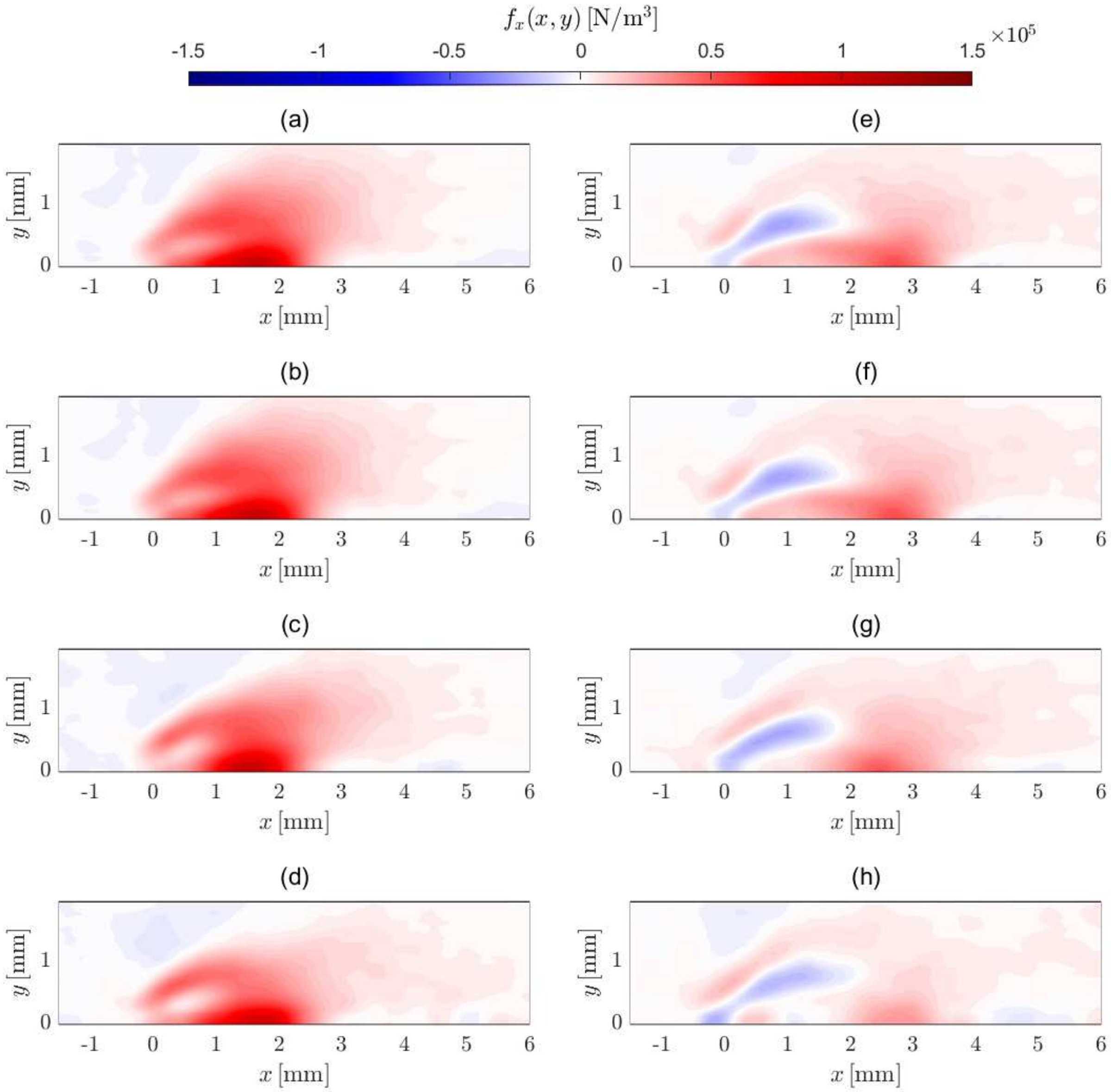

Figure 5.16: Phase-resolved body-force field distribution on the negative-going half cycle for increasing free-stream velocity $U_\infty = [0, 2.5, 7.5, 20]$ m/s determined according to N.S.E. (equation 3.2a). (a)-(d) $\phi = 5\pi/4$; (e)-(h) $\phi = 17\pi/12$.

The V.E. phase-resolved body-force field results are shown in figures 5.17 (a)-(h) and 5.18 (a)-(h) for the positive and negative-going half cycle, respectively. The V.E. body-force fields during the positive-going half cycle indicate a mild degradation of the spatial distribution in the presence of external flow. Such an effect is already visible for $U_\infty = 2.5$ m/s when compared with quiescent-air conditions (fig. 5.17(a)-(b); fig. 5.17(e)-(f)). With increasing airflow velocity, it gradually becomes more noticeable. For free-stream velocities up to $U_\infty = 7.5$ m/s, the dominant characteristics can be identified, however when comparing to $U_\infty = 20$ m/s the impact appears to be strongly pronounced (fig. 5.17(a) and fig. 5.17(d)). On the other hand, the negative-going half cycle seems to be less sensitive. The results shown in figures fig. 5.18(a)-(d) depict only a slight change as the free-stream velocity is increased. The area of the dominant force seems to be slightly diminished in height when comparing quiescent air and $U_\infty = 20$ m/s. In addition, an oval-like shape appears in the middle of the dominant region of the positive volume-force generation when operating with external flow (fig. 5.18(a)-(d)). Nonetheless, considering only the cases in the presence of external flow, both the body-force field magnitude and spatial distribution seem to correlate well. For instance, comparison between free-stream velocities $U_\infty = 2.5$ m/s and $U_\infty = 20$ m/s evidences that although minor changes can be detected, the overall behaviour remains unchanged (fig.5.18(a)-(e); fig. 5.18(d)-(f)). Furthermore, the impact of the stripes due to numeric operations seem to significantly deform the body-force field as free-stream velocity is increased when compared to quiescent air.

The comparison between both methods, in general indicates that the most significant features of the phase-resolved body-force field can be identified regardless of the method for the negative-going half cycle. For instance, both approaches seem to indicate an increasing oval-like shape at phase position $\phi = 5\pi/4$ in the dominant region of the body-force field, which gradually becomes more pronounced as external velocity is increased. Additionally, the finger-like shape which relates to a negative volume force generation is present in both methods. On the other hand, the positive-going half cycle results indicates a divergent trend between both approaches. Whilst the N.S.E. body-force field global features can be identified for the considered free-stream velocities, the V.E. method appears to more sensitive. In addition, the determined body-force field distribution is considerably different when comparing the N.S.E. and V.E. methods.

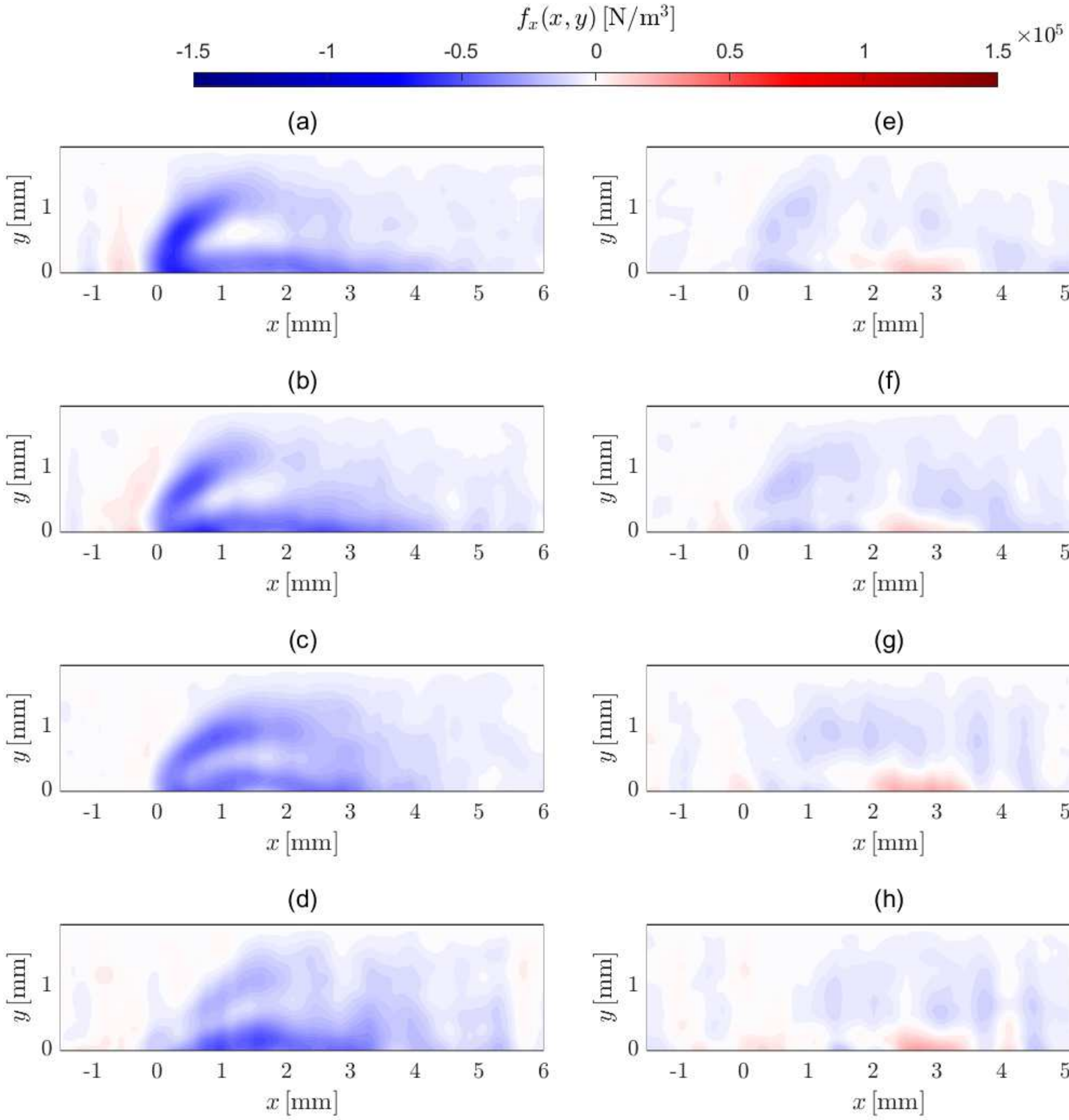

Figure 5.17: Phase-resolved body-force field distribution on the positive-going half cycle for increasing free-stream velocity $U_\infty = [0, 2.5, 7.5, 20]$ m/s determined according to V.E. (equation 3.6). (a)-(d) $\phi = \pi/12$; (e)-(h) $\phi = \pi/3$.

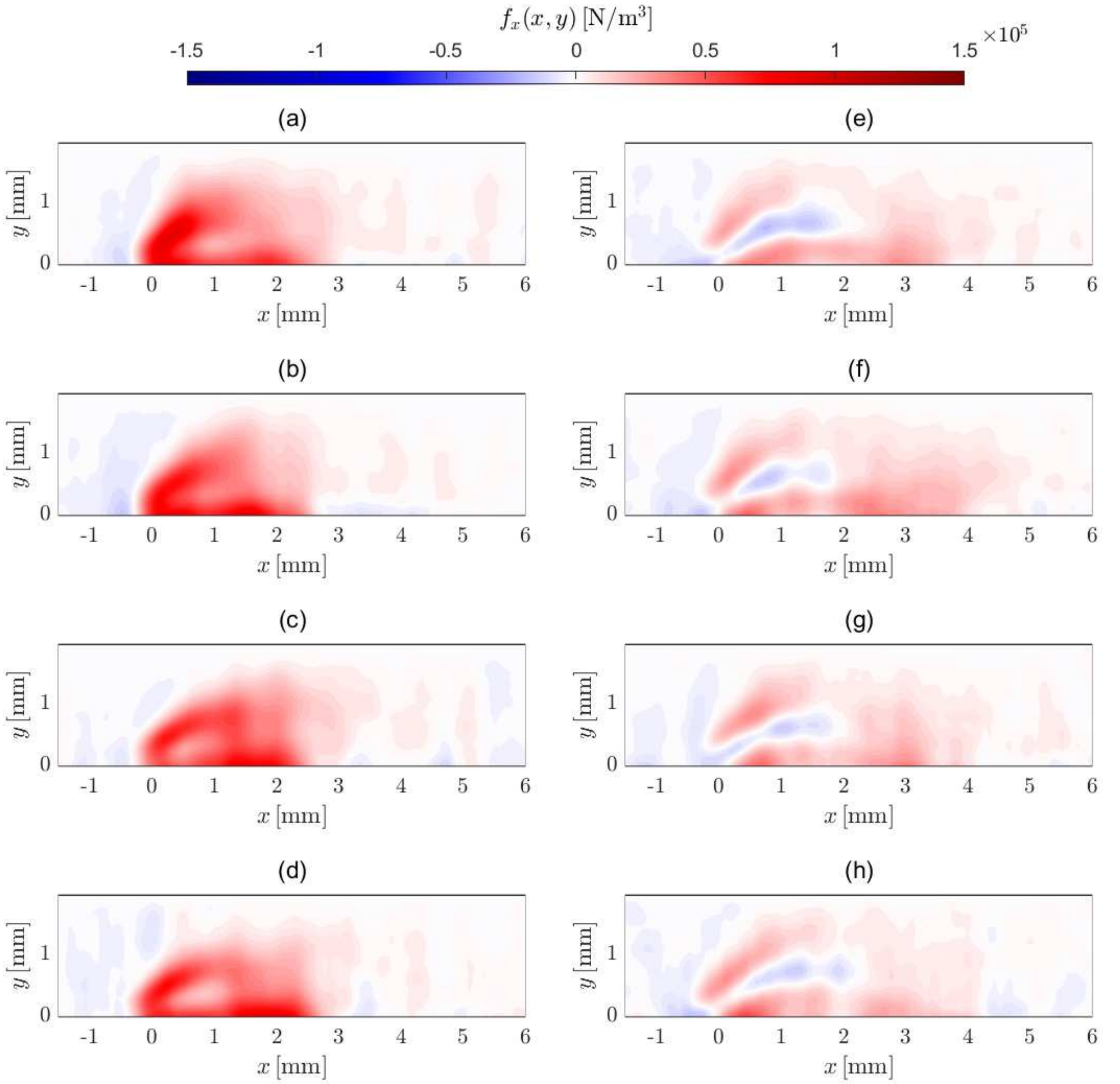

Figure 5.18: Phase-resolved body-force field distribution on the negative-going half cycle for increasing free-stream velocity $U_\infty = [0, 2.5, 7.5, 20]$ m/s determined according to V.E. (equation 3.6). (a)-(d) $\phi = 5\pi/4$; (e)-(h) $\phi = 17\pi12$.

Further analysis of the phase-resolved results is provided by the integrated value of body-force fields over the CV. The results are shown for all tested free-stream velocities in figures 5.19(a) and 5.19(b) for the N.S.E. and V.E. method, respectively. Analysis of the N.S.E. integral value indicates that, on one hand the positive-going half cycle seems to be influenced only for higher free-stream velocities $U_\infty = [15; 20]$ m/s. For the lower cases, the force magnitude is found to be virtually constant when comparing with quiescent-air conditions. On the other hand, during the negative-going half cycle a slight decrease is evidenced for free-stream velocities up to $U_\infty = 10$ m/s, whilst for higher external airflow velocities a steep drop is evidenced $\approx 38\%$, $U_\infty = [15; 20]$ m/s. Regarding the V.E. method, the results shown in figure 5.19(b), the positive-going half-cycle net force value appears to be gradually diminished in magnitude as external-airflow velocity is increased. Such a result is clearly visible at the minimum force location $\phi = \pi/12$. For the negative-going half-cycle, the results seem to correlate better with quiescent-air conditions which correlates with the analysis of the phase-resolved body-force fields. In addition, the results lie within a range of 25% and 10% for the positive and negative-going half-cycle, respectively.

Furthermore, the collapsed discharge regions are also evaluated in figures 5.19(a) and 5.19(b) by the no-current zones (rectangles). In the first collapsed region, both N.S.E. and V.E. methods indicate a virtually null net-force production F_x. Such a conclusion appears to be more trustful when considering the V.E. method. In addition, the domain is found to be independent of the operating free-stream velocity, see also 5.1.2. In contrast, the estimated integral value of the body-force features negative values during the second collapse of the discharge. However, the V.E. seems to estimate a slightly lower force integral value when compared with the N.S.E. approach. Furthermore, the V.E. method appears to be only slightly dependent on external flow, whereas the N.S.E. seems to indicate a gradually decreasing force integral value for increasing free-stream velocity.

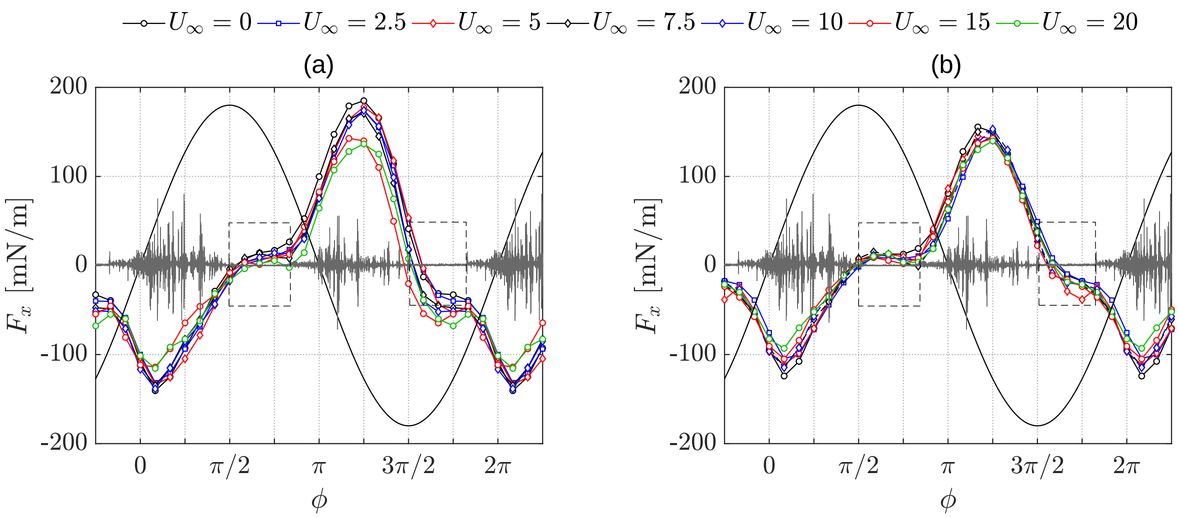

Figure 5.19: Integrated value of the phase-resolved streamwise body-force field F_x according to the CV $x = [-1.5; 6]$ mm $y = [0; 2]$ mm for the tested free-stream velocities U_∞ m/s and current signal; discharge collapse regions indicate by the rectangles. (a) according to N.S.E. (equation 3.2a); (b) according to V.E. (equation 3.6).

Chapter 6

Discussion

In this chapter discussion of the results is presented, including the contribution of each source term to the body-force determination, role of the assumptions, impact of phase resolution, fluid-mechanic efficiency and effectiveness. The reproducibility of the results, plasma actuator assembly and degradation are elaborated.

6.1 Contribution of each source term

In order to explain the behaviour of the phase-resolved integral forces, the contribution of the temporal (first row), convective (second row) and diffusive terms (third row) to the phase-resolved volume-integrated force F_x shown in figure 5.19 is presented in figures 6.1(a)-(f). The left and right column correspond to the N.S.E. and V.E. method, respectively. For simplicity, the results are only presented for free-stream velocities $U_\infty = [0, 5, 10, 20]$ m/s. One should notice that the time-averaged value of the presented quantities can be obtained by averaging the values for a single discharge cycle. In addition, the average value over a cycle of the unsteady component is found to be almost identical to zero $\mathcal{O}(10^{-18})$ [17]. The results immediately show the difference in order of magnitude between each component. As indicated by the source terms analysis (see figures 5.12 and 5.13), the unsteady term represents the major contribution to the phase-resolved body force whereas the convective and diffusive term correspond only to a minor part. Specifically, the results indicate that from the convective to temporal terms the values are one order of magnitude larger. Similarly, from the convective to diffusive terms the values are an order of magnitude smaller.

The results indicate that the difference between the N.S.E. and V.E. based force estimation arises from the convective terms (fig. 6.1(b); fig. 6.1(e)). Whilst the V.E. method convective terms reveal only minor changes when compared to the quiescent-air case, the N.S.E. method indicates a significant variation. Such an effect appears to be gradually enhanced as the external-airflow velocity increases. Nonetheless, the progression for the different phase positions appears to be similar for both methods. Moreover, the order of magnitude is found to be the same as the estimated time-averaged volume-integrated force, see figure 5.9. Such a result correlates with the quasi-steady behaviour $\partial u/\partial t \approx 0$ and a considerable small impact of the diffusive terms [17, 28].

Regarding the diffusive terms, the results indicate a considerably different behaviour between both approaches (fig. 6.1(c); fig. 6.1(f)). On one hand, the magnitude of the volume-integrated values of the diffusive terms determined with the V.E. (3.6) increase with external-airflow velocity. This is due to the BL operation where the viscous effects are expected to increase with free-stream velocity [54, 55]. On the other hand, the N.S.E. method indicates a minor decrease in magnitude for higher free-stream velocities. As a result of the subtraction of the base-flow pressure gradient, the values shown in figure 6.1(c) represent the difference between the actuated and non-actuated BL diffusive terms, see section 4.3.3. For increasing airflow velocity the plasma is expected to gradually loose the ability to modify the BL [9]. Hence, the magnitude from quiescent-air conditions to free-stream velocity $U_\infty = 20$ m/s decreases.

As an aspect of major importance, the volume integrated value of the unsteady term determined with the V.E. and N.S.E. appears to be virtually constant for free-stream velocities up to $U_\infty = 10$ m/s for both methods (fig. 6.1(a); fig. 6.1(b)). For higher free-stream velocity $U_\infty = 20$ m/s, the results indicate a minor change in both negative and positive force peak. However, such an effect appears to be more pronounced when determined with the N.S.E. than with the V.E. method.

In conclusion, the independence of the temporal component from external flow for free-stream velocities up $U_\infty = 10$ m/s indicates that the integral-force determination can be reduced to a quiescent-air analysis. Such an approach would apply for the V.E. method where the convective terms undergo minor changes. Consequently, a time-averaged analysis of the velocity field would be sufficient to study the influence of external flow on the DBD plasma net force for free-stream velocities up to $U_\infty = 10$ m/s. However, it is mandatory to investigate the phase-resolved body-force fields as the distributions exhibit slight to mild changes when operating in the presence of external airflow, see section 5.2.2. Furthermore, one should notice that the plasma was operated within a boundary-layer where the velocity is found to be lower than the operating free-stream velocity (sec. 4.3.2 table 4.5).

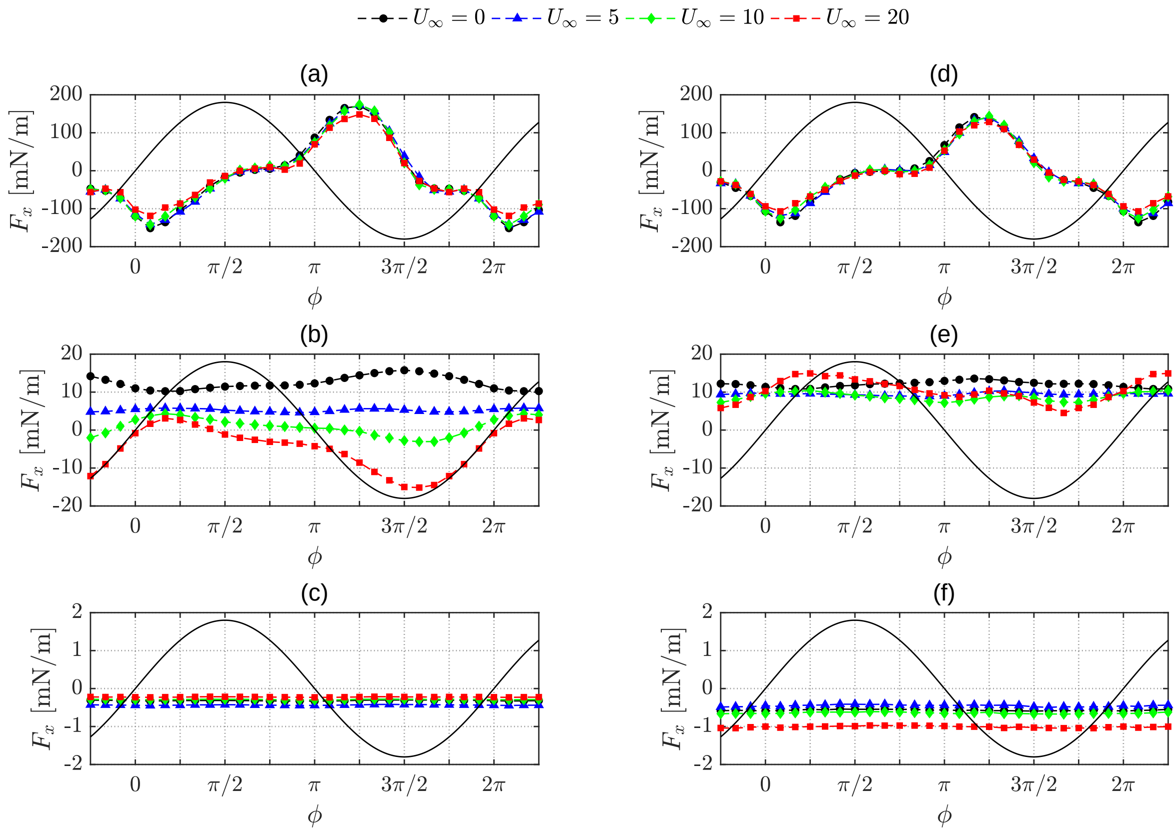

Figure 6.1: Phase-resolved integral value of the source-terms contribution to the net force determined according to N.S.E. (equation 3.2a) (a)-(c) and V.E. (equation 3.6) (d)-(f). (a)-(d) temporal terms; (b)-(e) convective terms; (c)-(f) diffusive terms.

6.2 Role of the unknown pressure gradient

The extensive experimental study on the time-averaged and phase-resolved body-force fields shed light into the validity of the N.S.E. and V.E. methods, see sections 3.1, 5.2.1 and 5.2.2. The results for quiescent-air conditions for the time-averaged body-force indicates that both methods lead to trustful results. For instance, this is evidenced by the compliance between the body-force magnitude and spatial distribution determined with both methods, see figures 5.3(a)-(b). In addition, the ratio of the force gradients $\partial f_y/\partial x$ and $\partial f_x/\partial y$ shown in figure 5.6 is a good indicator of the validity of the V.E. assumption. On the other hand, the phase-resolved analysis indicates a slightly different body-force estimation between both approaches. The spatial distribution was found to be mildly changed and the N.S.E. integral value seems to estimate a larger net force, see section 5.2.2. Nonetheless, it seems to be reasonable to assume that both methods are valid for quiescent-air conditions.

In the presence of external airflow, the time-averaged results show a distinctive behaviour between both methods, see figures 5.7(a)-(c) and 5.8(a)-(c). With the N.S.E. method, the body-force field dominant region of positive net force is diminished in height and length already for $U_\infty = 5$ m/s. In addition, a negative volume force on top of the bulk of the plasma gradually grows as external-airflow velocity is increased. In contrast, the body-force fields determined with the V.E. approach show robust results for free-stream velocities up to $U_\infty = 10$ m/s (fig.5.3(b); fig.5.8(a)-(b)). The net-force analysis of the body-force indicates a virtually constant net force determined with the V.E. method when operating with external flow, whereas the N.S.E. shows a decisively decreasing behaviour even reaching negative values, see figure 5.9. Regarding the phase-resolved body-force fields, an evaluation of the impact of external flow on the force is complex. On one hand, the temporal terms appear to be independent of external flow for free-stream velocities up to $U_\infty = 10$ m/s for both methods. On the other hand, the convective shows a minor change for the V.E. whilst a significant variation is found for the N.S.E. method, see figures 6.1(a)-(f).

Correlation with the power consumption anticipates a constant net-force output for the virtually constant power-consumption results, see section 5.1.1 [8, 16]. On one hand, the integrated volume-force determined with the V.E. resembles such a behaviour, on the other hand the results obtained with the N.S.E. indicate that the negligible pressure gradient assumption is an oversimplification. The issues regarding the presence of a pressure gradient make comparisons between the force gradients difficult and doubtful, therefore it is not performed, see for instance figure 5.6. Moreover and since it is assumed that the base-flow adverse pressure gradient remains unchanged with and without plasma actuation, the varying results for different free-stream velocities obtained with the N.S.E. method are attributed to the plasma-induced pressure gradient, see sections 4.3.2 and 4.3.3, hence it implies an oversimplification of the method. It should be noted that the questionable results determined with the N.S.E. (3.2a) might also be related to the actuator location and assembly. The proximity to the flat plate leading edge where the external airflow is decelerating, and the non-negligible thickness of the actuator might lead to local streamline curvature. Although, the impact is expected to be small, this effect might influence the force determination with the N.S.E. method. For V.E. method, as the pressure gradient is present implicitly in the equations, this effect is not evidenced in the results. Further analysis regarding the plasma-actuator assembly is provided in section 6.6.

6.3 Influence of phase resolution on the volume-integrated force

The discharge phenomenon of an AC-DBD plasma actuator is well-known for the highly unstable character which develops in small time scale [13, 14, 23]. Such a behaviour can be clearly verified by the phase-resolved body-force field analysis provided in section 5.2.2. The combined impact of the unsteadiness and short time scale is expected to have a large influence on the estimation of the time derivative of the velocity $\partial u/\partial t$. In addition, since the unsteady term is determined with a central difference scheme, it might be slightly dependent on the magnitude in the neighbouring phase positions. Accordingly, a study based on the discharge-cycle resolution is performed in order to evaluate the impact of the phase-to-phase spacing ($\Delta\phi$). The phase-resolved and time-averaged integral value are determined for different spacing ($\Delta\phi = \pi/3$ (black data), $\Delta\phi = \pi/4$ (blue data), $\Delta\phi = \pi/6$ (red data), $\Delta\phi = \pi/12$ (green data)) within the defined CV, see section 5.2.1. For simplicity, the analysis is only provided for the N.S.E. method in quiescent-air conditions, see section 3.1. In figure 6.2(a) and 6.2(b) the results are shown for the phase-resolved and time-averaged force integral, respectively, for phase resolutions of 6, 8, 12 and 24 phases per discharge cycle.

In general, the results shown in figure 6.2(a) for all considered discharge-cycle discretization strategies are able to describe the oscillating behaviour of the phase-resolved body-force production. However, resolution lower than $\Delta\phi = \pi/6$ (12 phase positions) culminates in a wrong estimation of the peak of the force production either on the positive- or on the negative-going half cycle. Nonetheless, for a 8 phases decomposition, although the force peak is slightly shifted the results resemble approximately the force production determined with 12 phase positions. Furthermore, comparison between 12 and 24 phase resolutions evidences that the positive force peak is estimated at the correct position, however the negative peak is rather unclear. As an aspect of major importance, it should be noticed the unsteady term of equations (3.2a) and (3.6) is highly sensible to the defined Δt.

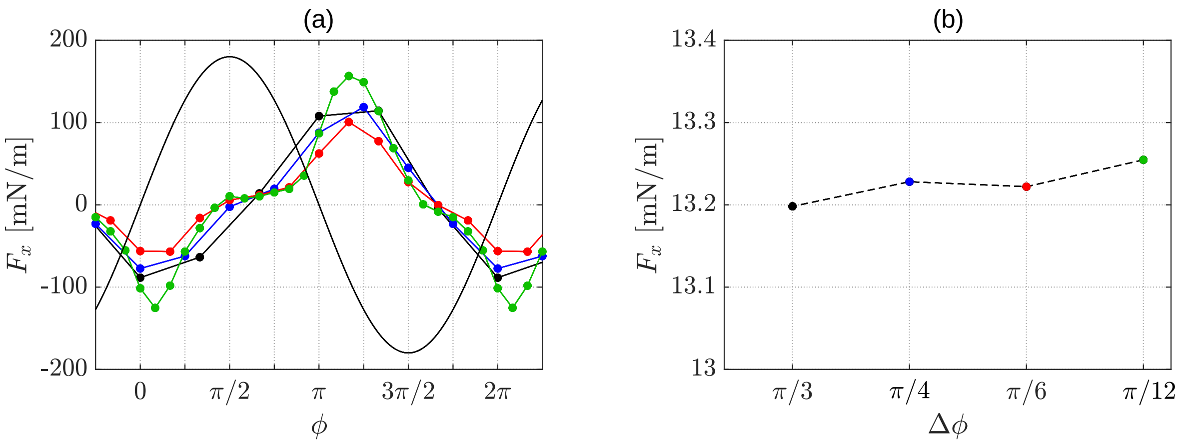

Figure 6.2: Impact of the discharge cycle discretization $\Delta\phi$ on the body force determination in quiescent air $U_\infty = 0$ m/s according to N.S.E. (equation 3.2a): $\Delta\phi = \pi/3$ (black data), $\Delta\phi = \pi/4$ (blue data), $\Delta\phi = \pi/6$ (red data), $\Delta\phi = \pi/12$ (green data). (a) Phase-resolved body-force production for a single discharge cycle; (b) Time-averaged volume integrated force.

The time-averaged force production sensitivity to the discharge discretization is studied on figure 6.2(b). One should notice that the time-averaged results are computed by averaging the phase-resolved velocity fields and subsequently calculating the body-force field (see section 3.1 and 4.1.4). The results estimate an insignificant impact of the phase-to-phase spacing on the force determination. A variation of $\Delta F_x \leq 1\%$ is determined between the lower and higher phase resolutions. Such a results comes without surprise a the source of measurement error is the unsteady term which has a meaningless contribution to the time-averaged body force [17].

A complementary study on the discharge-cycle discretization is performed by considering different initial phase positions to estimate the phase-resolved body-force production. Accordingly, the phase-resolved force integral value F_x is determined for phase resolutions of 8 and 12 phases and subsequently compared with phase resolution of 24 phases per discharge cycle (red data). The starting phase position is shifted and comprises $\phi_0 = [0, \pi/12, \pi/6]$ (black, blue and green data, respectively) for the 8 phase resolution and $\phi_0 = [0, \pi/12]$ (black and blue data, respectively) for 12 phase resolution. The results are only considered for quiescent-air conditions using the N.S.E. (3.2a). In figures 6.3(a) and 6.3(b), the integral value of the phase-resolved body force is shown for phase resolutions of 8 and 12 phases for the different starting phase position, respectively.

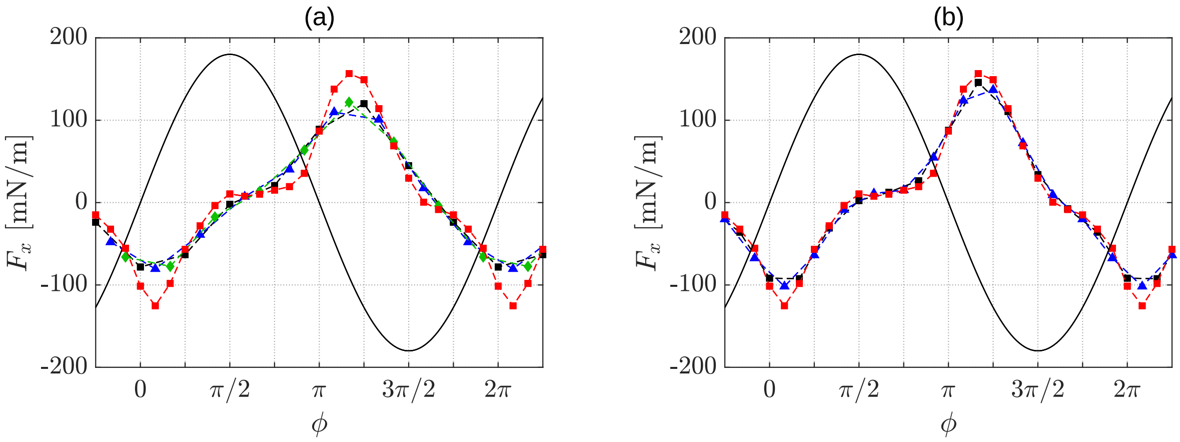

Figure 6.3: Impact of the discharge cycle discretization and starting phase position on the volume-integrated phase-resolved body force; ($\Delta\phi = \pi/12$ - red data). (a) $\Delta\phi = \pi/4$: $\phi_0 = 0$ (black data), $\phi_0 = \pi/12$ (blue data), $\phi_0 = \pi/6$ (green data); (b) $\Delta\phi = \pi/6$: $\phi_0 = 0$ (black data), $\phi_0 = \pi/12$ (blue data).

Regarding the 8 phases per discharge cycle, the results indicate the force negative peak magnitude to be similar for the different starting phase positions. On the other hand, the positive force peak seems to be better estimated when starting at phase position $\phi = \pi/6$ (green data). Furthermore, the peak locations either on the positive and negative-going cycle is not accurately estimated with a single strategy when compared with phase resolution of 24 phases (red data). Whilst in the positive-going half cycle the estimation seems to be more accurate for starting phase position $\phi = \pi/12$ (blue data), in the negative-going half cycle the peak is coincident with the the force peak according to a phase resolution of 24 phases, for starting phase position $\phi = \pi/6$. Furthermore, in the regions of collapsed discharge, 8 phase positions per discharge cycle appear not to be able to resolve the phenomenon regardless of the starting phase position.

For the 12 phases per discharge cycle shown in figure 6.3(b) for starting phase positions $\phi_0 = [0, \pi/12]$ (black and blue data, respectively), both strategies seems be capable of characterizing the collapsed discharge region accurately when compared to the 24 phases per discharge cycle (red data). Nonetheless, the peak locations are again sensitive to the starting phase position. Accordingly, depending on the strategy, one can only determined the peak location accurately. Nonetheless, the magnitude seems to be always underestimated when compared to a phase resolution of 24 phases.

6.4 Fluid mechanic efficiency and effectiveness

The fluid-mechanic efficiency η_{FM} (2.4) and effectiveness η^*_{FM} (2.5) of the present plasma actuator configuration are studied [25, 45, 46], see also section 2.4.1. Due to the anticipated impact of the pressure gradient on the body-force field estimation with the N.S.E. (3.2a), the results are only considered for the V.E. (3.6). The considered integral value of the time-averaged force F_x and power consumption P can be evaluated in figures 5.9 and 5.1(a), respectively

The results indicate an increasing fluid-mechanic efficiency for the tested free-stream velocities, see figure 6.4(a). Such a result can be anticipated as the results of the integrated volume force F_x presents mild changes for a virtually constant power consumption P for increasing free-stream velocity, see sections 5.1.1 and 5.2.1. Even though the trend shows an increasing behaviour which favours the efficiency of DBD plasma actuators, one should notice that the power consumption is expected to drop significantly for higher free-stream velocities $\Delta P \approx 30\%$ for $M = 0.4$ [30], hence the results cannot be extrapolated for higher free-stream velocities. Furthermore, once the the external-airflow velocity is comparable to the drift velocity of the ions, an impact on the performance, thus a change on the plasma forcing mechanism might be expected. Regarding the fluid-mechanic effectiveness shown in figure 6.4(b), the relation between the integrated volume-force obtained from the V.E. (3.6) and the virtually constant power consumption translates into a small variation of the effectiveness when operating under the influence of external airflow. However, a steep drop is evidenced between quiescent air conditions and free-stream velocity $U_\infty = 2.5$ m/s. With increasing free-stream velocity, the effectiveness is found to be within a range of $\approx 7\%$. Moreover, the relation between the fluid-mechanic effectiveness and operating free-stream velocity, immediately anticipates the increasing behaviour of the fluid-mechanic power i.e. the mechanical power transferred by the plasma actuator to the fluid. At this point, a clear distinction between fluid-mechanic efficiency and effectiveness must be made. Whilst the effectiveness represents the electrical-to-mechanical conversion capability of the actuator, the efficiency provides insights about the actuator flow-control authority.

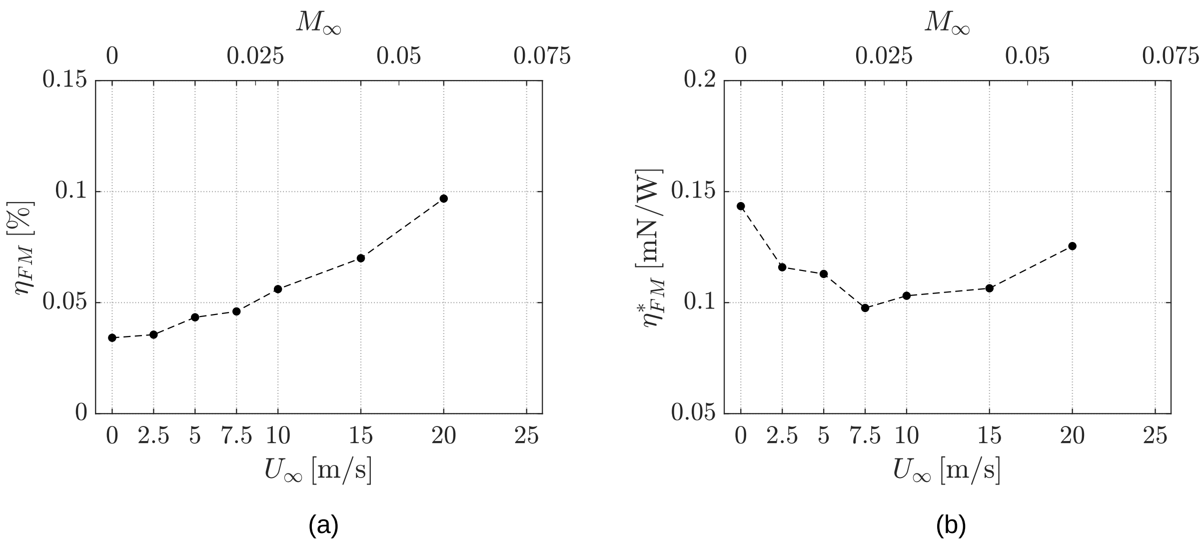

Figure 6.4: (a) Fluid-mechanic efficiency η_{FM} (%); (b) fluid-mechanic effectiveness η^*_{FM} (mN/W) of the present plasma actuator configuration as function of the operating free-stream velocity U_∞ m/s.

6.5 Results reproducibility

Analysis of the reproducibility of the body-force field results presented in the present study is shown on figure 6.5. The time-averaged force production is compared for the N.S.E. (3.2a) (blue data) and V.E. (3.6) (black data). The squares and circles indicate the data of the first and second set of experiments with phase resolutions of 8 and 24 phases per cycle, respectively (see section 4.1.5). In addition, the averaged of the resultant forces F_x is calculated and error bars are included to ensure statistical significance.

In general, the results indicate the same trend in both experiments. Even though the N.S.E. determines a non-physical negative force production for high free-stream velocities, the results are consistent in both experiments. Similarly, the trend associated to the V.E. method reveals consistent results between experiments. One might argue that the scatter is rather large for some free-stream velocities. However, being able to reproduce the trend is already a important indicator of the accurate measurements of the body-force production F_x. The range in which the results are comprised is dependent of the plasma actuator assembly and PIV calibration. On one hand, the PIV setup calibration was carefully performed in order to ensure the same resolution and FOV between experiments, see section 4.1.4. On the other hand, two actuators were handmade with the same characteristics for the two sets of experiments. Hence, the actuators might induce slightly different measurements depending on the experiment. Furthermore, it should be noticed that the reproducibility not only verifies the accuracy of the measurements but also indicates that two different plasma actuators operating in the same conditions are able to produce similar body force. Consequently, the reproducibility of the body-force results justifies a solid interpretation of the results on the force distributions and magnitude

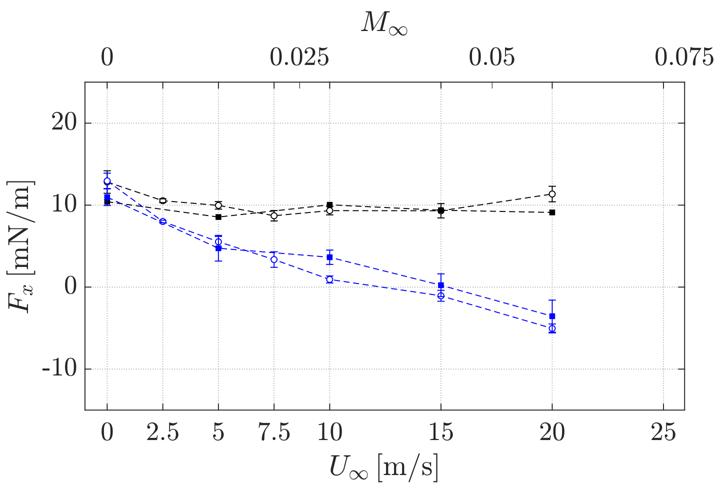

Figure 6.5: Reproducibility of the body-force results determined according to N.S.E. (equation 3.2a) (blue data) and V.E. (equation 3.6) (black data); solid squares represent the first set of experiments and empty circles the second.

6.6 Plasma actuator assembly and degradation

The impact of the geometrical dimensions of a plasma actuator when measuring the velocity field using the PIV technique can be somehow overlooked. For instance, in the present study the plasma actuator was built with total thickness of ≈ 0.5 mm which is considerably small. However, the FOV defined for the velocity measurements is given by the area 10×4.5 mm^2 (length$\times$height), hence the thickness represents about 11% of the total height. Although one might argue that such a percentage is meaningless, the actuator will be responsible for introducing several forward and backward-facing steps. Accordingly, it might influence the airflow over the flat plate. Ideally the actuator should be place on the flat plate without inducing any curvature on the flow. In the present study, the assembly was performed in order to guarantee smoothness and minimize the impact of a small step due to the actuator. Nonetheless, it represents a source of uncertainty to the velocity measurements. In figure 6.6(a) the current plasma actuator placed over the flat plate is shown to provide some insight about the configuration and indicate possible improvements for future experiments. A possible solution would be to flush-mount the actuator in a trough on the flat plate, thus avoiding the impact of the thickness of the electrodes and dielectric layers.

Another factor of major concern is the operation of a degraded plasma actuator. The generation of plasma above the dielectric leads to gradual degradation of the first layers. Consequently, the discharge properties are expected to change. As dielectric layers are destroyed the amount of current that passes through the dielectric increases. The power consumption and force production varies accordingly, hence resulting in different measurements. In the present study, the actuators were carefully analysed between measurements to verify and guarantee that the physical-geometrical properties remained unchanged. Nonetheless, it should be mentioned as a factor of major importance for future experiments. The visual inspection of the plasma actuator after long-time operation, as shown in figure 6.6(b), demonstrates the strong degradation of the dielectric layers. Immediately downstream the far most edge of the exposed electrode the top layer of Kapton destroyed and thus might comprise the experiments.

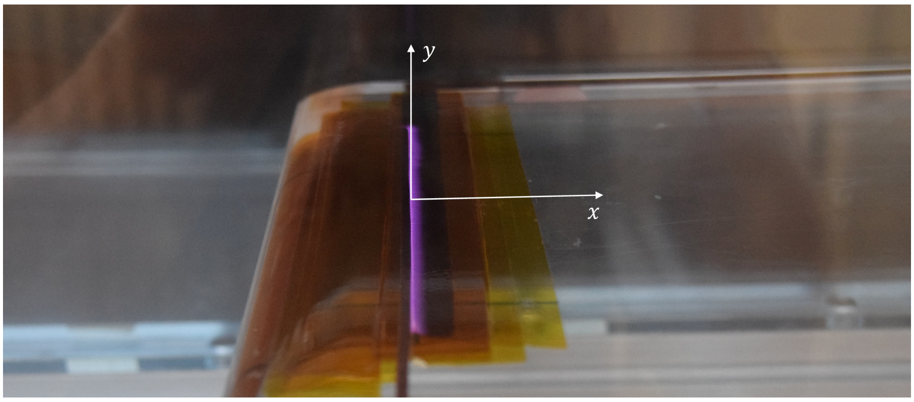

(a)

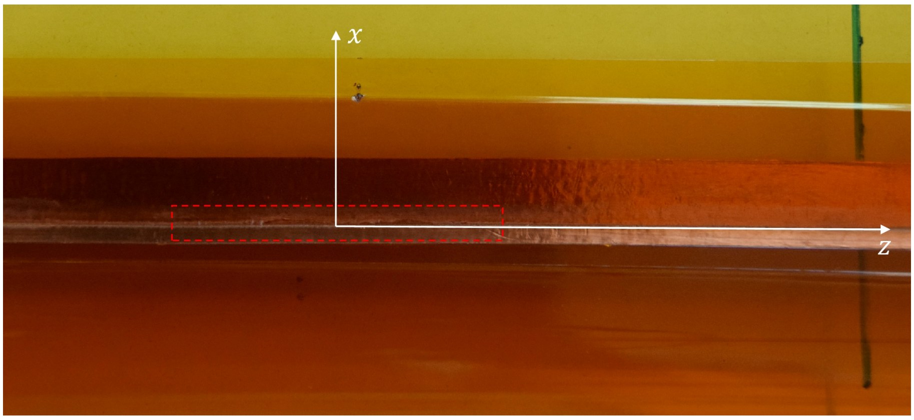

(b)

Figure 6.6: AC-DBD plasma actuator analysis. (a) Plasma actuator assembly; (b) Dielectric degradation (red dashed line).

Chapter 7

Conclusions

In this chapter the conclusions of the present study are summarized and improvements for future works are proposed.

7.1 Achievements

In the present experimental investigation, the electrical and mechanical characteristics of an AC-DBD plasma actuator were determined in presence of an external laminar BL flow. Regarding the electrical quantities, the power consumption (sec.5.1.1) and current signal (sec.5.1.2) analysis led to a virtually constant power consumption of the plasma actuator for flow speeds up to $U_\infty = 20$ m/s and indicated the regimes of discharge collapse are located at the same phase positions regardless of the operating free-stream velocity [7, 8]. As for mechanical characterization, phase-resolved velocity information was acquired with high phase resolution of 24 phases per discharge cycle to derive the body-force fields, using the N.S.E. and V.E. methods (sec.3.1) [18, 19]. The insights into the phenomena occurring over a discharge-cycle can be summarized as follows:

- The N.S.E. method introduced by Wilke [18] (sec.3.1) relies on a negligibly small pressure gradient due to the plasma discharge, however this assumption is an oversimplication of the problem when considering the presence of external airflow. The volume integrated time-averaged force F_x showed a decisively decreasing behaviour, which results in negative values of the force for $U_\infty > 15$ m/s. This result is attributed to the fact that the pressure gradient is neglected in the calculations, as no physical phenomenon associated with imposing an external airflow on an AC-DBD plasma actuator may explain the change in direction of the plasma-force production (sec.5.2.1). The impact of the external airflow on the body-force field estimation is already noticeable at low free-stream velocities $U_\infty = 5$ m/s (fig.5.7(a)) and tends to continuously grow as the free-stream velocity is increased up to $U_\infty = 20$ m/s.
- In contrast, the body-force model by Albrecht et al. [19] (sec.3.1) relies on the assumption of a negligibly force gradient $\partial f_y / \partial x$, thus it solves only the wall-parallel component of the force

$f_x(x, y)$. The body-force field results show good agreement for external-airflow velocities up to $U_\infty = 10$ m/s whereas a mild change is detected for higher free-stream velocities $U_\infty = 20$ m/s (fig. 5.8(a)-(c)). The time-averaged volume-integrated force F_x shows only a mild variation when operating with external flow. Nonetheless, the results tend to converge to a rather constant value for free-stream velocities up to $U_\infty = 15$ m/s. It is also noted that the integral-force magnitude is found to be within a determined order-of-magnitude $\mathcal{O}(10)$ (sec.5.2.1), correlating with the power consumption analysis of the actuator (sec.5.1.1). Such a conclusion is further reflected by the fluid-mechanic effectiveness of the actuator (sec.6.4). Nonetheless, the problem of the unknown wall-normal force $f_y(x, y)$ remains to be solved in future.

- From the time-averaged volume-integrated force determined with the V.E. approach, it may be concluded that the fluid-mechanic efficiency increases with increasing velocity, which is consistent with a nearly constant fluid-mechanic effectiveness (sec.6.4). This outcome indicates an increase in the control authority of plasma actuators within the tested range of external-airflow velocities. However, for higher free-stream velocities it is expected that the fluid-mechanic effectiveness decreases as the external flow velocity approaches the ion drift velocity. Therefore, experiments have to be extended to higher free-stream velocities.

- The contribution of each source term to the body-force field, using both methods, has been considered (sec.3.1) [18, 19]. Regarding the convective term, the results seem to indicate an influence of the external airflow for both models. Specially for the N.S.E. where the difference between results obtained in quiescent-air conditions and $U_\infty = 20$ m/s is evident. In contrast, the unsteady component appear to be virtually constant for free-stream velocities up to $U_\infty = 10$ m/s for both N.S.E. and V.E. methods. For higher free-stream velocities, such a conclusion only holds for the V.E. approach. This leads to the conclusion that for low external airflow velocities ≤ 10 m/s, the integral-force determination can be reduced to a quiescent-air analysis. However, this only holds for the V.E. approach where the convective terms undergo minor changes. Hence, it may significantly reduce the effort of an experimental investigation since time-averaged PIV would be sufficient to study the influence of external airflow on the AC-DBD plasma net force. In contrast, in order to gain insight into the spatial distribution, phase-resolved measurements have indeed to be performed in the presence of external airflow.

- The sensitivity analysis clarifies that higher phase resolution leads to more accurate phase-resolved body-force estimation (sec.6.3). However, for time-averaged net-force estimation its impact is found to be insignificant due to the independence of the temporal term [17].

- The reliability of both the plasma actuator (in terms of manufacturing and operation) and the force-determination strategy has been demonstrated by the reproducibility study which justifies a solid interpretation of the results on the force distributions and magnitudes. (sec.6.5).

- First PIV experiments to successfully derive the phase-resolved and time-averaged body-force fields from velocity fields in external laminar BL flow.

7.2 Future Work

The present experimental characterization of an AC-DBD plasma actuator in the presence of external airflow can be further improved in future experimental campaigns. Hence, the recommendations are summarized as follows:

- The acquisition rate used to record the electrical quantities (sec. 4.1.3) for the current-signal analysis (sec. 5.1.2) and determination of power consumption (sec. 5.1.1) has to be carefully re-evaluated. For instance, the current-signal analysis indicated a slightly different behaviour compared to previous reports. The negative-going half cycle features large current peaks and it is somehow irregular, instead of rather uniform behaviour which is characteristic [17, 21, 23]. These measurements can be improved by a higher vertical resolution of the acquisition device. Regarding the power consumption analysis, the resolution of the $Q-V$ cyclogram i.e. the two sharp edges is essential to capture small power consumption variations [30]. To clarify the distinct results, in future experiments it is recommended to use higher acquisition rate to acquire the electrical quantities.

- The assembly of the plasma actuator and location on the elliptic edge flat plate are pointed as a source of uncertainty (sec. 6.6). The proximity to the leading edge has also to be accounted for, hence to minimize the impact of the flow deceleration on the plasma actuator and velocity measurements. In addition, the actuator should be placed in a trough since the assembly directly on the flat plate results in several forward- and backward-facing steps. As a consequence, it might induce a curvature on the flow, hence it is a potential source of uncertainty to the velocity measurements.

- The degradation of the dielectric evidences that the plasma actuator should be further improved in terms of durability in order to be placed in practical applications (sec. 6.6). Furthermore, an automated production of the actuator could improve the repeatability as the present actuators were manually fabricated and are thus never equal.

- The plasma body-force field determination should be extended to the higher free-stream velocities. On one hand, the fluid-mechanic efficiency is found to increase for the considered free-stream velocities, however for higher external-airflow velocities the actuator flow-control authority is expected to decrease (sec. 6.4). On the other hand, the tested free-stream velocities are considerably low when compared to practical applications such as aircraft and motorsport engineering.

- The induced airflow produced by a plasma actuator is assumed to be incompressible. Nonetheless, there might be variations in the local density of the plasma discharge that might lead to second order effects and hence influence the results. In present study, it was verified that the incompressible continuity equation does not hold within the entire CV (not shown). However, the impact was not considered in the body-force fields calculation since it would require a study with the compressible N.S.E. and further assumptions regarding temperature and density fields. Accordingly, it is highly recommended as a next step in plasma body-force fields characterization to analyse the density and temperature variations in the discharge region.

Bibliography

[1] L. N. Cattafesta and M. Sheplak. Actuators for active flow control. *Annual Review of Fluid Mechanics*, 43(1):247–272, 2011. doi: 10.1146/annurev-fluid-122109-160634.

[2] L. Leger, E. Moreau, and G. Touchard. Control of low velocity airflow along a flat plate with a dc electrical discharge. volume 3, pages 1536 – 1543 vol.3, 01 2001. ISBN 0-7803-7114-3. doi: 10.1109/IAS.2001.955739.

[3] C. Y. Schuele, T. C. Corke, and E. Matlis. Control of stationary cross-flow modes in a mach 3.5 boundary layer using patterned passive and active roughness. *Journal of Fluid Mechanics*, 718: 5–38, 2013.

[4] J. Jolibois, M. Forte, and r. Moreau. Application of an ac barrier discharge actuator to control airflow separation above a naca 0015 airfoil: Optimization of the actuation location along the chord. *Journal of Electrostatics*, 66(9):496 – 503, 2008. ISSN 0304-3886. doi: https://doi.org/10.1016/j.elstat.2008.03.008.

[5] N. Benard, J. Jolibois, and E. Moreau. Lift and drag performances of an axisymmetric airfoil controlled by plasma actuator. *Journal of Electrostatics*, 67(2):133 – 139, 2009. ISSN 0304-3886. doi: https://doi.org/10.1016/j.elstat.2009.01.008. 11th International Conference on Electrostatics.

[6] J. Little, M. Nishihara, I. Adamovich, and M. Samimy. High-lift airfoil trailing edge separation control using a single dielectric barrier discharge plasma actuator. *Experiments in Fluids*, 48:521–537, 03 2009. doi: 10.1007/s00348-009-0755-x.

[7] D. Ashpis, M. Laun, and E. Griebeler. *Progress toward Accurate Measurements of Power Consumption of DBD Plasma Actuators*. 2012. doi: 10.2514/6.2012-823.

[8] J. Kriegseis, S. Grundmann, and C. Tropea. Power consumption, discharge capacitance and light emission as measures for thrust production of dielectric barrier discharge plasma actuators. *Journal of Applied Physics*, 110(1):013305, 2011. doi: 10.1063/1.3603030.

[9] R. Pereira, D. Ragni, and M. Kotsonis. Effect of external flow velocity on momentum transfer of dielectric barrier discharge plasma actuators. *Journal of Applied Physics*, 116:103301–103301, 09 2014. doi: 10.1063/1.4894518.

[10] M. Kotsonis and S. Ghaemi. Experimental and numerical characterization of a plasma actuator in continuous and pulsed actuation. *Sensors and Actuators A: Physical*, 187:84 – 94, 2012. ISSN 0924-4247. doi: https://doi.org/10.1016/j.sna.2012.08.002.

[11] J.-P. Boeuf, Y. Lagmich, T. Unfer, T. Callegari, and L. Pitchford. Electrohydrodynamic force in dielectric barrier discharge plasma actuators. *Journal of Physics D Applied Physics*, 40:652–662, 02 2007. doi: 10.1088/0022-3727/40/3/S03.

[12] P. Dörr and M. Kloker. Numerical investigation of plasma actuator force-term estimations from flow experiments. *Journal of Physics D Applied Physics*, 48, 09 2015. doi: 10.1088/0022-3727/48/39/395203.

[13] G. Font, C. Enloe, and T. McLaughlin. Effect of volumetric momentum addition on the total force production of a plasma actuator. Number 0 in Fluid Dynamics and Co-located Conferences. American Institute of Aeronautics and Astronautics, Mar. 2009. doi: 10.2514/6.2009-4285.

[14] C. Enloe, T. McLaughlin, R. Van Dyken, and J. Fischer. Plasma structure in the aerodynamic plasma actuator. Number 0 in Aerospace Sciences Meetings. American Institute of Aeronautics and Astronautics, Mar. 2004. doi: 10.2514/6.2004-844.

[15] C. Enloe, M. McHarg, G. Font, and T. McLaughlin. Plasma induced drag. 2009. doi: 10.2514/6.2009-1622.

[16] A. Debien, N. Benard, and E. Moreau. Streamer inhibition for improving force and electric wind produced by DBD actuators. *Journal of Physics D: Applied Physics*, 45(21):215201, may 2012. doi: 10.1088/0022-3727/45/21/215201.

[17] N. Benard, A. Debien, and E. Moreau. Time-dependent volume force produced by a non-thermal plasma actuator from experimental velocity field. *Journal of Physics D: Applied Physics*, 46(24): 245201, may 2013. doi: 10.1088/0022-3727/46/24/245201.

[18] B. Wilke. *Aerodynamische strömungssteuerung mittels dielektrischen Barriereentladungs-Plasmaaktuatoren*. PhD thesis, Technische Universität Darmstadt, DLR, 2009.

[19] T. Albrecht, T. Weier, G. Gerbeth, H. Metzkes, and J. Stiller. A method to estimate the planar, instantaneous body force distribution from velocity field measurements. *Physics of Fluids - PHYS FLUIDS*, 23, 02 2011.

[20] T. Corke, M. L. Post, and D. M. Orlov. Sdbd plasma enhanced aerodynamics: concepts, optimization and applications. *Progress in Aerospace Sciences*, 43:193–217, 10 2007. doi: 10.1016/j.paerosci.2007.06.001.

[21] E. Moreau. Airflow control by non-thermal plasma actuators. *Journal of Physics D: Applied Physics*, 40(3):605–636, jan 2007. doi: 10.1088/0022-3727/40/3/s01.

[22] M. Forte, J. Jolibois, J. Pons, E. Moreau, G. Touchard, and M. Cazalens. Optimization of a dielectric barrier discharge actuator by stationary and non-stationary measurements of the induced flow velocity: Application to airflow control. *Experiments in Fluids*, 43:917–928, 01 2007. doi: 10.1007/s00348-007-0362-7.

[23] J. Pons, E. Moreau, and G. Touchard. Asymmetric surface dielectric barrier discharge in air at atmospheric pressure: electrical properties and induced airflow characteristics. *Journal of Physics D: Applied Physics*, 38(19):3635–3642, sep 2005. doi: 10.1088/0022-3727/38/19/012.

[24] N. Benard and E. Moreau. Capabilities of the dielectric barrier discharge plasma actuator for multi-frequency excitations. *Journal of Physics D: Applied Physics*, 43(14):145201, mar 2010. doi: 10.1088/0022-3727/43/14/145201.

[25] R. Giepman and M. Kotsonis. On the mechanical efficiency of dielectric barrier discharge plasma actuators. *Applied Physics Letters - APPL PHYS LETT*, 98:1504–221504, 05 2011. doi: 10.1063/1.3597652.

[26] P. Versailles, V. Gingras-Gosselin, and H. D. Vo. Impact of pressure and temperature on the performance of plasma actuators. *AIAA Journal*, 48(4):859–863, 2010. doi: 10.2514/1.43852.

[27] M. Kotsonis, S. Ghaemi, L. Veldhuis, and F. Scarano. Measurement of the body force field of plasma actuators. *Journal of Physics D: Applied Physics*, 44(4):045204, jan 2011. doi: 10.1088/0022-3727/44/4/045204.

[28] J. Kriegseis, C. Schwarz, C. Tropea, and S. Grundmann. Velocity-information-based force-term estimation of dielectric-barrier discharge plasma actuators. *Journal of Physics D: Applied Physics*, 46(5):055202, jan 2013. doi: 10.1088/0022-3727/46/5/055202.

[29] M. Kuhnhenn, B. Simon, I. Maden, and J. Kriegseis. Interrelation of phase-averaged volume force and capacitance of dielectric barrier discharge plasma actuators. *Journal of Fluid Mechanics*, 809, 12 2016. doi: 10.1017/jfm.2016.679.

[30] J. Kriegseis, S. Grundmann, and C. Tropea. Airflow influence on the discharge performance of dielectric barrier discharge plasma actuators. *Physics of Plasmas*, 19(7):073509, 2012. doi: 10.1063/1.4736995.

[31] J. Roth. Industrial plasma engineering, volume 1: Principles, by j. reece roth. iop publishing, 2001. isbn 750308257. *Journal of Plasma Physics*, 68:237 – 240, 04 1995. doi: 10.1017/S0022377803222170.

[32] J. Roth, D. Sherman, and S. Wilkinson. *Boundary layer flow control with a one atmosphere uniform glow discharge surface plasma*. 1998. doi: 10.2514/6.1998-328.

[33] F. O. Thomas, T. C. Corke, M. Iqbal, A. Kozlov, and D. Schatzman. Optimization of dielectric barrier discharge plasma actuators for active aerodynamic flow control. *AIAA Journal*, 47(9):2169–2178, Mar. 2009. ISSN 0001-1452. doi: 10.2514/1.41588.

[34] C. L. Enloe, T. E. McLaughlin, R. D. Van Dyken, K. D. Kachner, E. J. Jumper, and T. C. Corke. Mechanisms and responses of a single dielectric barrier plasma actuator: Plasma morphology. *AIAA Journal*, 42(3):589–594, Mar. 2004. ISSN 0001-1452. doi: 10.2514/1.2305.

[35] C. L. Enloe, T. E. McLaughlin, R. D. Van Dyken, K. D. Kachner, E. J. Jumper, T. C. Corke, M. Post, and O. Haddad. Mechanisms and responses of a dielectric barrier plasma actuator: Geometric effects. *AIAA Journal*, 42(3):595–604, Mar. 2004. ISSN 0001-1452. doi: 10.2514/1.3884.

[36] J. Kriegseis, B. Möller, S. Grundmann, and C. Tropea. Capacitance and power consumption quantification of dielectric barrier discharge (dbd) plasma actuators. *Journal of Electrostatics - J ELECTROSTAT*, 69:302–312, 08 2011. doi: 10.1016/j.elstat.2011.04.007.

[37] E. Moreau, L. Léger, and G. Touchard. Effect of a dc surface-corona discharge on a flat plate boundary layer for air flow velocity up to 25m/s. *Journal of Electrostatics*, 64(3):215 – 225, 2006. ISSN 0304-3886. doi: https://doi.org/10.1016/j.elstat.2005.05.009.

[38] N. Benard, E. Moreau, N. Zouzou, H. Rabat, J. Pons, D. Hong, A. Leroy, P. Peschke, and C. Hollenstein. Nanosecond pulsed plasma actuators. *ERCOFTAC Bulletin*, 94:11–16, 03 2013.

[39] G. Correale, T. Michelis, D. Ragni, M. Kotsonis, and F. Scarano. Nanosecond-pulsed plasma actuation in quiescent air and laminar boundary layer. *Journal of Physics D: Applied Physics*, 47:105201, 02 2014. doi: 10.1088/0022-3727/47/10/105201.

[40] B. Dong, J. M. Bauchire, J. M. Pouvesle, P. Magnier, and D. Hong. Experimental study of a DBD surface discharge for the active control of subsonic airflow. *Journal of Physics D: Applied Physics*, 41(15):155201, jun 2008. doi: 10.1088/0022-3727/41/15/155201.

[41] M. Kotsonis. Diagnostics for characterisation of plasma actuators. *Measurement Science and Technology*, 26, 09 2015. doi: 10.1088/0957-0233/26/9/092001.

[42] D. M. Orlov and D. Edelstein. Characterization of discharge modes of plasma actuators. *Aiaa Journal - AIAA J*, 46:3142–3148, Dec. 2008.

[43] A. V. Likhanskii, M. N. Shneider, S. O. Macheret, and R. B. Miles. Modeling of dielectric barrier discharge plasma actuator in air. *Journal of Applied Physics*, 103(5):053305, 2008. doi: 10.1063/1.2837890.

[44] J. R. Roth, D. M. Sherman, and S. P. Wilkinson. Electrohydrodynamic flow control with a glow-discharge surface plasma. *AIAA Journal*, 38(7):1166–1172, Mar. 2000. ISSN 0001-1452. doi: 10.2514/2.1110.

[45] J. Jolibois and E. Moreau. Enhancement of the electromechanical performances of a single dielectric barrier discharge actuator. *Dielectrics and Electrical Insulation, IEEE Transactions on*, 16:758 – 767, 07 2009. doi: 10.1109/TDEI.2009.5128516.

[46] J. Kriegseis, A. Duchmann, C. Tropea, and S. Grundmann. On the classification of dielectric barrier discharge plasma actuators: A comprehensive performance evaluation study. *Journal of Applied Physics*, 114(5):053301, 2013. doi: 10.1063/1.4817366.

[47] A. R. Hoskinson, N. Hershkowitz, and D. E. Ashpis. Force measurements of single and double barrier DBD plasma actuators in quiescent air. *Journal of Physics D: Applied Physics*, 41(24): 245209, nov 2008. doi: 10.1088/0022-3727/41/24/245209.

[48] R. Durscher and S. Roy. Force measurement techniques and preliminary results using aerogels and ferroelectrics for dielectric barrier discharge actuators. 06 2011. doi: 10.2514/6.2011-3735.

[49] R. E. Hanson, N. M. Houser, and P. Lavoie. Dielectric material degradation monitoring of dielectric barrier discharge plasma actuators. *Journal of Applied Physics*, 115(4):043301, 2014. doi: 10.1063/1.4862309.

[50] S. Pavon, J.-L. Dorier, C. Hollenstein, P. Ott, and P. Leyland. Effects of high-speed airflows on a surface dielectric barrier discharge. *Journal of Physics D: Applied Physics*, 40(6):1733–1741, mar 2007. doi: 10.1088/0022-3727/40/6/021.

[51] M. Raffel, C. E. Willert, S. Wereley, and J. Kompenhans. *Particle Image Velocimetry*. Springer-Verlag Berlin Heidelberg, 2 edition, 2007. ISBN 978-3-540-72308-0. doi: 10.1007/978-3-540-72308-0.

[52] D. E. Ashpis, M. C. Laun, and E. L. Griebeler. Progress toward accurate measurement of dielectric barrier discharge plasma actuator power. *AIAA Journal*, 55(7):2254–2268, 2017. doi: 10.2514/1.J055816.

[53] A. Sciacchitano and B. Wieneke. Piv uncertainty propagation. *Measurement Science and Technology*, 27:084006, 08 2016. doi: 10.1088/0957-0233/27/8/084006.

[54] V. d. Brederode. *Aerodinâmica Incompressível: Fundamentos*. IST Press, 2014. ISBN 978-989-8481-32-0.

[55] K. Schlichting, Hermann Gersten. *Boundary-Layer Theory*. Springer, Berlin, Heidelberg, 9th edition edition, 2017. ISBN 978-3-662-52917-1.

[56] R. Pereira, M. Kotsonis, G. de Oliveira, and D. Ragni. Analysis of local frequency response of flow to actuation: Application to the dielectric barrier discharge plasma actuator. *Journal of Applied Physics*, 118(15):153301, 2015. doi: 10.1063/1.4933292.

[57] T. C. Manley. The electric characteristics of the ozonator discharge. *Transactions of The Electrochemical Society*, 84(1):83, 1943. doi: 10.1149/1.3071556.

Appendix A

Time-averaged body-force fields

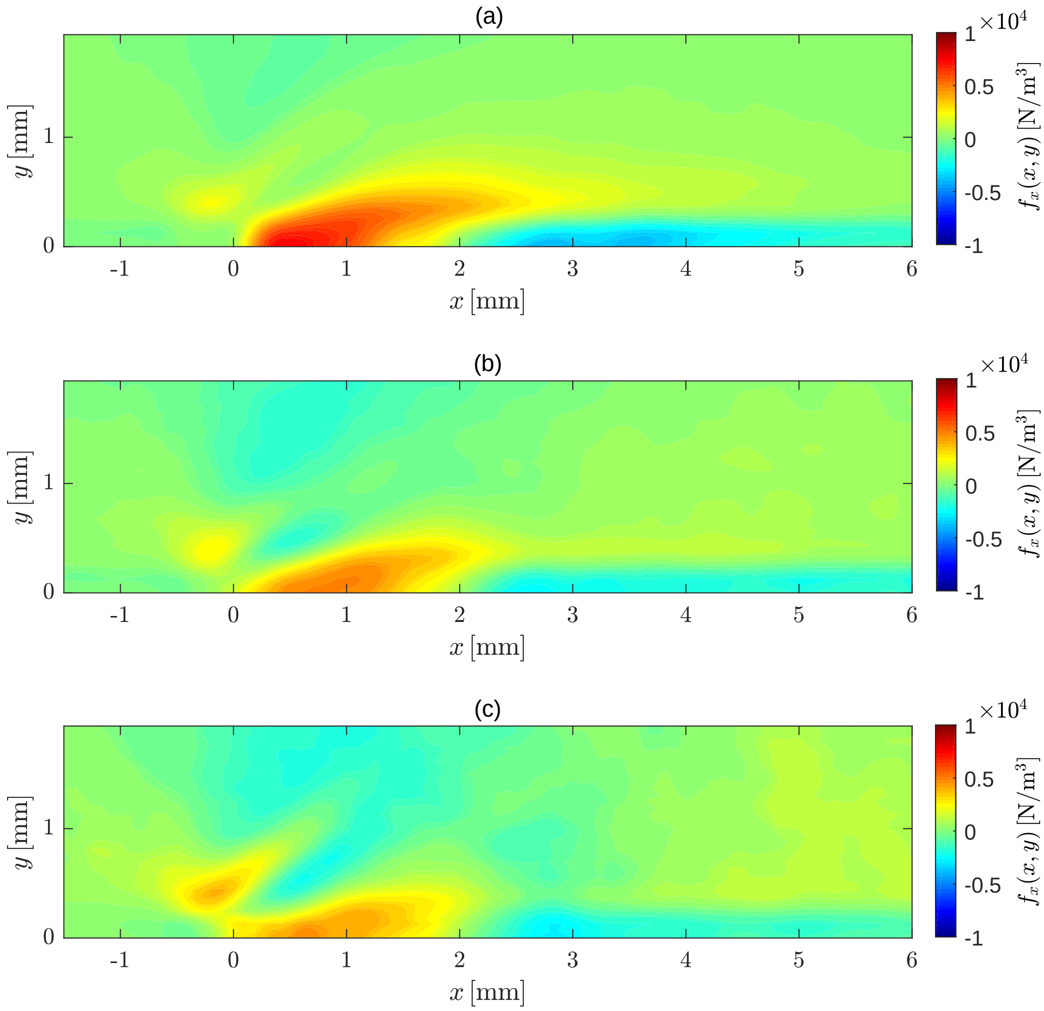

Figure A.1: Horizontal component of the body-force field distribution $f_x(x, y)$ determined according to N.S.E. (equation 3.2a) for different free-stream velocities U_∞. (a) $U_\infty = 2.5$ m/s; (b) $U_\infty = 7.5$ m/s; (c) $U_\infty = 15$ m/s.

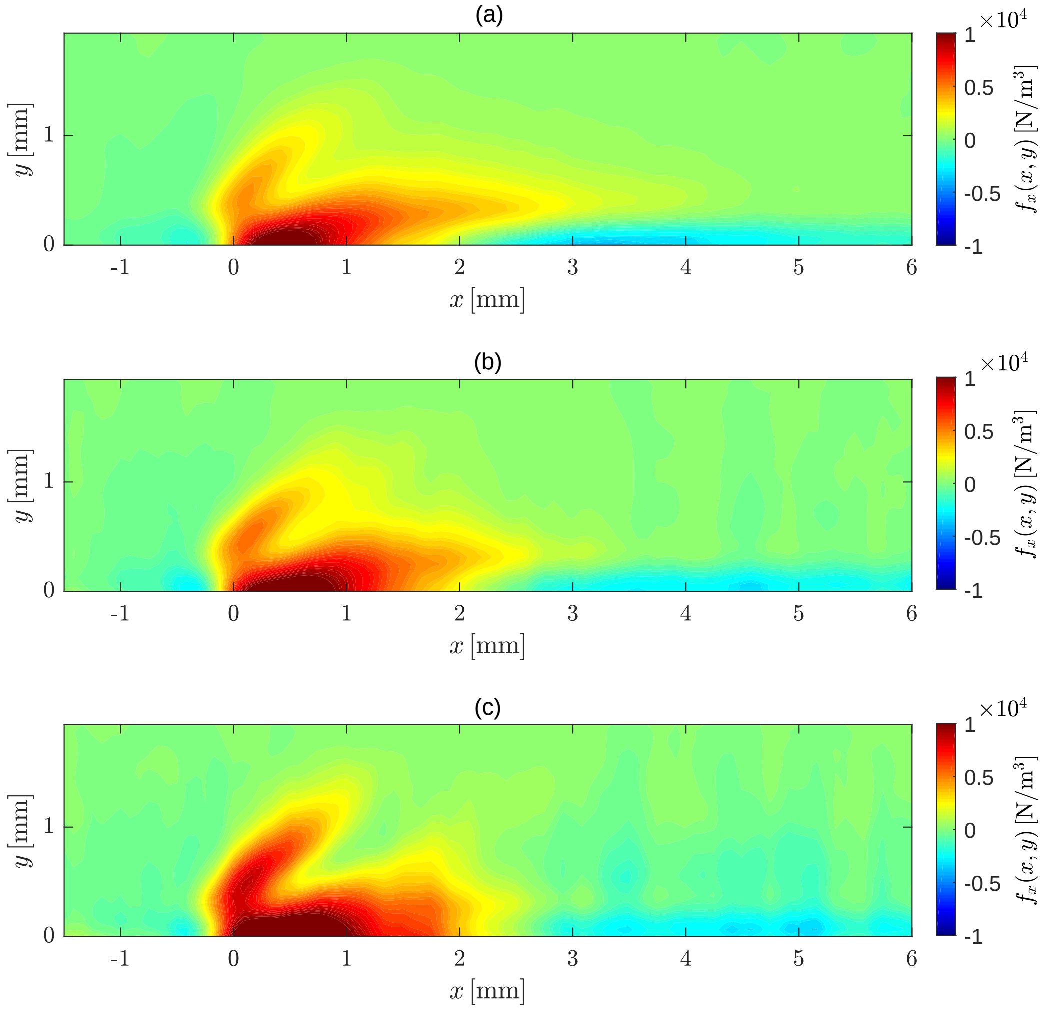

Figure A.2: Horizontal component of the body-force field distribution $f_x(x, y)$ determined according to V.E. (equation 3.6) for different free-stream velocities U_∞. (a) $U_\infty = 2.5$ m/s; (b) $U_\infty = 7.5$ m/s; (c) $U_\infty = 15$ m/s.

Appendix B

Phase-resolved body-force fields

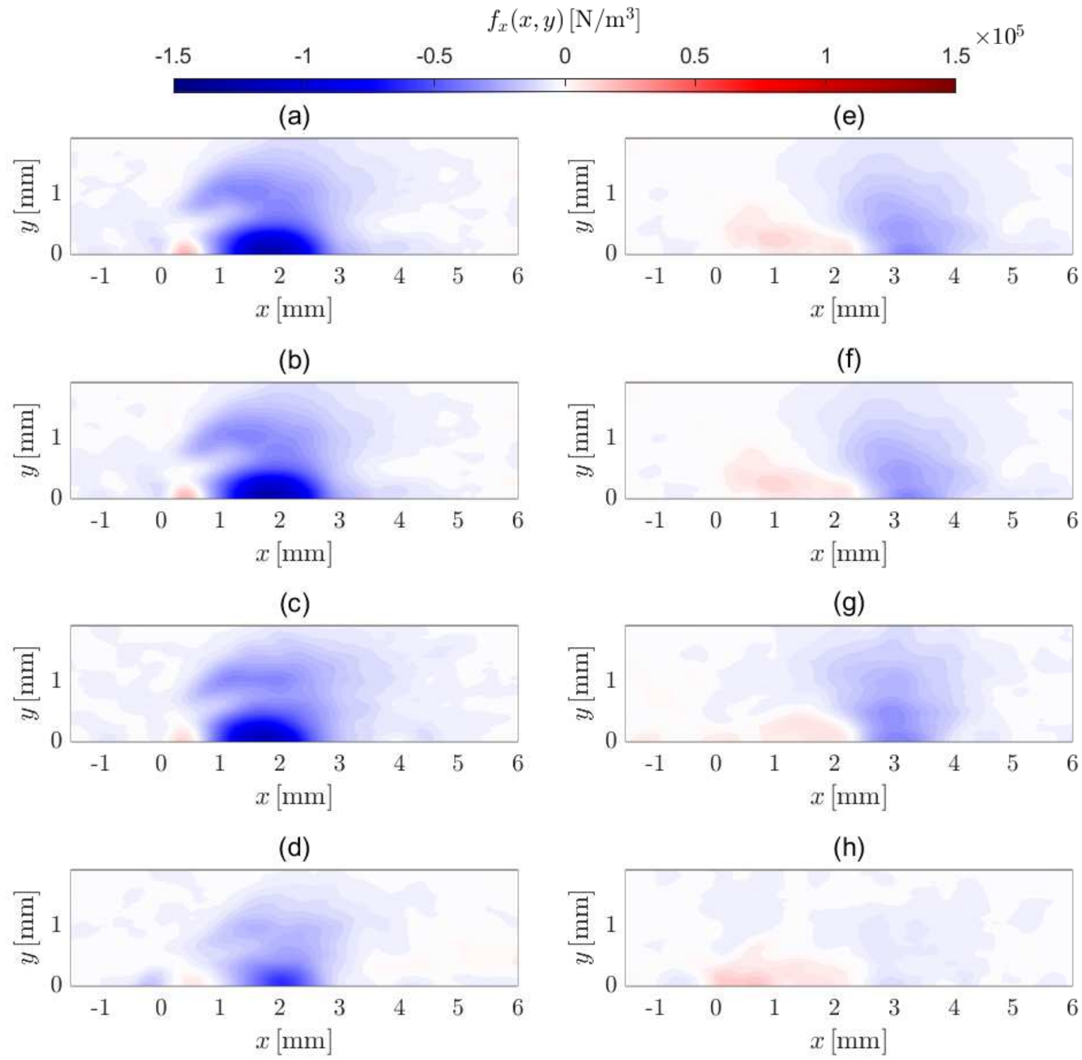

Figure B.1: Phase-resolved body-force field distribution on the positive-going half cycle for increasing free-stream velocity $U_\infty = [0, 5, 10, 15]$ m/s determined according to N.S.E. (equation 3.2a). (a)-(d) $\phi = \pi/12$; (e)-(h) $\phi = \pi/3$.

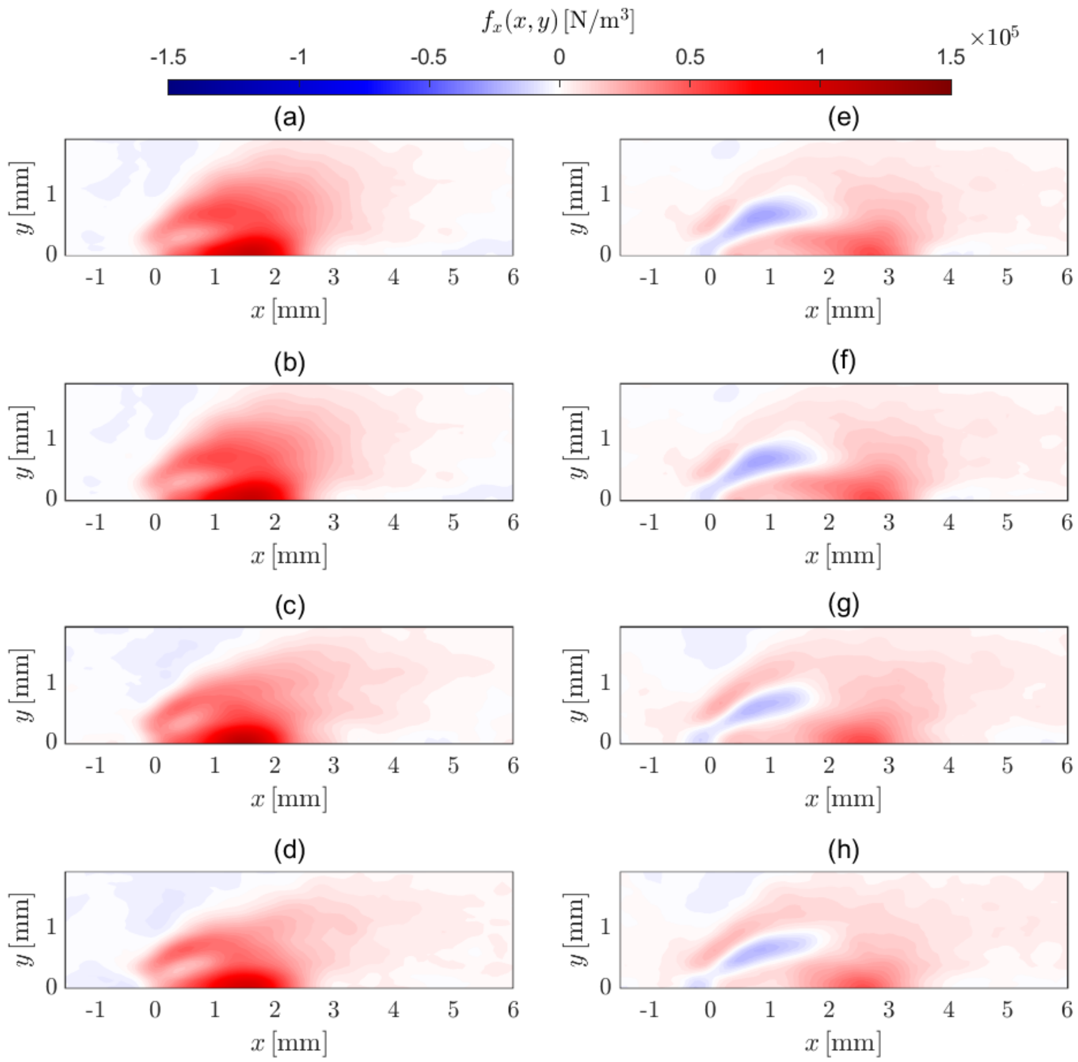

Figure B.2: Phase-resolved body-force field distribution on the positive-going half cycle for increasing free-stream velocity $U_\infty = [0, 5, 10, 15]$ m/s determined according to N.S.E. (equation 3.2a). (a)-(d) $\phi = 5\pi/4$; (e)-(h) $\phi = 17\pi/12$.

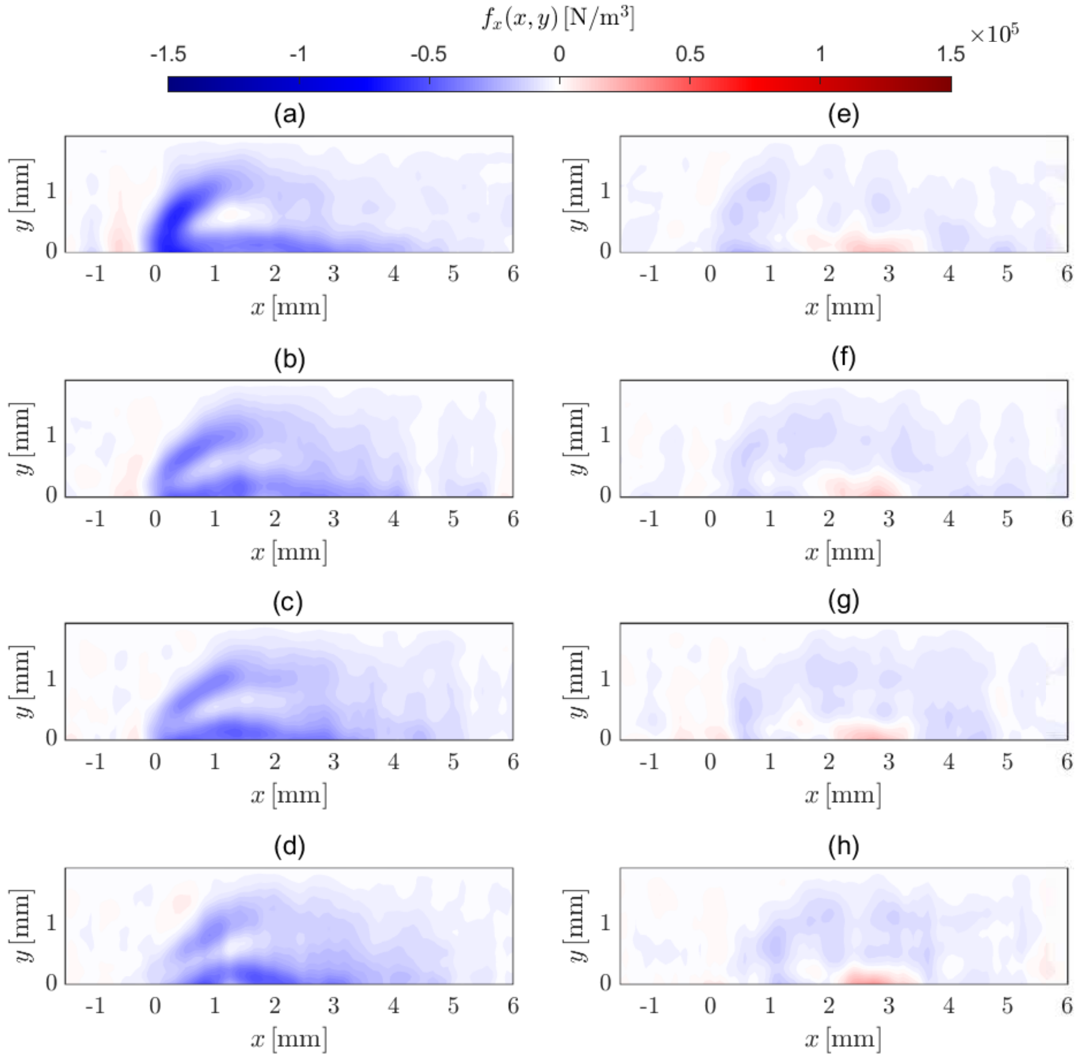

Figure B.3: Phase-resolved body-force field distribution on the positive-going half cycle for increasing free-stream velocity $U_\infty = [0, 5, 10, 15]$ m/s determined according to V.E. (equation 3.6). (a)-(d) $\phi = \pi/12$; (e)-(h) $\phi = \pi/3$.

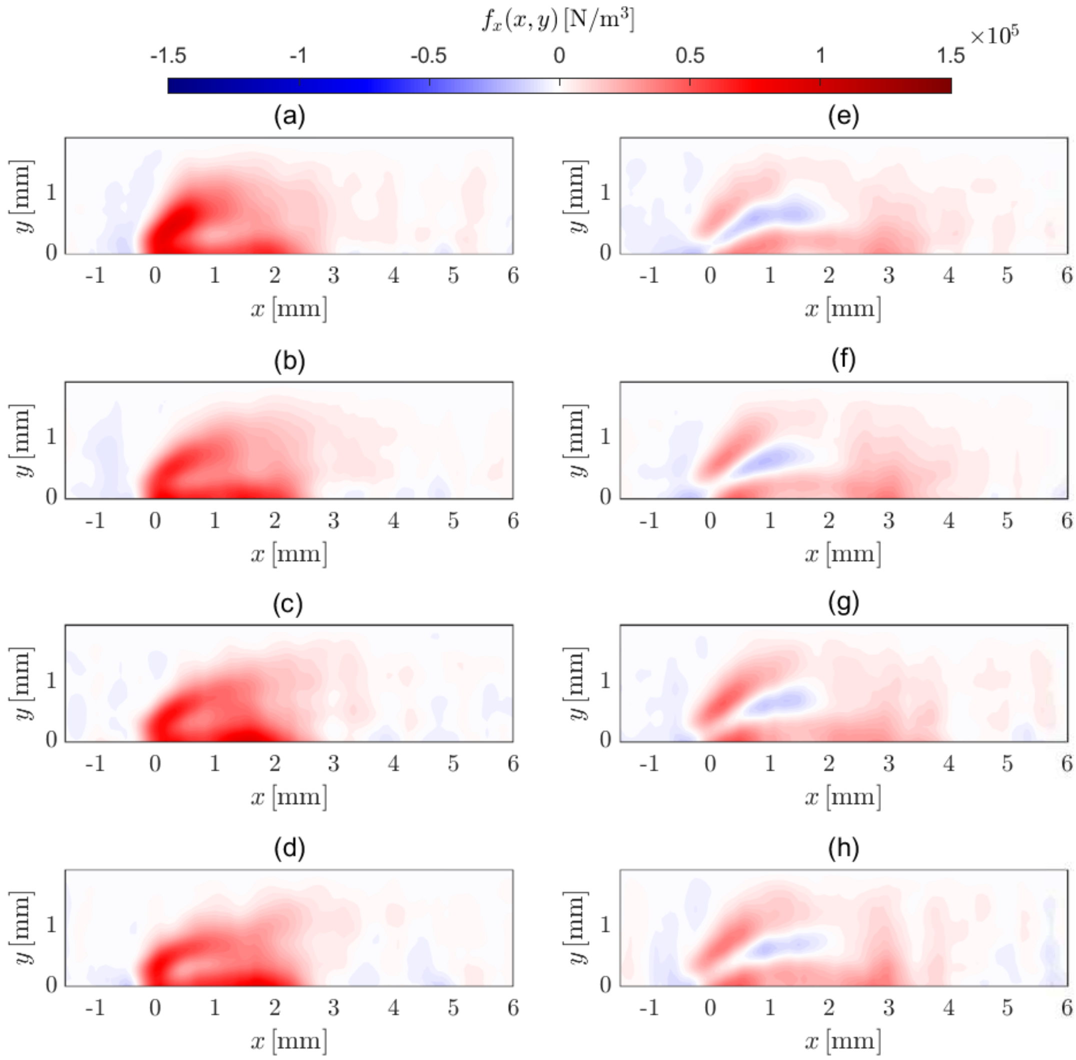

Figure B.4: Phase-resolved body-force field distribution on the positive-going half cycle for increasing free-stream velocity $U_\infty = [0, 5, 10, 15]$ m/s determined according to V.E. (equation 3.6). (a)-(d) $\phi = 5\pi/4$; (e)-(h) $\phi = 17\pi/12$.

List of Scientific Contributions

M. T. Hehner, G. Coutinho, S. Najam, R. Pereira, and J. Kriegseis. Phase-resolved body-force estimation of AC-DBD plasma actuator at various airflow speeds. Lecture held at 15th International Symposium on Fluid Control Measurement Mechanics and Flow Visualisation (FLUCOME 2019), Naples, Italy, May 26–30, 2019.

M. T. Hehner, G. Coutinho, R. Pereira, N. Benard and J. Kriegseis. Phase-resolved Body-force Determination of an AC-DBD Plasma Actuator in Laminar Flow. Lecture to be held at 72nd Annual Meeting of the American Physical Society (APS) Division of Fluid Dynamics, Seattle, United States of America, November 23–26, 2019.

M. T. Hehner, G. Coutinho, R. Pereira, N. Benard and J. Kriegseis. On the interplay of body forces and flow speed for DBD-based flow control. *Journal of Physics D: Applied Physics*. To be submitted.